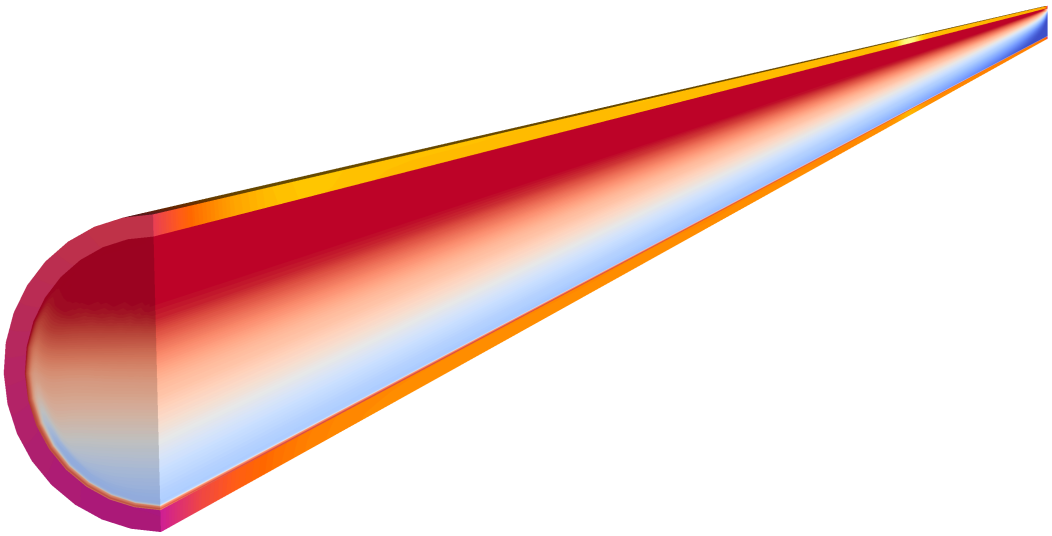

Assessment of Multiphase Boiling Models

For Modelling of Heat and Mass Transfer In An Aero Engine Steam Vaporizer Tube

Master's thesis in Sustainable Energy Systems

ALEXANDER BLOM LARSEN

DEPARTMENT OF MECHANICAL AND MARITIME SCIENCES

CHALMERS UNIVERSITY OF TECHNOLOGY
Gothenburg, Sweden 2024
www.chalmers.se

Master's thesis 2024

Assessment of Multiphase Boiling Models

For Modelling of Heat and Mass Transfer In An Aero Engine Steam Vaporizer Tube

ALEXANDER BLOM LARSEN

CHALMERS
UNIVERSITY OF TECHNOLOGY

Department of Mechanics and Maritime Sciences
Division of Fluid Dyanmics
Chalmers University of Technology
Gothenburg, Sweden 2024

Assessment of Multiphase Boiling Models
For Modelling of Heat and Mass Transfer In An Aero Engine Steam Vaporizer Tube
ALEXANDER BLOM LARSEN

Supervisor: Jonathan Bergh, Future Engines, GKN Aerospace Engine Systems (Sweden)
Examiner: Srdjan Sasic, Chalmers University of Technology, Department of Mechanics and Maritime Sciences

Master's Thesis 2024
Department of Mechanics and Maritime Sciences
Division of Fluid Dynamics
Chalmers University of Technology
SE-412 96 Gothenburg
Telephone +46 31 772 1000

Cover: Cross-sectional view of single heat exchanger tube, along with contours plots showing the wall temperature of the tube, as well as the vapour volume fraction inside the tube.

Typeset in LaTeX
Printed by Chalmers Reproservice
Gothenburg, Sweden 2024

Assessment of Multiphase Boiling Models
For Modelling of Heat and Mass Transfer In An Aero Engine Steam Vaporizer Tube
ALEXANDER BLOM LARSEN
Department of Mechanics and Maritime Sciences
Chalmers University of Technology

Abstract

The growing aviation industry is transitioning towards more sustainable and efficient aero engines, with many aerospace companies investigating the use of heat exchanger technology to reduce specific fuel consumption (SFC) and enhance thermal efficiency. Multiphase boiling models enable the analysis of flow behaviour and performance of heat exchanger systems, including mass, momentum, and heat transfer. This thesis provides a comprehensive analysis of the Lee and Thermal Phase Change boiling models and their available sub models in terms of their robustness and accuracy in modelling fully phase inverted boiling scenarios.

A survey of the available sub-models was conducted to conclude how different modelling approaches affects the results. In terms of the Interfacial Area Concentration (IAC) modelling, the interfacial area transport equation approach promoted boiling for the Lee model, while inhibiting it for the Thermal Phase Change model. The algebraic model displayed better convergence behaviour. As for heat transfer modelling, the double-resistance approach yielded more accurate wall temperatures than the single-resistance approach. Regarding turbulence modelling, solving two sets of turbulence equations showed negligible differences compared to a single set. The $k - \omega$ SST model was deemed more appropriate for this case compared to the standard $k - \varepsilon$ model. In terms of the interfacial momentum transfer (force) modelling, the results showed that only modelling the drag and turbulent dispersion forces affected the results non-trivially.

When compared to experiments, in all cases the numerical results matched experimental data poorly, although the Thermal Phase Change model was seen to outperform the Lee model relatively speaking. Tuning the model coefficients showed some improvement, especially for the Lee model, but not for the Thermal Phase Change model. Finally, in order to assess any impact of explicit modelling of the tube walls on the overall veracity of the numerical results, including the tube wall thicknesses explicitly was to seen to improve the performance of both the Lee and Thermal Phase Change models, particularly when used in conjunction with the double-resistance thermal resistance approach.

Keywords: Heat transfer, boiling, multiphase, CFD, Eulerian multiphase, Conjugate heat transfer.

Acknowledgements

First and foremost, I would like to express my deepest gratitude to my supervisor at GKN Aerospace, Jonathan Bergh, for his continuous support, guidance, and encouragement throughout this spring. His invaluable insights and expertise have been instrumental in the completion of this thesis.

I am also profoundly grateful to Jonas Bredberg for his constructive feedback and suggestions, which significantly enhanced the quality of this work.

A special thanks to my fellow thesis workers at GKN Aerospace for their camaraderie, intellectual discussions, and moral support. I particularly want to acknowledge Suraj Shankar for being a great teammate and collaborator.

I would also like to express my deepest appreciation to my friend, August Skoglund, for his great banter, questionable music takes, and for always being there during the challenging times of this journey.

Finally, I express my gratitude to my family for their unwavering support and encouragement throughout my thesis.

Alexander Blom Larsen, Gothenburg, June 2024

List of Acronyms

Below is the list of acronyms that have been used throughout this thesis listed in alphabetical order:

CFD	Computational Fluid Dynamics
CHF	Critical Heat Flux
CHT	Conjugate Heat Transfer
DNB	Departure from Nucleate Boiling
HTC	Heat Transfer Coefficient
Modified HRIC	(Modified) High-Resolution Interface Capturing
ONB	Onset of Nucleate Boiling
PRESTO!	Pressure Staggered Option
QUICK	Quadratic Upstream Interpolation for Convective Kinematics
RGP	Real Gas Property
RPI	Rensselaer Polytechnic Institute
TPC	Thermal Phase Change
UDF	User Defined Function
VoF	Volume of Fluid

Nomenclature

Below is the nomenclature that has been used throughout this thesis listed in alphabetical order:

Bo	Boiling number
c_p	Specific heat capacity $[\frac{J}{kgK}]$
Eo	Eötvös number
f_D	Darcy friction factor
G	Mass flux $[\frac{kg}{m^2 s}]$
h	Convective heat transfer coefficient $[\frac{W}{m^2 K}]$
h_{lat}	Latent heat of vaporization $[\frac{J}{kg}]$
k	Conductive heat transfer coefficient $[\frac{W}{mK}]$
k	Turbulent kinetic energy $[K]$
L	Characteristic length $[m]$
Nu	Nusselt number
p	Pressure $[Pa]$
Pr	Prandtl number
q	Heat transfer rate $[W]$
q''	Heat flux $[\frac{W}{m^2}]$
Re	Reynolds number
R	Thermal resistance $[W^{-1}]$
T	Temperature $[K]$
ΔT	Temperature difference $[K]$
∇T	Temperature gradient $[K]$
u	Velocity $[\frac{m}{s}]$
$U_{overall}$	Overall heat transfer coefficient $[\frac{W}{m^2 K}]$
x	Vapour quality
X_{tt}	Martinelli parameter
α	Volume fraction

μ	Dynamic viscosity $[Pa * s]$
μ_T	Turbulent viscosity $[\frac{m^2}{s}]$
ρ	Density $[\frac{kg}{m^3}]$
$\bar{\bar{\tau}}$	Stress tensor
ω	Specific dissipation rate $[s^{-1}]$

Contents

List of Acronyms **ix**

Nomenclature **xi**

List of Figures **xvii**

List of Tables **xxi**

1 Introduction **1**

2 Theory **3**
2.1 Heat transfer . . . 3
2.1.1 Conduction . . . 3
2.1.2 Convection . . . 4
2.1.3 Heat Transfer Coefficient . . . 4
2.1.3.1 Single- and Multiphase Heat Transfer . . . 5
2.1.4 Boiling . . . 5
2.1.4.1 Pool Boiling . . . 6
2.1.4.1.1 Nucleate Boiling . . . 7
2.1.4.1.2 Transition Boiling . . . 7
2.1.4.1.3 Film Boiling . . . 7
2.1.4.2 Flow Boiling . . . 8
2.1.4.2.1 Bubbly Flow . . . 9
2.1.4.2.2 Plug Flow and Slug Flow . . . 9
2.1.4.2.3 Stratified and Wave Flow . . . 9
2.1.4.2.4 Annular Flow . . . 10
2.1.4.2.5 Mist Flow . . . 10
2.1.5 The “Boiling Crisis” . . . 11
2.1.6 Dimensionless numbers . . . 13
2.1.6.1 Reynolds number . . . 13
2.1.6.2 Nusselt Number . . . 13
2.1.6.3 Prandtl Number . . . 14
2.1.6.4 Boiling Number . . . 14
2.1.6.5 Martinelli Parameter . . . 15
2.1.6.6 Eötvös Number . . . 15
2.1.6.7 Weber Number . . . 16
2.1.6.8 Froude Number . . . 17

2.1.7 Experimental Correlations 18
2.1.7.1 Single-Phase Heat Transfer Correlations 18
2.1.7.1.1 Dittus-Boelter Correlation 18
2.1.7.1.2 Gnielinski Correlation 19
2.1.7.1.3 Petukhov-Popov Correlation 19
2.1.7.2 Single-Phase Pressure Drop Correlations 19
2.1.7.2.1 Darcy-Weisbach Correlation 19
2.1.7.3 Multiphase Heat Transfer Correlations 20
2.1.7.3.1 Chen's Correlation 20
2.1.7.3.2 Liu-Winterton's Correlation 21
2.1.7.3.3 Kandlikar's Correlation 22
2.2 Computational Fluid Dynamics 22
2.2.1 Governing Equations for Single-Phase Flows 23
2.2.1.1 Conservation of Mass 23
2.2.1.2 Conservation of Momentum 23
2.2.1.3 Conservation of Energy 24
2.2.2 Multiphase Modelling Frameworks 24
2.2.2.1 Mixture model 26
2.2.2.2 Lagrangian Particle Tracking 26
2.2.2.3 Eulerian-Eulerian 26
2.2.2.4 Volume of Fluid 26
2.2.2.5 Choice of Multiphase Modelling Frameworks for Analysis in This Thesis 26
2.2.3 Governing Equations for Multiphase Flows (Eulerian Framework) 27
2.2.3.1 Conservation of Mass 27
2.2.3.2 Conservation of Momentum 28
2.2.3.3 Conservation of Energy 29
2.2.4 Turbulence Modelling 29
2.2.4.1 RANS Modelling 29
2.2.4.1.1 The Boussinesq Hypothesis 30
2.2.4.2 Standard k-ε Model 31
2.2.4.3 Standard k-ω Model 32
2.2.4.4 k-ω Shear Stress Transport (SST) Model 32
2.2.4.5 Wall Functions and y^+ 33
2.3 Boiling modelling 36
2.3.1 Mass Transfer Modelling 36
2.3.1.1 Lee Model 38
2.3.1.2 Thermal Phase Change Model 40
2.3.2 Interfacial heat transfer modelling 42
2.3.2.1 Single-resistance approach 43
2.3.2.1.1 Nusselt number 43
2.3.2.1.2 Ranz-Marshall model 43
2.3.2.1.3 Hughmark model 44
2.3.2.1.4 Tomiyama model 44
2.3.2.1.5 Fixed to Saturation Temperature 44
2.3.2.2 Double-resistance approach 44

2.3.2.2.1 Lavieville (Constant Time Scale) Method . 45
2.3.2.2.2 Zero-resistance criteria 45
2.3.3 Interfacial momentum transfer modelling 45
2.3.3.1 Drag force 47
2.3.3.1.1 Schiller and Naumann model 47
2.3.3.1.2 Symmetric model 47
2.3.3.2 Lift force 48
2.3.3.2.1 Tomiyama model 48
2.3.3.3 Wall lubrication force 49
2.3.3.3.1 Antal et al. model 49
2.3.3.4 Virtual mass force 50
2.3.3.5 Turbulent dispersion force 50
2.3.3.5.1 Burns et al. model 50
2.3.4 Interfacial area modelling 51
2.3.4.1 Transport equation based model 51
2.3.4.1.1 Yao-Morel Model 52
2.3.4.2 Algebraic Models 53
2.3.4.2.1 Particle Model 53
2.3.4.2.2 Symmetric Model 54
2.3.5 Summary of boiling-related models 54

3 Experimental study **57**
3.1 Jige et al. 57
3.1.1 Layout and Specifications 58
3.1.1.1 Test Loop 58
3.1.1.2 Test section 59

4 Numerical modelling **61**
4.1 Mesh 61
4.1.1 Mesh independence study 61
4.2 Base solver configuration 66
4.3 Solution strategies 67
4.4 Convergence criteria 67

5 Results **69**
5.1 Numerical results 69
5.1.1 Single-phase simulations 69
5.1.1.1 Heat Transfer Coefficients 69
5.1.1.2 Pressure Drop 70
5.1.1.3 Summary 71
5.1.2 Multiphase Simulations 71
5.1.2.1 Test Cases 71
5.1.2.2 Survey of available sub models 72
5.1.2.2.1 Base configuration 72
5.1.2.2.2 Interfacial area modeling 73
5.1.2.2.3 Heat transfer modelling 76
5.1.2.2.4 Turbulence modelling 78

5.1.2.2.5 Force modelling 81
5.1.2.2.6 Summary 83
5.1.2.3 Comparison with experiments and correlations 84
5.1.2.3.1 Default coefficients 85
5.1.2.3.2 Tuned coefficients 87
5.1.2.3.2.1 Lee model 87
5.1.2.3.2.2 Thermal Phase Change model 88
5.1.2.3.3 Summary 89
5.1.2.4 Conjugate heat transfer 90
5.1.2.4.1 Mesh 90
5.1.2.4.2 Thin walls vs Thick walls 91
5.1.2.4.3 Single vs Double resistance models (thick walls) 93
5.1.2.4.4 Summary 95

6 Summary and Conclusions **97**
6.1 Recommendations for Future Work 98

Bibliography **99**

A Appendix A - Incremental Wall Flux UDF **I**

List of Figures

2.1 Flow chart showing the boiling patterns for pool and flow boiling. . . 6
2.2 The boiling curve, where wall heat flux is displayed versus wall superheat[1] [5]. 7
2.3 Schematic of flow boiling in a horizontally oriented tube [7]. 8
2.4 Images of different flow patterns observed in a horizontal, internal flow tube [8]. 9
2.5 Schematic of flow pattern, associated heat transfer mechanisms, and qualitative variation in HTCs for flow boiling in a horizontal tube [8]. 10
2.6 The boiling curve, a diagram of heat flux vs wall superheat [7]. 12
2.7 Bubble-shape diagram showing the dependence on Re and Eo [12]. . . 16
2.8 Temporal development of a droplet's shape with different Weber numbers [14]. 17
2.9 Schematic of different multiphase frameworks in CFD. 25
2.10 Schematic of a velocity profile (left), computational mesh required to resolve the steep gradient of flow variables (centre) and computed boundary layer profile (right) [34]. 33
2.11 Comparison of a piecewise-linear and a non-linear (wall function) approach [34]. 34
2.12 Diagram of dimensionless velocity and distance from the wall. Black line: Experimental and DNS data. Green line: log law. Blue line: $U^+ = y^+$ [34]. 35
2.13 Flow chart of the physical processes that require modelling in flow boiling. 36
2.14 Flow chart of the available boiling/ Evaporation models in ANSYS Fluent 2023R1 [28]. 37
2.15 Flow chart of the available boiling/ evaporation models compatible with the Eulerian framework in ANSYS Fluent 2023R1 [28]. 38
2.16 Heat transfer sub-models available for the Lee and TPC boiling models. 43
2.17 Schematic comparing single-resistance heat transfer (left) and double-resistance heat transfer (right). 45
2.18 Schematic of the interfacial forces acting on bubbles. (a) drag force, (b) lift force, (c) wall lubrication force, (d) virtual mass force, and (e) turbulent dispersion force [40]. 46

3.1 Schematic view of the experimental setup [52]. 58
3.2 Schematic view of the test section and the measurement points [52]. . 59

4.1 Cross-sectional view of the five meshes. 63
4.2 Axial view of the 200k cell mesh. 63
4.3 Plot of vapour quality against the no. of cells in each mesh. 65
4.4 Plot of wall temperature against the no. of cells in each mesh. 65
4.5 Example of the relative residuals of a converged solution. 67
4.6 Example of an area-averaged outlet volume fraction monitor for final simulation configuration for a multiphase case (that is, with the maximum wall heat flux and final solver configuration (spatial discretization). 68
4.7 Example of an area-averaged wall temperature monitor for final simulation configuration for multiphase case. 68

5.1 Plot of predicted HTC from single-phase heat transfer correlations and CFD against experimental data. 70
5.2 Plot of predicted pressure from single-phase correlations against CFD results. 70
5.3 Comparison of interfacial area models with the Lee model. Contours showing vapour volume fraction in the axial direction. 75
5.4 Comparison of interfacial area models with the Lee model. Contours showing vapour volume fraction in the radial direction (cross-sectional view of the test section outlet). 75
5.5 Comparison of interfacial area models with the Thermal Phase Change model. Contours showing vapour volume fraction in the axial direction. 76
5.6 Comparison of interfacial area models with the Thermal Phase Change model. Contours showing vapour volume fraction in the radial direction (cross-sectional view of the test section outlet). 76
5.7 Comparison of the single- and double-resistance approaches with the Thermal Phase Change model. Contours showing vapour volume fraction in the radial direction (cross-sectional view of the test section outlet). 77
5.8 Comparison of heat transfer models with the Thermal Phase Change model. Contours showing vapour volume fraction in the axial direction. 78
5.9 Comparison of turbulence models with the Lee model. Contours showing vapour volume fraction in the axial direction. 79
5.10 Comparison of turbulence models with the Lee model. Contours showing vapour volume fraction in the radial direction (cross-sectional view of the test section outlet). 80
5.11 Comparison of turbulence models with the Thermal Phase Change model. Contours showing vapour volume fraction in the axial direction. 80
5.12 Comparison of turbulence models with the Thermal Phase Change model. Contours showing vapour volume fraction in the radial direction (cross-sectional view of the test section outlet). 81
5.13 Comparison of different force configurations with the Lee model. Contours showing vapour volume fraction in the axial direction. 82
5.14 Comparison of different force configurations with the Lee model. Contours showing vapour volume fraction in the radial direction (cross-sectional view of the test section outlet). 83

5.15 Predicted HTCs of the Lee and Thermal Phase Change models with default coefficients for Case 1, compared against experimental data and correlations. 86
5.16 Predicted HTCs of the Lee and Thermal Phase Change models with default coefficients for Case 2, compared against experimental data and correlations. 86
5.17 Predicted HTCs of the Lee model with tuned coefficients for Case 1, compared against experimental data and correlations. 87
5.18 Predicted outlet volume fractions with increments of mass transfer coefficients in the Lee model. 88
5.19 Predicted HTCs of the TPC model with tuned coefficients for Case 1, compared against experimental data and correlations. 89
5.20 Cross-sectional view of the mesh including the tube wall thickness. . . 91
5.21 Axial view of the mesh including the tube wall thickness. 91
5.22 Comparison of modelling with and without CHT with the Lee model. Contours showing vapour volume fraction in the axial direction. . . . 92
5.23 Comparison of modelling with and without CHT with the Thermal Phase Change model (single-resistance). Contours showing vapour volume fraction in the axial direction. 92
5.24 Predicted HTCs of the mass transfer models with and without CHT for Case 1, compared against experimental data and correlations. . . 93
5.25 Comparison of the single- and double-resistance approaches with the Thermal Phase Change model and CHT. Contours showing vapour volume fraction in the axial direction. 94
5.26 Comparison of the single- and double-resistance approaches with the Thermal Phase Change model and CHT. Contours showing the temperature distribution in the axial direction (vapour temperature in the fluid domain and wall temperature in the solid domain). 94
5.27 Predicted HTCs of the single- and double-resistance approaches with the Thermal Phase Change model and CHT, compared against experimental data and correlations. 95

List of Tables

2.1 Comparison of multiphase frameworks. 25
2.2 Comparison of the source terms for the Lee and Thermal Phase Change models. 42
2.3 Overview of three closure models for the transport equation based model. 52
2.4 Comparison of the Lee and Thermal Phase Change models. 55
2.5 Interfacial momentum transfer sub-model choices. 55

3.1 Accuracy of the measurement instrumentation. 59

4.1 Properties of the five low-Re grids. 62
4.2 Numerical setup for the mesh independence study. 62
4.3 Spatial discretization schemes used for the single- and multiphase simulations. 66

5.1 Boundary conditions for the single-phase experiments. 69
5.2 Experimental conditions for the 3.5mm diameter tube. 71
5.3 Sub-models included in the base configuration. 72
5.4 Results from the interfacial area modelling analysis. Table shows area-averaged vapour quality at the heated section outlet and area-averaged wall temperature from the heated section wall. 74
5.5 Results from the heat transfer modelling analysis. Table shows area-averaged vapour quality at the heated section outlet and area-averaged wall temperature from the heated section wall. 77
5.6 Results from the turbulence modelling analysis. Table shows area-averaged vapour quality at the heated section outlet and area-averaged wall temperature from the heated section wall. 79
5.7 Results from the force modelling survey. Table shows area-averaged vapour quality at the heated section outlet and area-averaged wall temperature from the heated section wall. 82
5.8 Multiphase model configuration. 84

1
Introduction

The growing aviation industry is currently undergoing a transition to make aero engines more sustainable, efficient and environmentally friendly. As part of this transition, GKN Aerospace is investigating the incorporation of heat exchanger technology which has the potential to reduce specific fuel consumption (SFC) as well as enhance overall thermal efficiency of existing and future engines and engine cycles. In industrial heat exchangers, boiling is frequently used for heat recovery proposes, as utilizing the latent heat of vaporization ensures reliable heat transfer characteristics.

Multiphase flow modelling enables the analysis of flows and systems which incorporate these types of phenomena (i.e. boiling) by including mass, momentum, and heat transfer in the modelling approach. However, it presents computational difficulties due to the numerous and complex equations required to accurately represent the flow dynamics. Furthermore, achieving convergence in such numerical simulations often proves to be challenging.

Currently, various multiphase (and specifically boiling models) are available, each differing in complexity and sophistication. The RPI[1]model has been successfully applied and validated against flow boiling experiments [1], but it is highly complex and computationally demanding due to the modelling of sub-continua phenomena. Alternatively, evaporation / condensation models, such as the Lee and Thermal Phase Change models, which exclude sub-continua phenomena and convert any superheated or subcooled liquid or gas in the flow domain into vapour or liquid respectively, and are numerically simpler which make them potentially attractive alternatives to specific "boiling" models, such as the aforementioned RPI model.

These models have proven to be computationally cheaper and more stable but are derived from strong assumptions regarding the evaporation process. Therefore, this thesis will assess the accuracy and overall predictive capability of the Lee and Thermal Phase Change models for flow boiling.

[1]Rensselaer Polytechnic Institute

2
Theory

2.1 Heat transfer

Heat transfer is a field of thermal engineering concerning the exchange of heat transfer between physical systems or substances [2]. The driving force behind heat transfer is the temperature difference between the substances. The field is divided into thermal conduction, convection, and radiation, which all add up to the total heat transfer in a system:

$$q_{\text{cond}} + q_{\text{conv}} + q_{\text{rad}} = q_{\text{total}} = U_{\text{overall}} A \Delta T \tag{2.1}$$

where:

- $q_{\text{cond}}, q_{\text{conv}}, q_{\text{rad}}$ are the conductive, convective, and radiative heat transfer rates, respectively;
- q_{total} is the total heat transfer rate;
- U_{overall} is the overall heat transfer coefficient;
- A is the surface contact area; and
- ΔT is the temperature difference.

2.1.1 Conduction

Thermal conduction is the heat transfer that occurs principally through molecular collisions. When a substance is heated, its molecules closest to the heating source absorb thermal energy and collide with adjacent molecules, making the heat propagate throughout the substance. The ability of a substance to conduct heat is known as its thermal conductivity. The Fourier Rate Equation, also referred to as Fourier's First Law of Heat Conduction, can be seen in Eq. 2.2:

$$\frac{q_{\text{cond}}}{A} = -k \nabla T \tag{2.2}$$

where:

- q_{cond} is the conductive heat transfer rate;
- A is the surface contact area;
- ∇T is the temperature gradient; and
- k is the thermal conductivity of the medium.

In the above equation, the thermal conductivity, k, is assumed to be independent of direction which implies that the working medium is assumed to be isotropic. In many situations, this assumption is reasonable and many materials that are of engineering

interest most often can be considered isotropic. Further, the negative sign on the right-hand side denotes that the heat flow occurs in the direction of a decreasing temperature gradient.

2.1.2 Convection

Thermal convection involves heat transfer between a surface and a fluid through the movement of the fluid itself. There are two types of this phenomenon: natural and forced convection. Natural convection occurs when a region of the fluid is heated, its density decreases and the fluid starts to rise under the action of buoyancy forces, while the cooler and denser fluid descends, leading to circulation within the fluid, which further promotes the transfer of heat throughout the system.

Forced convection involves the transfer of heat through a fluid when an external force, such as a pump or a fan, is used to induce fluid motion. This pushes the warm fluid away and cold fluid onto the heated surface, resulting in a larger temperature difference which is the driving force for heat transfer.

In summary, natural convection relies on buoyancy and density differences within a fluid to generate the fluid motion, while forced convection involves external means (convective forces) which force the fluid to move and enhance heat transfer. Convective heat transfer (whether forced or natural), can be described mathematically by the Newton Rate Equation, see Eq. 2.3.

$$\frac{q_{\text{conv}}}{A} = h\Delta T \tag{2.3}$$

where:

- q_{conv} is the convective heat transfer rate;
- A is the area normal to the flow direction;
- ΔT is the temperature difference between the surface and the fluid; and
- h is the convective heat-transfer coefficient.

Observe that the coefficient h is dependent on the system geometry, properties of the fluid and the flow, and the magnitude of ΔT.

2.1.3 Heat Transfer Coefficient

The overall heat transfer coefficient, U_{overall}, is expressed mathematically in Eq. 2.4:

$$U_{\text{overall}}A = \frac{1}{A\sum R_i} = \left(\frac{L}{kA} + \frac{1}{hA}\right)^{-1} \tag{2.4}$$

where:

- R_i is the thermal resistance of heat transfer mechanism i; and
- L is the thickness of the conductive medium.

Since, in general, heat exchangers do not operate at sufficiently high temperatures for thermal radiation to be significant (i.e. above 1000K [3]), further discussion of this mechanism will not be included in this thesis.

2.1.3.1 Single- and Multiphase Heat Transfer

Multiphase heat transfer is more complex than that of single-phase since different phase states of the same substance have different material properties (e.g. density or thermal conductivity), which results in fundamentally different heat transfer characteristics for multiphase flows in comparison to single-phase flows.

Latent heat of vaporization[1] denotes the quantity of heat introduced into or withdrawn from a substance to induce a change in its phase. It is expressed in Eq. 2.5 as the enthalpy difference between saturated liquid and gas. This energy breaks down the intermolecular attractive forces and must provide the energy necessary to expand the gas.

$$h_{\text{lat}} = h_{\text{sat,vapour}} - h_{\text{sat,liquid}} \tag{2.5}$$

The saturation temperature at a given pressure is the temperature when the fluid starts to undergo phase change. For evaporation, this means that any additional thermal energy added to the system will contribute to the phase change process. This is beneficial in industrial applications, since the stability in temperature ensures that the substance involved absorbs or releases a consistent amount of heat energy without experiencing large fluctuations in temperature.

2.1.4 Boiling

Boiling is a phase change phenomenon when a liquid substance undergoes rapid vaporization and transforms into a gaseous state, creating discrete gas-liquid interfaces when subjected to a heat flux from a surface maintained above the saturation temperature of the substance [4], [5]. The phase change process starts at the boiling point of the liquid, which is defined as the temperature at which the vapour pressure of a liquid is equal to the surrounding pressure. Although strictly speaking, boiling and evaporation are distinct processes from one another, these terms are used interchangeably in this thesis.

In contrast to other heat transfer processes, the natural occurrence of water boiling is uncommon, typically occurring naturally in only reasonably isolated occurrences e.g. when submarine volcanoes erupt releasing heat into the surrounding water and causing localised boiling to occur.

Boiling distinguishes itself from other convection processes since it relies on the latent heat of vaporization, which is very large for typical pressures. Consequently, significant amounts of thermal energy can be transferred while maintaining a stable temperature during the process. The reliable heat transfer characteristics is the reason boiling is frequently leveraged in industrial processes for heat recovery purposes.

Different boundary conditions, such as heat flux, mass flux, inlet water temperature, vapour quality, and inner tube diameter, will cause various flow patterns to emerge in the boiling regime. Fig. 2.1 shows a schematic of the multitude of possible boiling patterns which under different conditions.

[1] Often termed simply "latent heat"

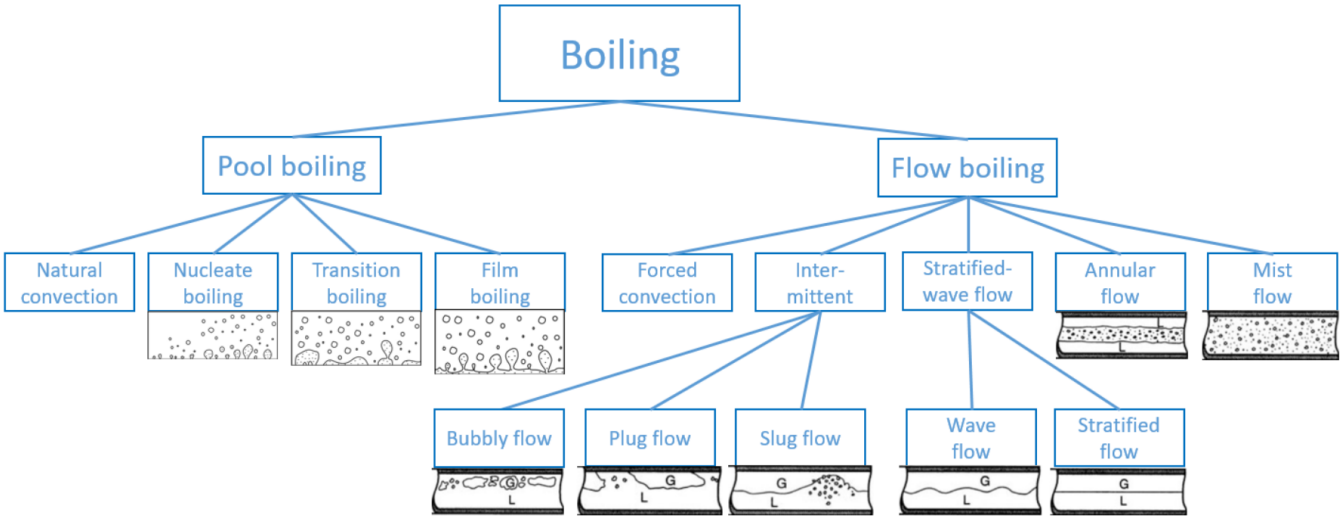

Figure 2.1: Flow chart showing the boiling patterns for pool and flow boiling.

2.1.4.1 Pool Boiling

The most common configuration of boiling is when a pool of quiescent liquid is subjected to heat from an adjacent horizontal surface, commonly referred to as pool boiling [5].

In 1934, Nukiyama presented the first boiling curve [6]. This curve shows the interdependence of the heat flux input and the wall superheat temperature, the latter being defined as the difference between the wall temperature and the saturation temperature of the working medium.

Nukiyama was able to identify various pool boiling regimes through the use of his apparatus. Since the publication of his original work, further investigations by Nukiyama have led to improvements of the boiling curve into a better depiction of the boiling phenomena (see Fig. 2.2).

Every segment of the boiling curve signifies a distinct pool boiling regime:

- Natural convection;
- Nucleate boiling;
- Transition boiling; and
- Film boiling

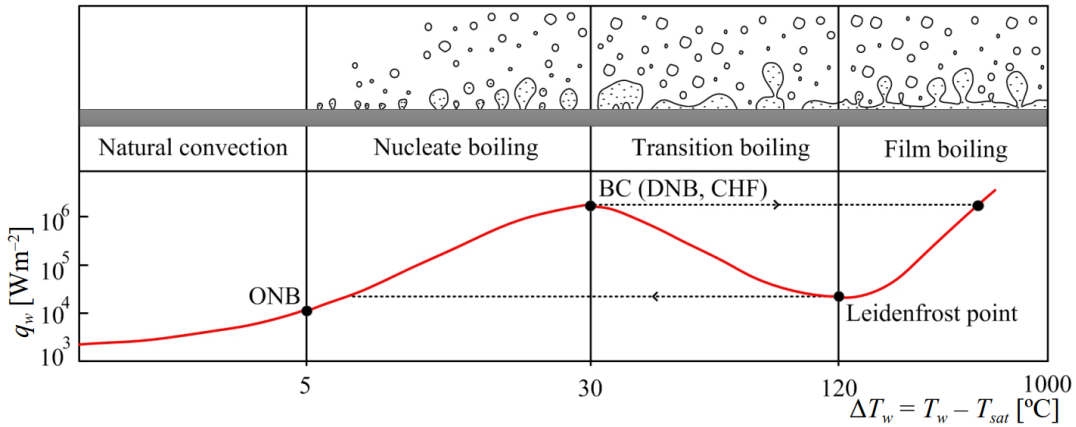

Figure 2.2: The boiling curve, where wall heat flux is displayed versus wall superheat[2] [5].

2.1.4.1.1 Nucleate Boiling

In the process of nucleate boiling, vapour bubbles form on the heating surface, detach, and get carried along with the main flow of the fluid. This is referred to as the Onset of Nucleate Boiling or ONB, as shown in Fig. 2.2.

This phenomenon plays a crucial role in enhancing heat transfer since the heat generated at the surface is directly transported into the fluid stream. Upon entering the bulk flow, the bubbles collapse due to the lower bulk temperature.

Consequently, nucleate boiling significantly improves a surface's capability to transfer thermal energy to the bulk fluid.

2.1.4.1.2 Transition Boiling

So-called "transition boiling" occurs as the wall temperature increases and vapour forms at a faster pace and starts to cover more of the wall area. Due to the significantly lower thermal conductivity of the vapour phase compared to the liquid phase, the wall heat flux reaches a limit, called the Critical Heat Flux (CHF).

At this point, in temperature-controlled systems, any increase in wall superheat will cause the heat transfer rate to decrease and the system will enter the transition boiling regime. The negative slope of the boiling curve signifies the transition of the contact condition on the heated surface, changing from a partial liquid film to a fully formed vapour layer.

2.1.4.1.3 Film Boiling

For systems in which the wall heat flux is controlled, any further increase leads to the formation of a vapour layer over the walls. Consequently, the wall temperature

[2]The difference between the wall temperature and the saturation temperature of the liquid at a given pressure

rises rapidly, causing the system to jump from the above-mentioned CHF point to the film boiling regime. The abrupt rise in wall temperature can induce permanent damage to the heat exchanger equipment, commonly known as burnout.

2.1.4.2 Flow Boiling

In flow boiling, fluid flow is induced over a heated surface through external means, for instance, via a pump (see Fig. 2.3). Flow boiling is further categorized as either internal or external, relying on whether the fluid is forced to flow inside a heated channel or over a heated surface. The orientation of the channel also affects the flow behaviour, since for vertical channels gravity acts in the same or opposite direction of the flow. In horizontal channels, vapour tends to accumulate at the upper part of the tube due to the density difference with the corresponding liquid.

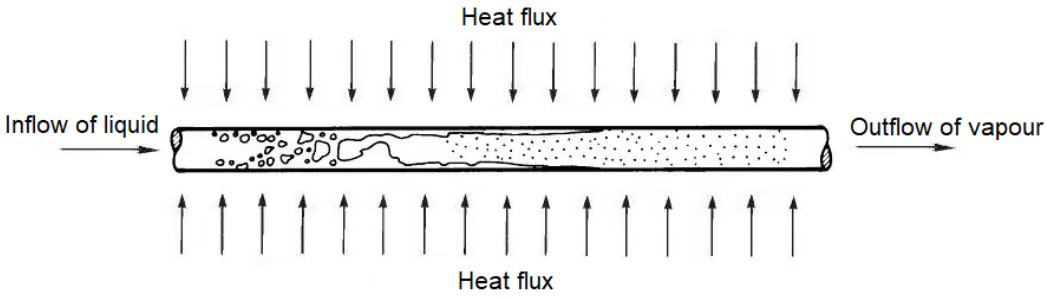

Figure 2.3: Schematic of flow boiling in a horizontally oriented tube [7].

Two-phase flows can take many different forms depending on the operating conditions and which stage of boiling the system is at. The spatial distributions and velocities of the liquid and vapour phases in the flow channel play a critical role in determining the overall behaviour and characteristics of the two-phase flow.

The flow structure influences phenomena such as heat transfer rates, pressure drop, and flow stability, making them essential considerations in the analysis and design of boiling systems. Below is a list of the main flow regimes observed in internal flows, ordered by the increment of vapour quality:

- Bubbly flow;
- Plug and slug flow;
- Wave flow;
- Stratified flow;
- Annular flow; and
- Mist flow.

For context, Fig. 2.4 shows a series of images of the typical flow regimes, which occur in horizontal tubes.

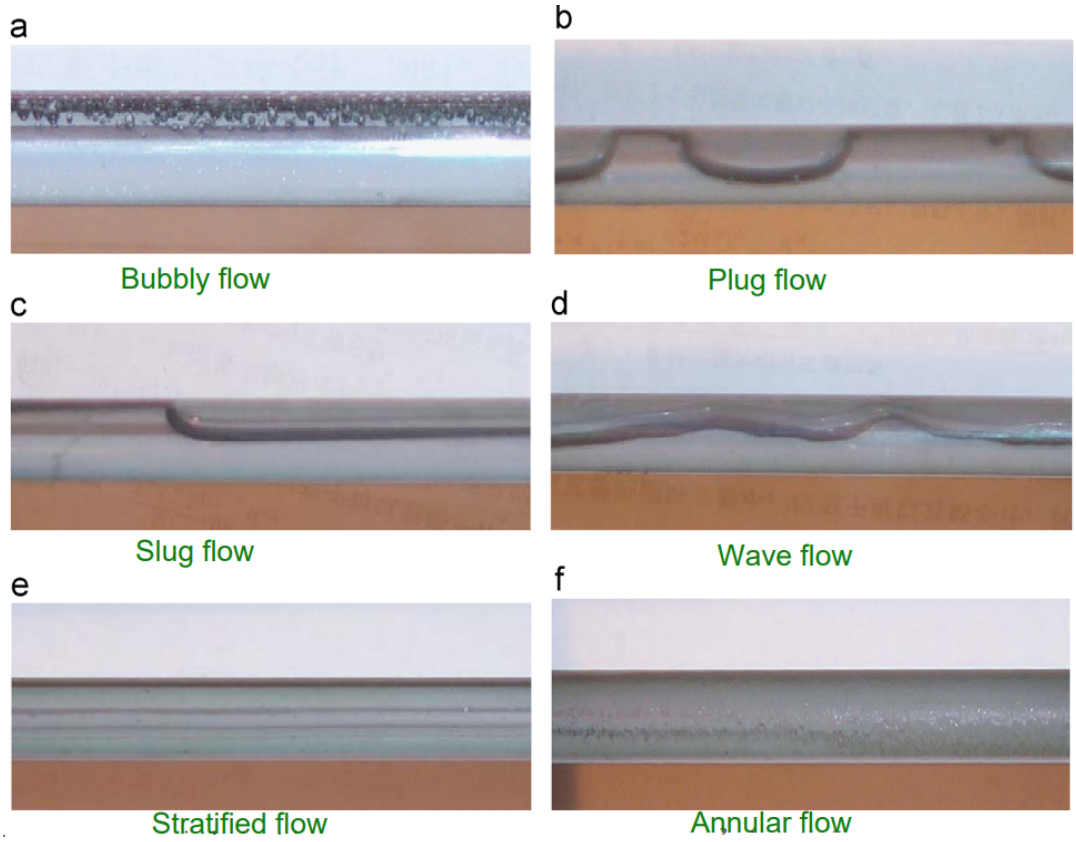

Figure 2.4: Images of different flow patterns observed in a horizontal, internal flow tube [8].

2.1.4.2.1 Bubbly Flow

Bubbly flow is a flow pattern characterized by vapour bubbles starting to form at nucleation sites on the wall, usually uneven parts of the surface. This is commonly referred to as the onset of nucleate boiling (ONB) and happens when the liquid adjacent to the wall is at its saturation temperature and starts to evapourate. The bubbles grow larger and eventually detach from the nucleation site and are completely surrounded by liquid. This is called quenching and transfers the heat through the liquid-vapour interface as the bubble traverses to the bulk flow. Due to the density difference between the phases, the bubbles accumulate at the top of the horizontal tube.

2.1.4.2.2 Plug Flow and Slug Flow

As the vapour quality increases, the bubbles start to coalesce into larger plugs and eventually slugs. These slug bubbles continue to grow and will eventually become almost as large as the tube itself.

2.1.4.2.3 Stratified and Wave Flow

At sufficiently low flow rates, the vapour phase will completely cover the upper part of the tube and waves start to form at the interface, commonly referred to as wave

flow. After some time, the waves will calm down and the flow becomes completely stratified. Note that these flow regimes only appear with certain operating conditions, unlike bubbly flow, which appears in almost every case and precedes all the other flow regimes.

2.1.4.2.4 Annular Flow

When the slugs continue to grow, they start coalescing and the bulk flow will eventually only consist of vapour phase, while a liquid film starts to form at the walls. This is known as annular flow.

2.1.4.2.5 Mist Flow

When the vapour quality reaches a sufficiently high level, the liquid film encapsulating the tube wall starts to evapourate and the remaining liquid gets ejected into the bulk flow in the form of droplets. Eventually, the walls are completely covered by the vapour phase and the droplets in the bulk flow evapourate due to the heat from the surrounding vapour.

Fig. 2.5 includes a schematic of the development and transitions of the flow regimes in a typical boiling type, as well as the corresponding heat transfer coefficients plotted against vapour quality. It is noticeable that the HTC increases up to the transition from annular flow to mist flow.

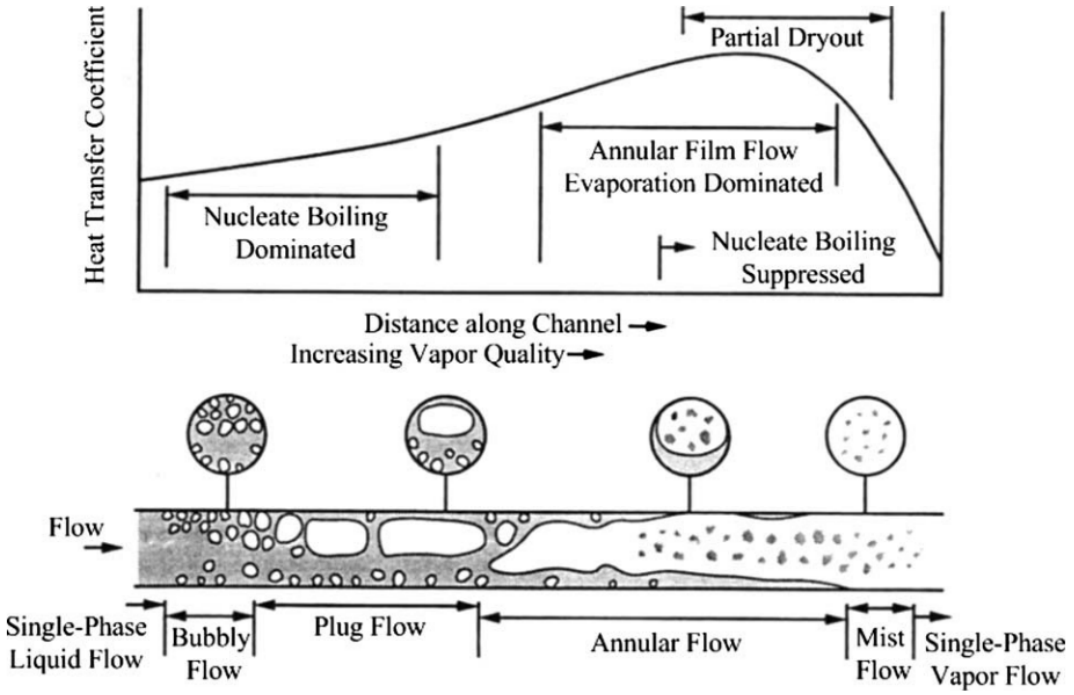

Figure 2.5: Schematic of flow pattern, associated heat transfer mechanisms, and qualitative variation in HTCs for flow boiling in a horizontal tube [8].

2.1.5 The "Boiling Crisis"

As discussed previously, a critical heat flux (as described above) is eventually reached with the increment of wall superheat, also referred to as the Departure from Nucleate Boiling (DNB) [5].

The changes in boiling behaviour that occur upon surpassing the CHF are widely known as the "boiling crisis". At this point, the boiling system will pursue one of two different paths.

For power-controlled systems, when the wall heat flux is allowed to further increase, a vapour film will form at the walls and the system will cross the boiling curve to the film boiling regime immediately. This brings a significant rise in the wall superheat which can damage the heating surface, referred to as burn-out, or even cause the metal tubes to melt.

Alternatively, for temperature-controlled systems, an increment of wall superheat will result in a decrease in the wall heat flux and the boiling system will go into the transition boiling regime. The downward slope observed in this regime is attributed to the change in contact condition on the heated surface, shifting from a partial liquid film to a complete vapour film.

Observe the point at which the transition and film boiling regimes meet (see Fig. 2.6), this is called the Leidenfrost point. This phenomenon was first reported by Johann Gottlob Leidenfrost in 1756, while analyzing the behaviour of water droplets on hot metal surfaces [5]. He observed that the time required for droplets to evapourate on extremely hot surfaces was longer compared to those on surfaces with moderate temperatures. The cause of this phenomenon arises from the rapid formation of an insulating vapour film on the heated surface, which hinders rapid vaporization due to the lower thermal conductivity of water vapour.

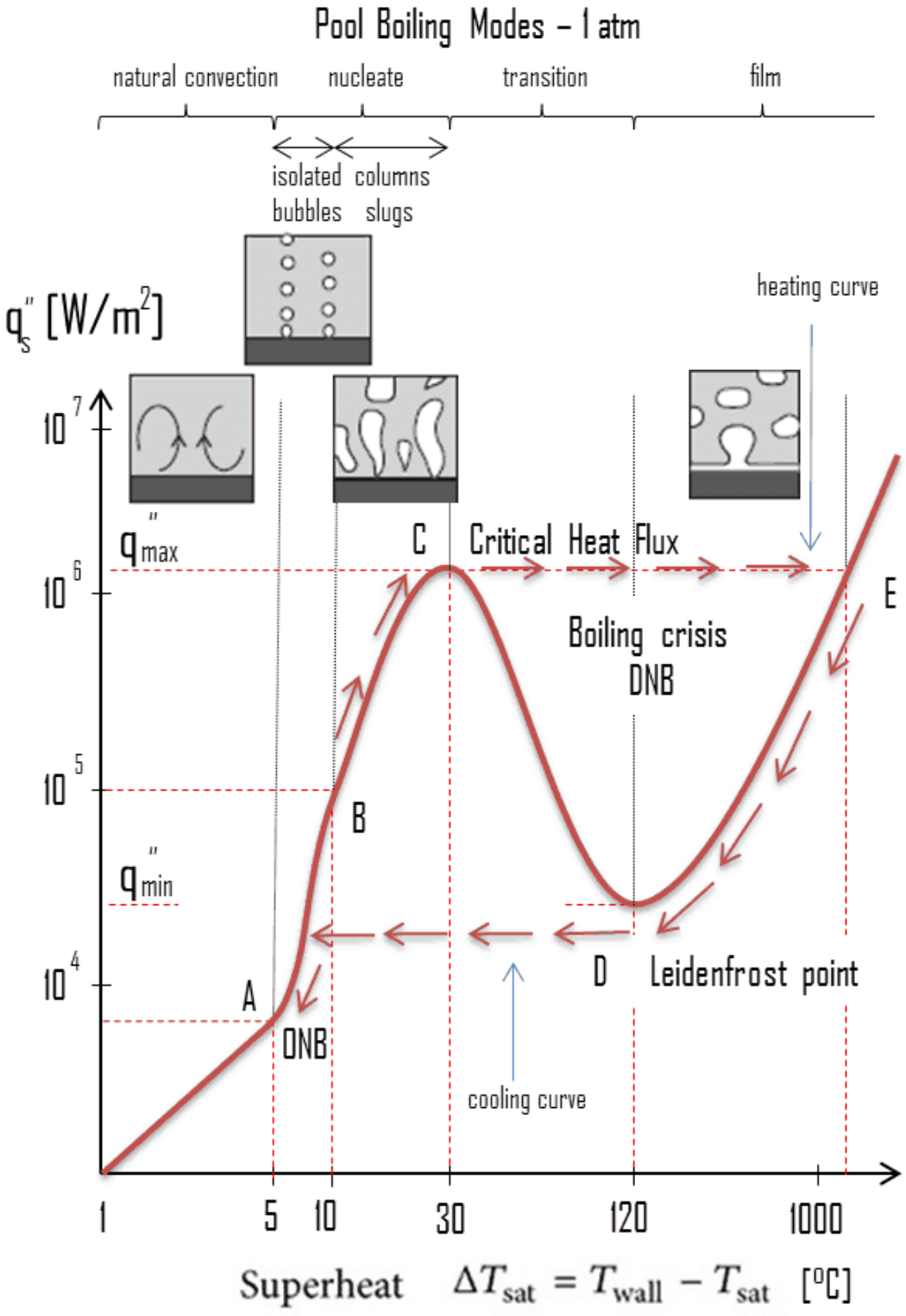

Figure 2.6: The boiling curve, a diagram of heat flux vs wall superheat [7].

Since the ultimate objective in employing heat removal through boiling is to leverage the latent heat of vaporization for transferring a substantial amount of heat while minimizing the rise in temperature of the cooling medium, the aim of most systems

is to attain the highest possible heat flux magnitudes while ensuring operation within the nucleate boiling regime. Operating a boiling system beyond this regime can results in permanent damage to the cooling equipment.

2.1.6 Dimensionless numbers

Depending on the characteristics of a multiphase flow, different forces and phenomena will be more significant, and it can be challenging to know in advance which of them can be neglected and which require modeling. Dimensionless numbers can be of great assistance to conclude the relative importance of various phenomena on the flow behaviour.
Listed below are the most important dimensionless numbers in boiling flows, on which many of the experimental correlations and computational models rely.

2.1.6.1 Reynolds number

Reynolds number is defined as the ratio of inertial and viscous forces in a fluid. It is useful for characterizing the flow behaviour in a certain domain, more specifically if the flow is turbulent (chaotic) or laminar (ordered).

$$\mathrm{Re} = \frac{\rho u L}{\mu} \tag{2.6}$$

where:

- ρ is the fluid's density;
- u is the velocity of the flow;
- L is the characteristic length of the domain; and
- μ is the fluid's dynamic viscosity.

In flows characterized by low Reynolds numbers, the viscous forces dominate and the flow is said to be laminar, characterized by even and constant fluid motion. For pipe flows, laminar flow is observed for flows with $\mathrm{Re} < 2300$.

In high Reynolds numbers flows, the inertial forces dominate and the flow is described as turbulent, characterized by its chaotic behaviour in which eddies and other flow instabilities appear. In pipe flows, turbulent flow is observed for conditions at which $\mathrm{Re} > 3500$. The chaotic nature of turbulence increases mixing of the fluid, which enhances heat transfer in the domain.

Finally, for pipe flows with $2300 < \mathrm{Re} < 3500$, the flow is described transitional, in which the flow transitions from laminar to turbulent, or vice versa.

2.1.6.2 Nusselt Number

Nusselt number describes the relative strength of convective to conductive heat transfer in a fluid. For low Nusselt numbers, the fluid is stagnant or moving very slowly and the heat transfer within the flow is dominated by the conductive heat transfer capacity of the flow, leading to a decrease in the temperature difference

between the fluid and the heated surface over time, and consequently a decrease in overall heat transfer rate with time.

For high Nusselt numbers, characterized by strong action of the convection forces of the fluid, the locally heated fluid adjacent to the heated surface is continuously replaced with cooler fluid, leading to the temperature difference between the heated surface and the fluid remaining high, and thus resulting in an overall increased heat transfer rate.

$$\mathrm{Nu} = \frac{hL}{k} \tag{2.7}$$

where:

- h is the convective heat transfer coefficient;
- L is the characteristic length of the domain; and
- k is the conductive heat transfer coefficient.

2.1.6.3 Prandtl Number

The Prandtl number outlines the relative importance of momentum diffusivity to thermal diffusivity. In other words, it describes how thermal energy is transferred versus how momentum is transferred through the fluid domain.

$$\mathrm{Pr} = \frac{\nu}{\alpha} = \frac{c_p \mu}{k} \tag{2.8}$$

where:

- ν is the momentum diffusivity of the fluid;
- α is the thermal diffusivity of the fluid;
- c_p is the specific heat capacity of the fluid;
- μ is the dynamic viscosity of the fluid; and
- k is the conductive heat transfer coefficient.

Highly viscous fluids, such as honey, transfer momentum more slowly than heat. Consequently, they diffuse thermal energy faster and have higher Prandtl numbers. In contrast, fluids with low viscosity, like air, transfer momentum more easily than heat, resulting in low Prandtl numbers. Additionally, Pr defines the relative thickness of the thermal and momentum boundary layers. A Prandtl number of $\mathrm{Pr} = 1$ indicates that the thermal and momentum boundary layers will have the same thickness.

2.1.6.4 Boiling Number

Boiling number is defined as the ratio of liquid mass evapourated per area heat transfer surface to fluid mass flow rate per flow cross-sectional area [9]:

$$\mathrm{Bo} = \frac{q}{G_l h_{\mathrm{lat}}} \tag{2.9}$$

where:

- q is the heat flux;
- G_l is the two-phase mass flux in the domain; and
- h_{lat} is the latent heat of the fluid.

It describes the relevance of convective heat transfer compared to the influence of vaporization. If Bo > 1, it indicates that convective heat transfer is the dominant heat transfer mechanism, and if Bo < 1, vaporization (bubble formation) is the dominant heat transfer mechanism. It is useful for determining the heat transfer behaviour of internal flows and is widely used in experimental correlations.

2.1.6.5 Martinelli Parameter

In 1949, Lockhart and Martinelli proposed a set of parameters used in correlations for the prediction of pressure drop in smooth tubes with isothermal two-phase flows [10]. It essentially acts as a correction factor in two-phase heat transfer correlations, where it suppresses the forced convection and enhances the nucleate boiling [11].

In most flow boiling cases, both the liquid and vapour phase will be flowing turbulently, hence the correlations employ the Martinelli parameter specifically for turbulent-turbulent flows, expressed as:

$$X_{\mathrm{tt}} = \left(\frac{1 - x_e}{x_e}\right)^{0.9} \left(\frac{\rho_v}{\rho_l}\right)^{0.5} \left(\frac{\mu_l}{\mu_v}\right)^{0.1} \tag{2.10}$$

where:

- x_e is the equilibrium vapour quality, a ratio of the actual vapour mass in the mixture to the vapour mass at equilibrium;
- ρ_v is the density of the vapour phase;
- ρ_l is the density of the liquid phase;
- μ_l is the dynamic viscosity of the liquid phase; and
- μ_v is the dynamic viscosity of the vapour phase.

2.1.6.6 Eötvös Number

Eötvös number is a dimensionless number used to assess the significance of buoyancy forces relative to surface tension forces acting on a bubble [12]. It is useful for predicting the shape of the bubbles in a fluid domain (see Fig. 2.7). A low value of Eö signals that surface tension will dominate over buoyancy, hence the bubble will exhibit a spherical shape. On the contrary, a high value indicates that buoyancy will be the dominant force, resulting in a distorted bubble shape, depending on Re. The shape of the bubbles, in turn, characterizes the flow regimes and affects the interfacial dynamics, most notably the momentum transfer.

$$\mathrm{Eo} = \frac{(\rho_L - \rho_G) g D^2}{\sigma} \tag{2.11}$$

where:

- g is the gravitational acceleration;
- D is the bubble diameter; and
- σ is the surface tension.

This number is commonly used in lift force correlations, where the shape of the bubble interface will greatly impact the behaviour of the lift force [13].

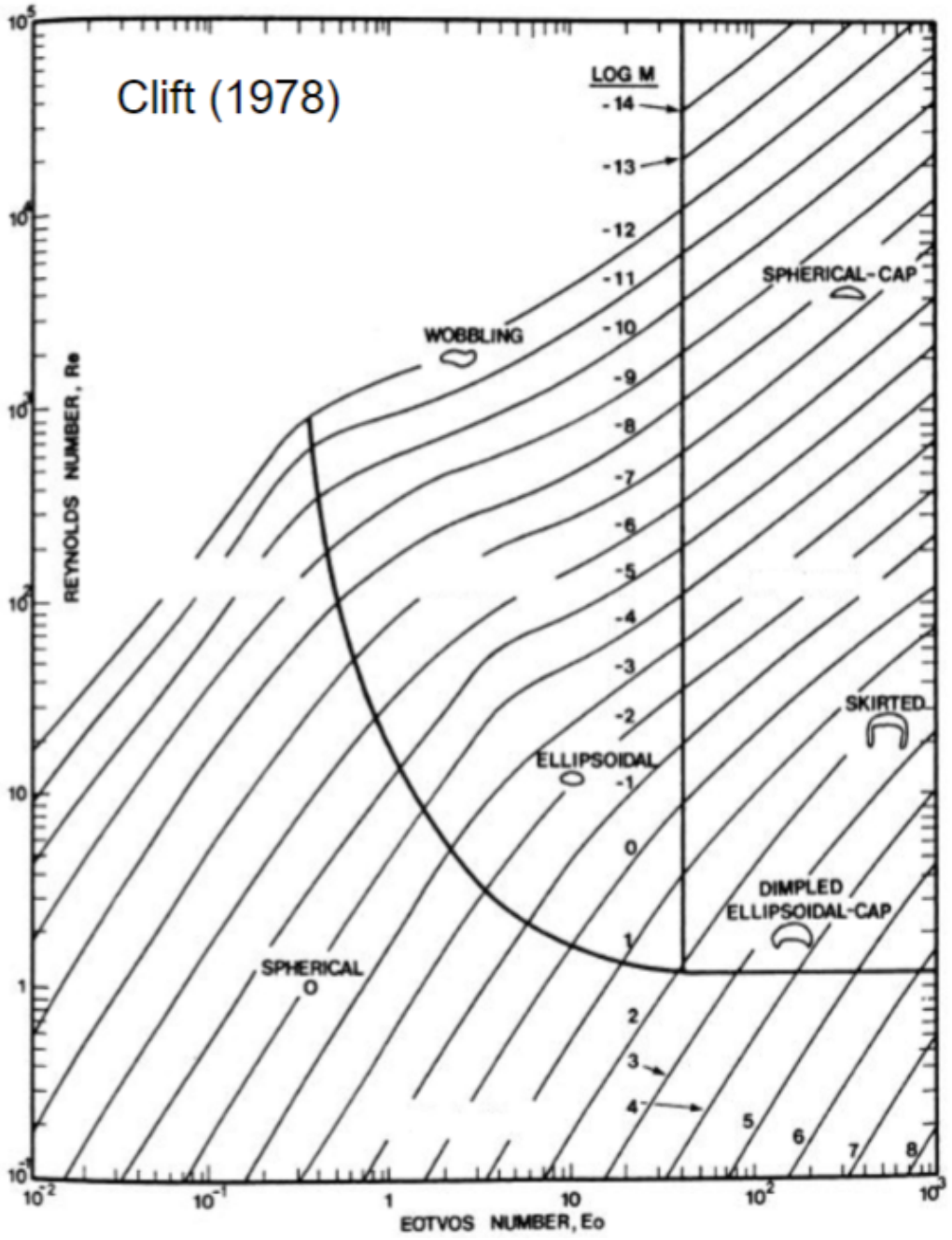

Figure 2.7: Bubble-shape diagram showing the dependence on Re and Eo [12].

2.1.6.7 Weber Number

The Weber number describes the relative importance of a bubble or droplet's inertial forces and its surface tension forces. Similar to the Eötvös number, it describes the shape of dispersed fluid particles. The Weber number is mathematically expressed as:

$$\mathrm{We} = \frac{(\rho_l u_t^2 d_b)}{\sigma} \tag{2.12}$$

An instance where the Weber number plays a crucial role is when a boiling flow exhibits mist flow, and the vapour phase has become the primary phase. The shear stress that the vapour flow in the center of the tube exerts on the liquid film at the walls could grow so strong that it pulls off droplets into the vapour flow. The inertial forces acting on the liquid film become so strong that they overpower the surface tension of the liquid, resulting in a high Weber number. The entrained droplets will have heavily distorted interface shapes depending on the relative strength of the inertial forces.

Another instance is when a droplet falls onto a surface. Depending on the Weber number, it will take different amounts of time for the liquid droplet to collapse and form a film (see Fig. 2.8).

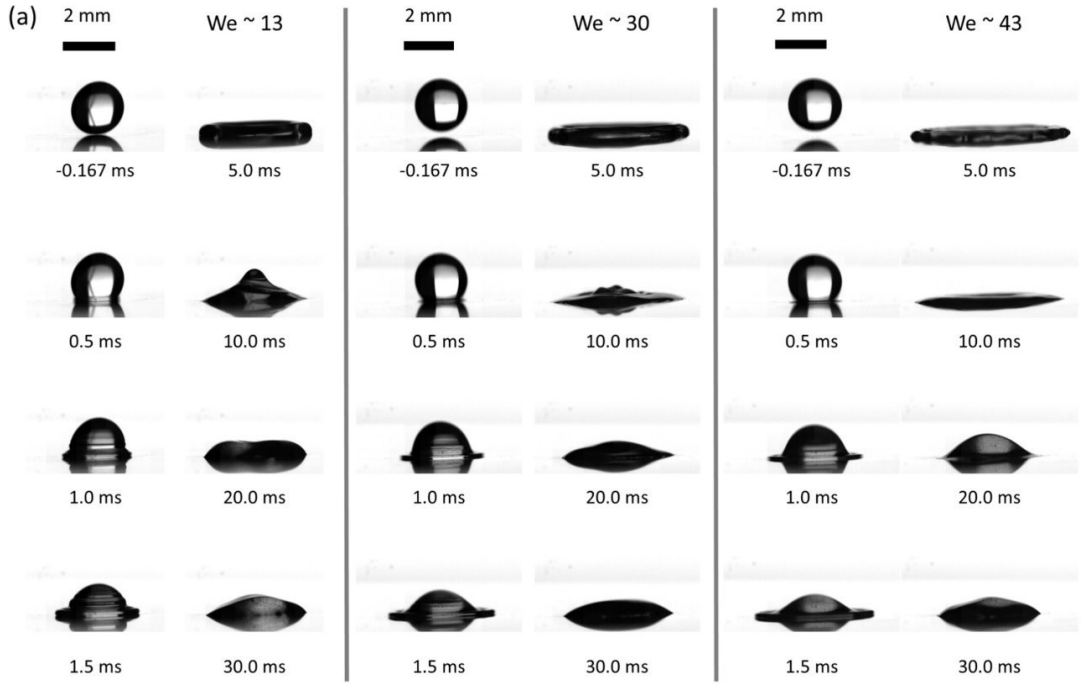

Figure 2.8: Temporal development of a droplet's shape with different Weber numbers [14].

2.1.6.8 Froude Number

The Froude number, which is a dimensionless number describing the relationship between gravitational and inertial forces, is significant for the geometry combination with the working medium in this thesis, as it introduces asymmetry in the flow due to the importance of gravitational forces [15]. In flow boiling, it is useful for determining the extent to which the fluid will be influenced by the orientation of the channel.

For large Fr, inertial forces will dominate over gravitational forces, resulting in symmetric flow patterns and heat transfer. Conversely, for small Fr, gravitational forces will significantly affect the fluid, resulting in asymmetric flow patterns and heat transfer.

The Froude number is defined as:

$$\mathrm{Fr} = \frac{G^2}{(\rho_l^2 g L)} = \frac{u}{\sqrt{gL}} \tag{2.13}$$

where:

- u is the velocity;
- g is the gravitational acceleration; and
- L is the characteristic length.

2.1.7 Experimental Correlations

Engineers with the aim of designing heat exchanger equipment are faced with a significant challenge due to the lack of precise and comprehensive predictive tools for boiling heat transfer [5].

Despite the apparently straightforward relationship depicted in the boiling curve and the underlying phenomenological descriptions of the mechanisms, a universal methodology for predicting heat transfer across different boiling regimes does not currently exist.

To fully understand and be able to predict the behaviour of a specific heat exchanger design, it is necessary to conduct experimental investigations involving numerous important parameters.

To circumvent the costly and time-consuming effort when designing boiling equipment, various researchers have developed empirical correlations for predicting HTCs and CHF values. However, these correlations are only applicable for certain ranges of operating conditions and often rely on empirical parameters calibrated by experimental data collected under limited ranges of parameters.

2.1.7.1 Single-Phase Heat Transfer Correlations

In single-phase flows, heat transfer characteristics can be accurately modeled with simple correlations based on fundamental dimensionless numbers. Below, some well-known correlations are presented.

2.1.7.1.1 Dittus-Boelter Correlation

The Dittus-Boelter correlation is a heat transfer correlation for turbulent flows which calculates the Nusselt number based on the Reynolds and Prandtl numbers, expressed as [16]:

$$\mathrm{Nu} = 0.023 \mathrm{Re}^{0.8} \mathrm{Pr}^{0.4} \frac{k_l}{d_{\mathrm{in}}} \tag{2.14}$$

This relation is applicable for internal flows in smooth tubes with Re $>$ 10,000, $0.6 < \mathrm{Pr} < 160$ and $\frac{L}{d} > 10$ [17]. The correlation is easily solved but lacks accuracy for fluid domains with large temperature differences.

2.1.7.1.2 Gnielinski Correlation

The Gnielinski correlation is a heat transfer correlation for forced convection in turbulent flows in horizontal tubes, valid for a wider range of Reynolds numbers including the transition region, expressed as [18]:

$$\mathrm{Nu} = \frac{\left(\frac{f_d}{8}\mathrm{Re} - 1000\right)\mathrm{Pr}}{1 + 12.7\left(\frac{f_d}{8}\right)^{1/2}\left(\mathrm{Pr}^{2/3} - 1\right)} \tag{2.15}$$

where f_d is the Darcy friction factor,a dimensionless friction coefficient accounting for friction losses in the tube. It is also used in the Darcy-Weisbach pressure drop correlation, presented in Section 2.1.7.2.1.

2.1.7.1.3 Petukhov-Popov Correlation

Similar to the Gnielinski correlation, the Petukhov-Popov correlation describes heat transfer for turbulent flows in horizontal tubes, expressed as [19]:

$$\mathrm{Nu} = \frac{\frac{f_f}{8}\mathrm{RePr}}{1 + 3.4f_f + \left(11.7 + \frac{1.8}{\mathrm{Pr}^{1/3}}\right)\left(\frac{f_f}{8}\right)^{1/2}\left(\mathrm{Pr}^{2/3} - 1\right)} \tag{2.16}$$

where $f_f = \frac{f_d}{4}$ is the Fanning friction factor.

2.1.7.2 Single-Phase Pressure Drop Correlations

For turbulent flows in internal channels, such as tubes, there will be frictional losses between the free-stream flow and the boundary layer forming near the walls. This results in pressure loss which is accentuated with higher Reynolds numbers. High pressure drops are unwanted in tube flows since they lead to energy losses, reduced efficiency, and even damages to the equipment as a result of flow instability. However, turbulence increases mixing of the fluid which enhances heat transfer, hence, a compromise between these factors needs to be reached.

The most common equation for predicting the pressure loss in a tube configuration is the Darcy-Weisbach equation, thanks to its accuracy and simple formulation.

2.1.7.2.1 Darcy-Weisbach Correlation

The Darcy-Weisbach correlation is expressed as [20]:

$$\frac{\Delta p}{L} = f_d \frac{\rho}{2}\frac{u^2}{d} \tag{2.17}$$

where:

- Δp is the pressure drop;
- L is the length of the tube;
- f_d is the Darcy friction factor;
- ρ is the bulk density;
- u is the bulk velocity; and

- d is the diameter of the tube.

The Darcy-Weisbach correlation relies on the so-called Darcy friction factor, which itself can be calculated using different correlations. In this thesis, the following correlations will be used:

- **Blasius Correlation** [21]:

$$f_d = 0.3164\, Re^{-1/4} \tag{2.18}$$

This correlation is valid for smooth tubes with turbulent flow, $4000 < Re < 10^5$.

- **Moody Correlation** [22]:

$$f_d = 0.0055 \left[1 + \left(2 \times 10^4 \frac{\varepsilon}{d} + \frac{10^6}{Re}\right)^{1/3}\right] \tag{2.19}$$

where ε/d is the tube's relative roughness, which equals zero for smooth tubes. This correlation is valid for $4000 < Re < 10^8$, $0 \leq \varepsilon/d \leq 0.01$.

- **Eck Correlation** [23]:

$$\sqrt{\frac{1}{f_d}} = -2 \log\left(\frac{\varepsilon/d}{3.715} + \frac{15}{Re}\right) \tag{2.20}$$

The valid range for this correlation was not found.

2.1.7.3 Multiphase Heat Transfer Correlations

There have been attempts to capture the complexities of two-phase heat transfer in semi-empirical correlations for decades. None of them have so far been able to predict the heat transfer characteristics of several two-phase systems with high accuracy [11].

Nonetheless, it is interesting to analyse the difference in accuracy between numerical simulations and correlations with regards to experimental data. In this section, some of the most well-known two-phase heat transfer correlations are presented.

2.1.7.3.1 Chen's Correlation

Chen's correlation aims to include the effects of phase change heat transfer by using a correlation derived from pool boiling experiments [11]:

$$h_{pb} = 0.00122 \frac{k_l^{0.79} c_{p,l}^{0.45} \rho_l^{0.49} g^{0.25}}{\sigma^{0.5} \mu_l^{0.29} h_{lat}^{0.24} \rho_g^{0.24}} \Delta T_{sat}^{0.24} \Delta p_{sat}^{0.75} \tag{2.21}$$

where:

- h_{pb} is the heat transfer coefficient of the pool boiling;
- k_l is the liquid thermal conductivity;
- $c_{p,l}$ is the liquid specific heat capacity;
- ρ_l, ρ_g are the phase densities;
- g is the gravitational acceleration;

- σ is the interfacial surface tension;
- h_{lat} is the latent heat;
- ΔT_{sat} is the difference between wall temperature and saturation temperature of the fluid;
- Δp_{sat} is the difference between the system pressure and the vapour partial pressure at saturation conditions.

To account for forced convection heat transfer, the Dittus-Boelter correlation is included:

$$h_{fc} = 0.023\, R\mathbf{E_l}^{0.8} Pr_l^{0.4} \frac{k_l}{d_{in}} \tag{2.22}$$

These two HTCs are weighted with correction factors, the first of which is the enhancement factor, F, expressed as:

$$F = 1 + 2.4 \times 10^4 Bo^{1.16} + 0.87 \left(\frac{1}{X_{tt}}\right)^{0.32} \tag{2.23}$$

where:

- Bo is the boiling number; and
- X_{tt} is the Martinelli parameter.

The suppression factor, S, is defined as:

$$S = \frac{1}{1 + 2.53 \times 10^{-6} (R\mathbf{E_l} F^{1.25})^{1.14} + 1.75 N_{conf}^{0.3}} \tag{2.24}$$

where $N_{conf} = \sqrt{\frac{\sigma}{g(\rho_l - \rho_g)d^2}}$ is a confinement number, which corrects for the size of the internal channel.

Finally, the final equation can be written as:

$$h_{tp} = \sqrt{(F h_{fc})^2 + (S h_{pb})^2} \tag{2.25}$$

which is the two-phase HTC for saturated boiling, and:

$$h_{tp} = \sqrt{(F h_{fc})^2 + \left(S h_{pb} \frac{T_w - T_{sat}}{T_w - T_b}\right)^2} \tag{2.26}$$

is for subcooled boiling.

2.1.7.3.2 Liu-Winterton's Correlation

Liu and Winterton proposed a similar correlation to that of Chen et al., but with different correction factors and a different correlation for the nucleate boiling term [24]. Liu and Winterton's correlation is given by:

$$F = \left(1 + x Pr_l \left(\frac{\rho_l}{\rho_v} - 1\right)\right)^{0.35} \tag{2.27}$$

$$S = \frac{1}{1 + 0.055F^{0.1}R\mathbf{E_l}^{0.16}} \tag{2.28}$$

$$h_{pb} = 55\left(\frac{p}{p_{cr}}\right)^{0.12}\left[-\log_{10}\left(\frac{p}{p_{cr}}\right)\right]^{-0.55}M^{-0.5}q^{0.67} \tag{2.29}$$

where:

- p_{cr} is the fluid's critical pressure;
- p is the fluid's static pressure;
- M is the molar mass of the compound; and
- q is the heat flux.

It should be noted that this correlation does not include any channel size correction factor.

2.1.7.3.3 Kandlikar's Correlation

Finally, Kandlikar presented a correlation which utilizes the convection number, Co, defined as [25]:

$$Co = \left(\frac{1-x}{x}\right)^{0.8}\left(\frac{\rho_v}{\rho_l}\right)^{0.5} \tag{2.30}$$

which, similar to the Martinelli parameter (see Section 2.1.6.5), corrects for the different properties of the liquid and vapour phases as the vapour quality increases [11].

The final equation is then written as:

$$h_{tp} = h_{fc}\left(C_1 Co^{C_2}(25Fr)^{C_5} + C_3 Bo^{C_4}F_{fl}\right) \tag{2.31}$$

where:

- $C_1 = 0.6683$, $C_2 = -0.2$, $C_3 = 1058$, $C_4 = 0.7$, $C_5 = 0.3$ are constants, valid in the nucleate boiling region;
- F_{fl} is a fluid-dependent parameter equal to 3.3 for R32 flowing on copper and brass surfaces [26].

2.2 Computational Fluid Dynamics

The conventional approach in engineering heavily relies on empirical or semi-empirical models [27]. Such models typically perform very well for well-known processes or equipment but are less sufficient for predicting flow behaviour under new conditions or for novel designs. Traditionally, the development of new industrial equipment or upscaling from laboratory level to full industrial-scale is dependent on the expertise of experienced engineers. This development process is very time-consuming and often requires significant resources.

Computational Fluid Dynamics (CFD) allows for very accurate prediction and analysis of the flow behaviour and performance of new equipment designs and

processes. The geometry of the equipment is recreated using CAD software and the domain is partitioned into finite volume elements, forming a grid. In these finite volume elements, or cells, a set of conservation equations are solved numerically in an iterative manner.

These equations contain field variables describing the physical state of each cell in the geometry, resulting in local information about the fluid's behaviour, which can reveal particularly sensitive areas, bottlenecks or operational limits in a proposed new design.

2.2.1 Governing Equations for Single-Phase Flows

The Navier-Stokes equations are a set of coupled partial differential equations (PDEs) which describe the motion of viscous fluids. Mathematically, they express the conservation of mass, momentum, and energy. The equations are expressed in tensor notation and are derived using a control volume formulation [28].

2.2.1.1 Conservation of Mass

The equation for conservation of mass (commonly referred to as the continuity equation) is given by Eq. 2.32:

$$\frac{\partial \rho}{\partial t} + \nabla \cdot (\rho \vec{u}) = 0 \tag{2.32}$$

The first term denotes the accumulation of mass over time, and the second term expresses the advection of mass through the control volume. For incompressible flows, the density variation can be neglected and so Eq. 32 can therefore be rewritten in the following way with this assumption in mind:

$$\nabla \cdot \vec{u} = 0 \tag{2.33}$$

In the cases analysed in this thesis, the velocities are expected to be substantially lower than the speed of sound (Ma < 0.3) and therefore the flow can be considered incompressible, and so Eq. 2.33 can be applied for the conservation of mass.

2.2.1.2 Conservation of Momentum

In a static reference frame, the conservation of momentum, commonly denoted as the momentum equation, can be written in the following way:

$$\frac{\partial (\rho \vec{u})}{\partial t} + \nabla \cdot (\rho \vec{u} \vec{u}) = -\nabla p + \nabla \cdot \bar{\bar{\tau}} + \rho \vec{g} + \vec{F} \tag{2.34}$$

where:

- p is the static pressure;
- $\vec{\tau}$ is the stress tensor; and
- $\rho \vec{g}$ and $\vec{F}$ are the gravitational body force and external body forces, respectively.

The first and second terms on the right-hand side form the so-called total stress tensor, while the third and fourth terms are the gravitational and external body forces, respectively. The stress tensor $\vec{\tau}$ is defined as

$$\bar{\bar{\tau}} = \mu \left[(\nabla \vec{u} + \nabla \vec{u}^T) - \frac{2}{3} \nabla \cdot \vec{u} I \right] \tag{2.35}$$

where:

- μ is the molecular viscosity;
- I is the unit tensor; and
- the second term on the right-hand side is the effect of volume dilation.

2.2.1.3 Conservation of Energy

The conservation of energy, often referred to as the energy equation, is expressed in a general form in Eq. 18:

$$\frac{\partial}{\partial t} \left(\rho \left(e + \frac{\vec{u}^2}{2} \right) \right) + \nabla \cdot \left(\rho \vec{u} \left(h + \frac{\vec{u}^2}{2} \right) \right) = \nabla \cdot (k_{eff} \nabla T - h_j \vec{J}_j + \bar{\bar{\tau}}_{eff} \cdot \vec{u}) \tag{2.36}$$

where:

- e is the internal energy;
- $\vec{u}$ is the velocity;
- h is the static enthalpy;
- k_{eff} is the effective conductivity ($k_{eff} = k + k_t$, where k_t is the turbulent thermal conductivity);
- $\vec{J}_j$ is the diffusive flux of species j;
- $\bar{\bar{\tau}}_{eff}$ is the effective stress tensor.

It is an energy balance that includes an accumulative term and an advective term on the left-hand side. The initial three terms on the right-hand side correspond to the energy transfer associated with conduction, species diffusion, and viscous dissipation.

2.2.2 Multiphase Modelling Frameworks

For certain applications, there is a need to investigate multiple phases and their interactions. This is particularly true for boiling, where complex phenomena such as phase change and bubble dynamics need to be addressed in the governing equations. Accounting for these phenomena is crucial for accurately predicting heat transfer coefficients, dry-out location, and overall system performance.

The main difference between single-phase and multiphase CFD is that the additional phase(s) need to be taken care of. This not only involves solving additional equations but also incorporating new terms that represent interfacial interactions, such as mass, momentum, and energy transfer.

There are numerous multiphase frameworks, each treating the phases and their interactions in different ways. To determine the most suitable framework for a

particular case, it is important to identify which type of flow regimes are expected within the domain of interest, as well as the desired level of accuracy and/or available computational resources [28].

Figure 2.9 and Table 2.1 show a comparison of the main categories of multiphase frameworks.

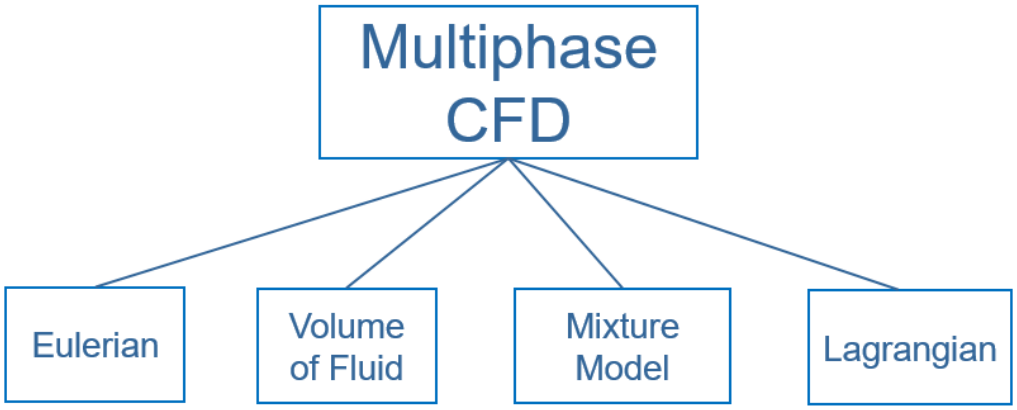

Figure 2.9: Schematic of different multiphase frameworks in CFD.

Table 2.1: Comparison of multiphase frameworks.

	Mixture	**Eulerian**	**Volume of Fluid**	**Lagrangian**
Concept	Single-fluid approach. Solves one set of eqs. for the mixture	Treats both phases as continuous fields. Solves one set of eqs. for each phase	Treats both phases as continuous fields. Resolves the interface between phases	Treats primary phase as continuous and dispersed phase as individual particles
Flow regimes	Bubbly, droplet, particle-laden flows	Bubbly, droplet, particle-laden flows	Bubbly, droplet, free surface flows	Bubbly, droplet, particle-laden flows
Accuracy	Low	High	Very high	High
Numerical Stability	High	Low	Medium	Medium
Comput. cost	Low	High	Very high	High
Outcome	Simplified modelling of multiphase flows	Mean fields of flow variables.	Interface and all scales resolved.	Behaviour of individual particles
Boiling models	Lee	Lee, TPC, RPI	Lee	-

2.2.2.1 Mixture model

The mixture model is a multiphase approach that solves a single set of governing equations for the mixture of phases, while also solving for their relative velocities as well as their volume fractions. It is less computationally expensive than a full multiphase framework, like the Eulerian-Eulerian, and can accurately predict flows where the dispersed phases are well distributed in the primary phase. However, in the case of flow boiling, the vapour phase is not expected to be well distributed throughout the liquid phase, hence this framework will not be considered in this thesis.

2.2.2.2 Lagrangian Particle Tracking

Lagrangian Particle Tracking is a multiphase framework where the primary phase is treated as an Eulerian field, while the dispersed phase is treated as individual particles (this is the reason why the framework is sometimes called Eulerian-Lagrangian). The equation of motion is solved for each particle and all forces acting on the particles are relative to its frame of reference. This is called the Lagrangian frame of reference, and any primary phase flow quantity can be completely different at the location of the particle compared to the mean field.

2.2.2.3 Eulerian-Eulerian

In contrast to the Eulerian-Lagrangian model described above, in the Eulerian-Eulerian model, an Eulerian reference frame is defined across the entire domain (i.e., the mesh) for both the primary and secondary phases. Hence, the behaviour of individual particles is of no concern, only averaged flow quantities are calculated.

2.2.2.4 Volume of Fluid

The Volume of Fluid (VoF) is a multiphase framework that employs an interface-capturing technique to resolve all the temporal and spatial scales at the interface of the two phases. This level of resolution requires a very refined grid and therefore a very small time-step size. The method is capable of modelling interfacial interactions with very high accuracy for small domains consisting only of a few bubbles. Despite being a powerful tool able to reproduce multiple mechanisms governing the motion, growth, coalescence, and collapse of individual bubbles, it is an impractical framework to use when macroscopic quantities of the domain are of primary concern.

2.2.2.5 Choice of Multiphase Modelling Frameworks for Analysis in This Thesis

For the purpose of evaluating boiling models for multiphase modelling in heat exchanger equipment, macroscopic properties of the flow behaviour were of primary interest. In addition, since in boiling flows, large degrees of separation in the physical nature of the continua occur between the primary and secondary phases (for example, the formation of tiny bubbles during nucleate boiling), high-resolution frameworks like the VoF framework were disregarded to save computational cost.

A continuum-based framework that solves the governing equations for both phases, which allows for the inclusion of advanced sub-models for interfacial interactions, would be less computationally demanding while still providing detailed representation of relevant boiling phenomena. Therefore, the Eulerian-Eulerian framework was determined to be the most suitable choice for this investigation.

2.2.3 Governing Equations for Multiphase Flows (Eulerian Framework)

In the Eulerian multiphase framework, each phase is treated as Eulerian fields, or in other words, are assumed to be continua [28]. This implies that averaging is required to obtain the mean fields for flow variables, such as density and velocity. The continuity, momentum, and energy equations are solved for each phase separately, as well as volume fraction equation(s). This implies that models are required to represent sub-continuum phenomena, such as nucleation of bubbles or particle interactions. Therefore, the choice of appropriate models becomes crucial.

Below, the governing equations in an Eulerian-Eulerian framework are presented for the liquid phase.

2.2.3.1 Conservation of Mass

In multiphase CFD, the continuity equation is solved for each phase.

$$\frac{\partial(\alpha_l \rho_l)}{\partial t} + \nabla \cdot (\alpha_l \rho_l \vec{u}_l) = \mathbf{S_l} \tag{2.37}$$

where:

- α_l is the volume fraction;
- ρ_l is the density of phase l;
- $\vec{u}_l$ is the velocity of phase l; and
- $\mathbf{S_l}$ is a mass transfer source term.

As can be seen, the main difference between the single- and multiphase continuity equations is the inclusion of the interfacial mass transfer terms on the right-hand side, $\mathbf{S_l}$, as well as the accumulative and advective term being weighted by the volume fraction, α_l. The source term for the liquid continuity equation can be expressed in the following way:

$$\mathbf{S_l} = \dot{m}_{vl} - \dot{m}_{lv} \tag{2.38}$$

where:

- $\dot{m}_{vl}$ denotes a condensation process (mass transfer from the gas to liquid phase), and
- $\dot{m}_{lv}$ denotes evapourative mass transfer (mass transfer from the liquid to gas phase).

Of importance then, is the understanding that both these terms need to be modelled, the details of which are discussed in Section 2.3.1.

2.2.3.2 Conservation of Momentum

$$\frac{\partial(\alpha_l \rho_l \vec{u}_l)}{\partial t} + \nabla \cdot (\alpha_l \rho_l \vec{u}_l \vec{u}_l) = -\nabla p + \nabla \cdot \bar{\bar{\tau}}_l + \alpha_l \rho_l \vec{g} + \sum \alpha_l \vec{F}_l + \mathbf{M_l} \tag{2.39}$$

where:

- p is the pressure (both phases share the same pressure);
- $\vec{g}$ is the gravitational acceleration; and
- $\bar{\bar{\tau}}_l$ is the stress-strain tensor, expressed as:

$$\bar{\bar{\tau}}_l = \alpha_l \mu_l (\nabla \vec{u}_l + \nabla \vec{u}_l^T) + \alpha_l \left(\lambda_l - \frac{2}{3}\mu_l\right) \nabla \cdot \vec{u}_l \vec{I} \tag{2.40}$$

where:

- μ_l is the shear viscosity;
- λ_l is the bulk viscosity; and
- $\vec{I}$ is the unit tensor.

$\mathbf{M_l}$ is the interfacial momentum transfer, expressed as:

$$\mathbf{M_l} = \vec{R}_{vl} + \dot{m}_{vl} \vec{u}_{vl} - \dot{m}_{lv} \vec{u}_{lv} \tag{2.41}$$

where $\vec{R}_{vl}$ is an interaction force between the phases, expressed as:

$$\vec{R}_{vl} = K_{vl}(\vec{u}_v - \vec{u}_l) \tag{2.42}$$

K_{vl} is an interfacial momentum exchange coefficient, expressed in the following way for fluid-fluid flows:

$$K_{vl} = \frac{\rho_v f}{6\tau_v} d_b A_{int} \tag{2.43}$$

where:

- d_b is the diameter of the vapour bubbles;
- A_{int} is the interfacial area;
- f is the drag function, defined in different ways for different exchange-coefficient models; and
- τ_v is the "particulate relaxation time", expressed as:

$$\tau_v = \frac{\rho_v d_v^2}{18\mu_l} \tag{2.44}$$

$\vec{F}_l$ is the sum of forces acting on the liquid phase. These forces will affect the vapour phase the most, hence, they are expressed in regards to the vapour phase below:

$$\vec{F}_v = \vec{F}_{E,v} + \vec{F}_{lift,v} + \vec{F}_{wl,v} + \vec{F}_{vm,v} + \vec{F}_{td,v} \tag{2.45}$$

where:

- $\vec{F}_{E,k}$ is an external body force;
- $\vec{F}_{lift,k}$ is a lift force;
- $\vec{F}_{wl,k}$ is a wall lubrication force;
- $\vec{F}_{vm,k}$ is a virtual mass force; and
- $\vec{F}_{td,k}$ is a turbulent dispersion force.

Closure for these force terms is required, and the choice of closure model will affect the behaviour of the flow in significant ways.

2.2.3.3 Conservation of Energy

The Eulerian formulation of the energy equation for multiphase flows is a modification of the corresponding single-phase equation.

$$\begin{aligned}\frac{\partial}{\partial t}\left(\alpha_k\rho_k\left(e_k+\frac{\vec{u}_k^2}{2}\right)\right)+\nabla\left(\alpha_k\rho_k\vec{u}_k\left(h+\frac{\vec{u}_k^2}{2}\right)\right)= \\ =\nabla*\left(\alpha_k k_{eff,k}\nabla T_k-h_k\vec{J}_k+\bar{\tau}_{eff,k}*\vec{u}_k\right)+p\frac{\partial\alpha_k}{\partial t}+\mathbf{E_l}\end{aligned} \tag{2.46}$$

The modifications include the multiplication of volume fraction of the phase to the accumulative, advective and conductive terms, as well as the inclusion of an interfacial energy transfer term and a pressure work term.

The source term can be expressed as:

$$\mathbf{E_l}=Q_{in}+Q_{vl}+\dot{m}_{vl}h_v(T_{sat})-\dot{m}_{lv}h_l(T_{sat}) \tag{2.47}$$

where:

- Q_{in} is the thermal energy put into the system;
- Q_{vl} is the heat transferred through the interface, calculated by the interfacial heat transfer model; and
- $\dot{m}_{vl}h_v(T_{sat})$ and $\dot{m}_{lv}h_l(T_{sat})$ are the thermal energies of the incoming and outgoing mass possess.

2.2.4 Turbulence Modelling

Turbulence is a complex and chaotic phenomenon that occurs at high Reynolds numbers, and it is computationally expensive[3] to resolve all the temporal and spatial scales of turbulent structures. As an alternative approach, so-called Reynolds-Averaged Navier-Stokes (RANS) modelling is a widely used approach that provides a computationally cheaper alternative for simulating turbulent flows.

2.2.4.1 RANS Modelling

In RANS modelling, the solution variables in the instantaneous Navier-Stokes equations are divided into a mean (time- or ensemble-averaged) component and a fluctuating component. For the velocity vector, this decomposition results in the following expression:

$$u_i=\bar{u}_i+u_i' \tag{2.48}$$

where $\bar{u}_i$ denotes the mean velocity components and u_i' represents the fluctuating velocity components ($i=1,2,3$). This decomposition is done in the same way for scalar quantities such as pressure and energy.

[3] If not impossible, for practical engineering-sized problems

Substituting the flow variables with these expressions in the instantaneous continuity and momentum equations, and then performing ensemble averaging (and omitting the overbar on the mean velocity, $\bar{u}_i$) results in the equations:

$$\frac{\partial \rho}{\partial t} + \frac{\partial}{\partial x_i}(\rho u_i) = 0 \tag{2.49}$$

$$\begin{aligned}\frac{\partial}{\partial t}\left(\rho u_i\right) + \frac{\partial}{\partial t}\left(\rho u_i u_j\right) = &- \frac{\partial p}{\partial x_i} + \frac{\partial}{\partial x_i}\left[\mu\left(\frac{\partial u_i}{\partial x_j} + \frac{\partial u_j}{\partial x_i} - \frac{2}{3}\delta_{ij}\frac{\partial u_i}{\partial x_i}\right)\right] \\ &+ \frac{\partial}{\partial x_j}\left(-\rho\overline{u_i' u_j'}\right)\end{aligned} \tag{2.50}$$

The equations above are known as the Reynolds-Averaged Navier-Stokes (RANS) equations and are here expressed in Cartesian tensor form. As a result of the averaging process above, one consequence is the emergence of additional terms ($-\rho\overline{u_i' u_j'}$) known as the "Reynolds stresses" which represent the influence of turbulence structures on the averaged flow.

Like the mass and energy transfer terms in the multiphase continuity, momentum and energy equations, these so-called Reynolds stresses require modelling for the closure of Eq. 2.50.

2.2.4.1.1 The Boussinesq Hypothesis

In 1877, Joseph Valentin Boussinesq introduced a pioneering concept to turbulence modelling [29]. His proposal stemmed from his observation that the momentum transfer in turbulent flows is dominated by the mixing induced by the turbulent eddies present in turbulent flow. Based on this observation, Boussinesq hypothesized that the turbulent shear stress was linearly dependent on the mean rate of strain of the flow, similar to laminar flows, and that therefore the so-called Reynolds stresses could be modelled in a similar way [28]. In his hypothesis, Boussinesq proposed that the coefficient governing this proportionality between the mean flow strain rate and the turbulent stresses be called the turbulent (or the eddy viscosity), denoted as μ_t.

Boussinesq's approach offers a way of modelling turbulent structures at a relatively low computational cost. However, it assumes that the eddy viscosity is an isotropic scalar quantity, which is not necessarily true for all cases, such as in secondary or highly swirling flows. Nevertheless, turbulence models derived from the Boussinesq hypothesis have proven very effective in modelling most shear flows, including wall boundary layers, mixing layers, and similar phenomena.

Using the Boussinesq hypothesis in Eq. 2.50, the Reynolds stresses in the RANS equations can be related to the mean velocity gradients and the turbulent viscosity in the following way [30]:

$$-\rho\overline{u_i' u_j'} = \mu_t\left(\frac{\partial u_i}{\partial x_j} + \frac{\partial u_j}{\partial x_i}\right) - \frac{2}{3}(\rho k + \mu_t\frac{\partial u_k}{\partial x_k})\delta_{ij} \tag{2.51}$$

where:

- μ_t is the turbulent viscosity;
- k is the turbulent kinetic energy; and
- δ_{ij} is the Dirac delta function.

2.2.4.2 Standard k-ε Model

The standard k-ε model is a two-equation turbulence model that introduces two transport equations for the turbulent kinetic energy, k:

$$\frac{\partial}{\partial t}(\rho k) + \frac{\partial}{\partial x_i}(\rho k u_i) = \frac{\partial}{\partial x_j}\left[(\mu + \frac{\mu_t}{\sigma_k})\frac{\partial k}{\partial x_j}\right] + G_k + G_b - \rho\varepsilon \tag{2.52}$$

and the turbulent dissipation rate, ε:

$$\frac{\partial}{\partial t}(\rho \varepsilon) + \frac{\partial}{\partial x_i}(\rho \varepsilon u_i) = \frac{\partial}{\partial x_j}\left[(\mu + \frac{\mu_t}{\sigma_\varepsilon})\frac{\partial \varepsilon}{\partial x_j}\right] + C_{1\varepsilon}\frac{\varepsilon}{k}(G_k + C_{3\varepsilon}G_b) - C_{2\varepsilon}\rho\frac{\varepsilon^2}{k} \tag{2.53}$$

where:

- G_k, G_b are the generation of k as a result of the mean velocity gradients and buoyancy, respectively;
- $\sigma_k, \sigma_\varepsilon$ are the turbulent Prandtl numbers for k and ε, respectively; and
- $C_{1\varepsilon}, C_{2\varepsilon}, C_{3\varepsilon}$ are empirical constants derived from experiments for fully turbulent flows.

The turbulent viscosity is calculated from k and ε in the following way:

$$\mu_t = \rho C_\mu \frac{k^2}{\varepsilon} \tag{2.54}$$

where C_μ is a constant. The standard k-ε model is based on the following assumptions:

- The flow in the domain is fully turbulent;
- Molecular viscosity effects are negligible; and
- The turbulent viscosity, μ_t, is an isotropic scalar (from the Boussinesq approximation).

These assumptions are valid for many turbulent flows, including wall boundary layers and mixing layers [28], and are therefore expected to be justifiable for the cases examined in this thesis. Further, while the k-ε model has been shown to predict turbulence in the free stream (high Re) region reasonably well, as a result of deficiencies in the modelling of ε, the model has also been shown to fail to capture the physics of various flows near the wall. Finally, as a result of difficulties in the accurate modelling of the flow near the wall, so-called wall functions are often used in conjunction with the standard k-ε model in the near-wall regions (see Section 2.2.4.4.1).

2.2.4.3 Standard k-ω Model

The standard k-ω model, proposed by Wilcox in 1988 [31], is a two-equation turbulence model that includes transport equations for the turbulent kinetic energy, k, and the specific dissipation rate, ω, which is approximately the ratio of k and ε:

$$\omega \approx \frac{\varepsilon}{k} \tag{2.55}$$

The k equation is defined as:

$$\frac{\partial}{\partial t}(\rho k) + \frac{\partial}{\partial x_i}(\rho k u_i) = \frac{\partial}{\partial x_j}\left[(\mu + \frac{\mu_t}{\sigma_k})\frac{\partial k}{\partial x_j}\right] + G_k + G_b - Y_k \tag{2.56}$$

and the ω equation as:

$$\frac{\partial}{\partial t}(\rho \omega) + \frac{\partial}{\partial x_i}(\rho \omega u_i) = \frac{\partial}{\partial x_j}\left[(\mu + \frac{\mu_t}{\sigma_\omega})\frac{\partial \omega}{\partial x_j}\right] + G_\omega + G_{\omega b} - Y_\omega \tag{2.57}$$

where:

- $G_\omega, G_{\omega b}$ describe the generation of ω due to mean velocity gradients and buoyancy effects.

Unlike the k-ε model, the k-ω model has been shown to predict the flow behaviour in the near-wall region with significantly greater accuracy. However, in addition to this, the standard k-ω model was also shown to have significant freestream sensitivity, meaning that it was sensitive to free stream conditions (outside of the boundary layer) which can greatly impact the solution, particularly in free shear flows[4] which are common for boiling flows [32].

As a result, Menter proposed a blended model comprising both the k-ε and k-ω models (the so-called k-ω Shear Stress Transport model) which has proved to be significantly more reliable for a wider range of flows, both in the near-wall as well as freestream regions.

2.2.4.4 k-ω Shear Stress Transport (SST) Model

As indicated, the k-ω Shear Stress Transport (SST) model is a combination of the standard k-ε and k-ω models [32]. Briefly, in the SST model, the k-ε model is rewritten into a k-ω formulation, after which the two models were combined with a blending function and added together. The blending function then activates the k-ω model in the near-wall region, and the k-ε model in the free stream with the result being that the blended (SST) model then takes advantage of the strengths of both turbulence models: good prediction of flow behaviour in the near-wall region by the k-ω model, and the free stream independence of the k-ε model.

[4] Free shear flows refer to when two fluids stream adjacent to one another with different velocities, without any solid barriers in between [33]

2.2.4.5 Wall Functions and y^+

As a result of the non-slip condition at wall boundaries (which assumes zero velocity at the wall), the freestream velocity decreases steeply due to the friction between the flow and the wall, resulting in the formation of the well-known (momentum) boundary layer [28], [34].

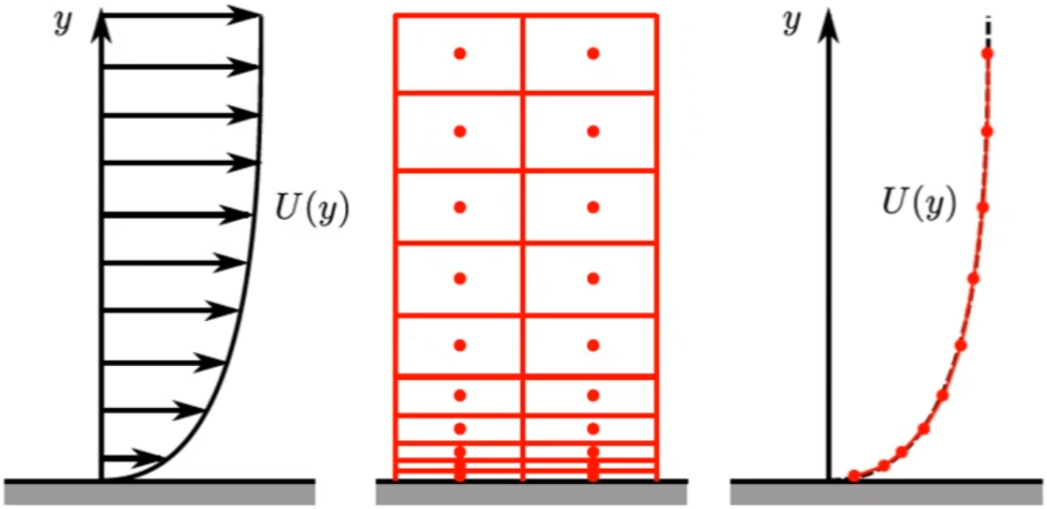

Figure 2.10: Schematic of a velocity profile (left), computational mesh required to resolve the steep gradient of flow variables (centre) and computed boundary layer profile (right) [34].

A second-order finite volume CFD code applies a piecewise-linear approach in resolving the near-wall region. Consequently, to resolve the steep gradient in flow quantities near the wall, a highly refined mesh in the direction normal to the wall is required. Apart from increasing the number of overall number of cells in the computational domain, and therefore overall simulation time, this refinement also leads to high aspect ratios and (potentially) poor cell quality adjacent to the walls, making convergence of the simulations longer and potentially more difficult.

As a result of the above, an alternative approach is the so-called "wall function" approach, in which the wall adjacent cells are replaced by a single large cell in which the flow behaviour is modelled using a non-linear flow function.

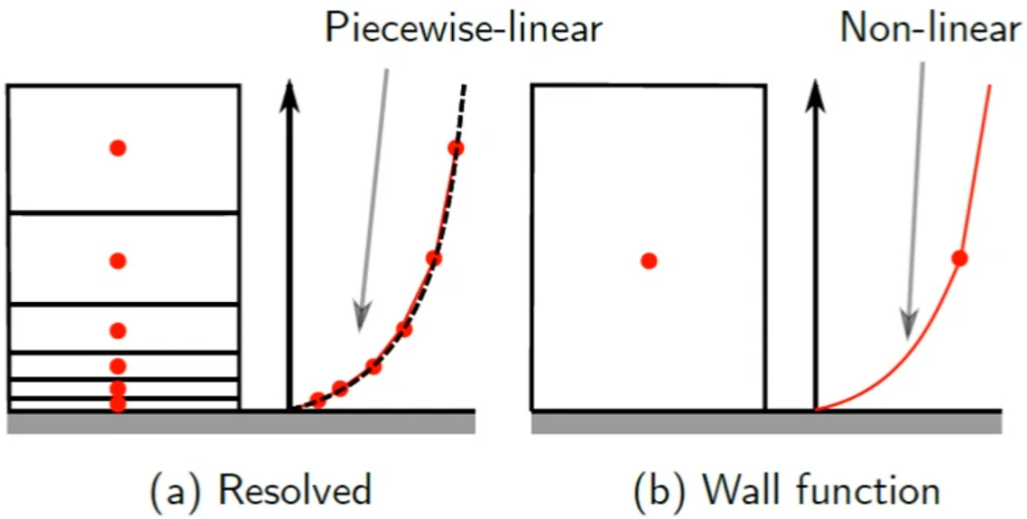

Figure 2.11: Comparison of a piecewise-linear and a non-linear (wall function) approach [34].

In order to create a non-linear function that would accurately model the variation near the wall, data of velocity and distance from the wall were extracted from numerous experiments and Direct Numerical Simulations (DNS) of planar, parallel flows without separation, curvature, or strong pressure gradients (see Fig. 2.11). This data was converted into dimensionless quantities to make these functions applicable for a wide range of geometries and flows:

- Dimensionless velocity: $U^+ = \frac{U}{U_\tau}$; and
- Dimensionless distance from the wall: $y^+ = \frac{yU_\tau}{\nu}$;

where:

- $U_\tau = \sqrt{\frac{\tau_w}{\rho}}$ is the friction velocity;
- τ_w is the wall shear stress; and
- ρ is the fluid density.

The aim is to fit functions against this observed behaviour (black line). Depending on y^+, the near-wall region is divided into the viscous sub-layer, buffer layer, and log-law region.

The viscous sub-layer ($y^+ < 5$) can be closely fitted with

$$U^+ = y^+ \tag{2.58}$$

while the log-law region ($30 < y^+ < 200$) can be modelled with the logarithmic law of the wall

$$U^+ = \frac{1}{\kappa} \ln(Ey^+) \tag{2.59}$$

where:

- κ is the von Kármán constant ($= 0.4187$); and
- E is an empirical constant ($= 9.793$).

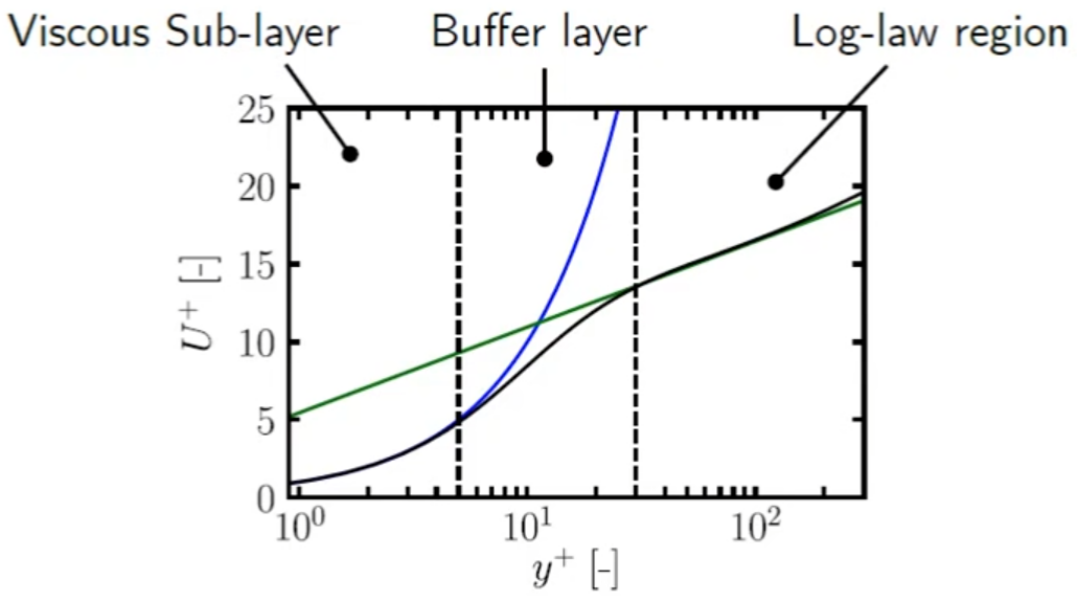

Figure 2.12: Diagram of dimensionless velocity and distance from the wall. Black line: Experimental and DNS data. Green line: log law. Blue line: $U^+ = y^+$ [34].

It can be observed that neither the green nor the blue line fits the empirical data in the buffer layer, which is why CFD code manuals generally recommend not having first layer cells in the buffer layer. CFD codes have incorporated features to blend or switch between Eqs. 2.58 and 2.59, but this approach generally gives inaccurate results. Therefore, the most common meshing strategy is to either generate a resolved mesh for flows with $y^+ < 1$, or a wall-function mesh for flows with $30 < y^+ < 300$.

As mentioned above, Fig. 8 consists of data from planar, parallel flows without separation, curvature, or strong pressure gradients. This means the universal profile cannot be expected to give accurate results in flows where these effects are present. To avoid these inaccuracies, trial-and-error in industry has shown that having a $y^+ \approx 1$ (that is, resolving, and not modelling the near wall flow) will in general produce better results (since the variation between the wall and the wall-adjacent cells will be linear). This is significant because, in finite-volume second-order CFD codes, the variation between the cells is linear.

In this investigation, both methods of near-wall modelling were used, with $y^+ < 1$ near-wall modelling used in conjunction with the k-ω SST model, and a combination of wall-function and near-wall modelling (via the so-called "enhanced wall treatment" approach) when using the k-ε model. In this latter approach, in regions where the computational mesh is sufficiently fine, the CFD solver employs the near-wall resolution approach, and in regions where the mesh is coarser, the solver reverts to a wall function approach [28].

2.3 Boiling modelling

As indicated previously, in multiphase simulations, the flow equations are characterized by mass, momentum and energy transfer source terms, the modelling of which are central to the overall accuracy of the simulated systems.

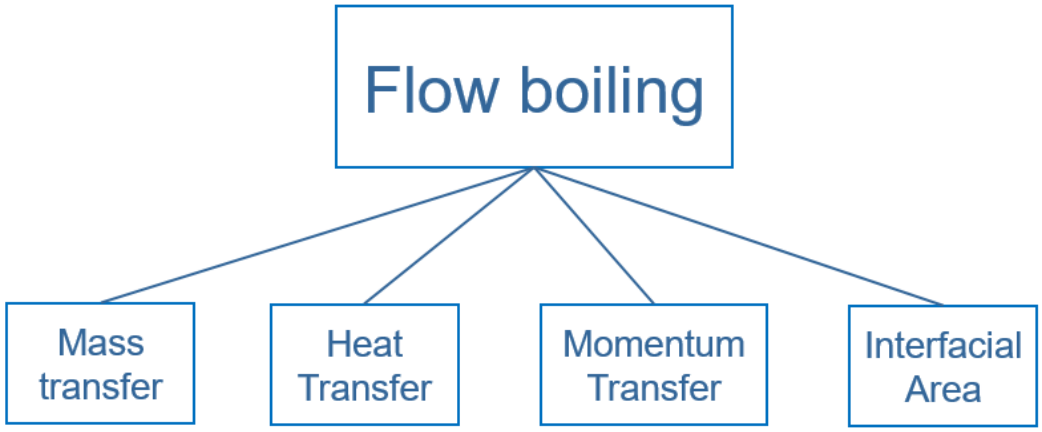

Figure 2.13: Flow chart of the physical processes that require modelling in flow boiling.

2.3.1 Mass Transfer Modelling

The most important aspects of numerical modelling of flow boiling are to properly account for the mass and heat transfer between the phases, and in doing so accurately model the boiling phenomena (liquid-gas mass transfer). Mass transfer, in particular, poses challenges not only due to its inherent complexity but also because it introduces numerical instabilities.

The goal of some boiling models is to model these complex processes while maintaining numerical stability, unavoidably reducing their physical accuracy. On the contrary, other models have been developed to incorporate more complexity, at the cost of increased computational power and poorer convergence behaviour.

The complete set of available boiling models in Fluent 2023 R1, in the VOF and Eulerian-Eulerian frameworks, are presented in Fig. 2.14.

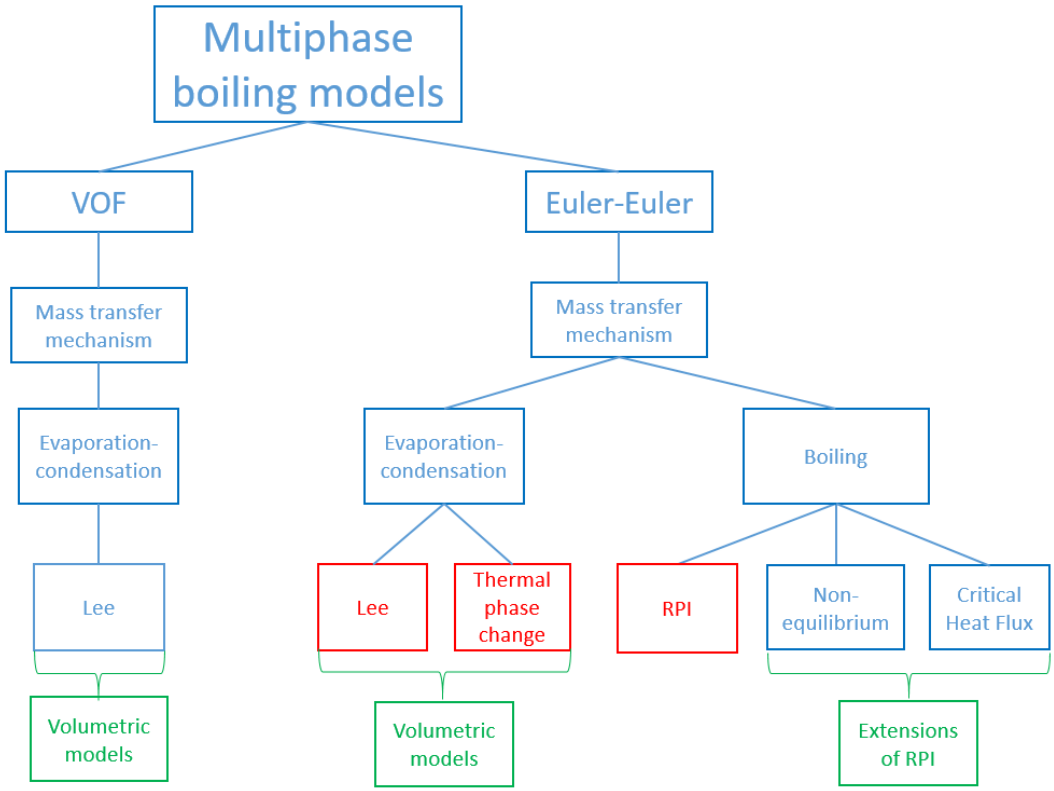

Figure 2.14: Flow chart of the available boiling/ Evaporation models in ANSYS Fluent 2023R1 [28].

As indicated previously, the Volume of Fluid method was not investigated in this thesis, since it is an interface capturing technique which would require a very refined grid to resolve the nucleation of bubbles and which was not practical given the aim of this work was to capture the macroscopic heat transfer characteristics of a full sized heat exchanger tube.

Additionally, phenomena related to cavitation was irrelevant for this investigation, hence, a smaller flow chart including the relevant boiling models available within the Eulerian-Eulerian framework is presented in Fig. 2.15.

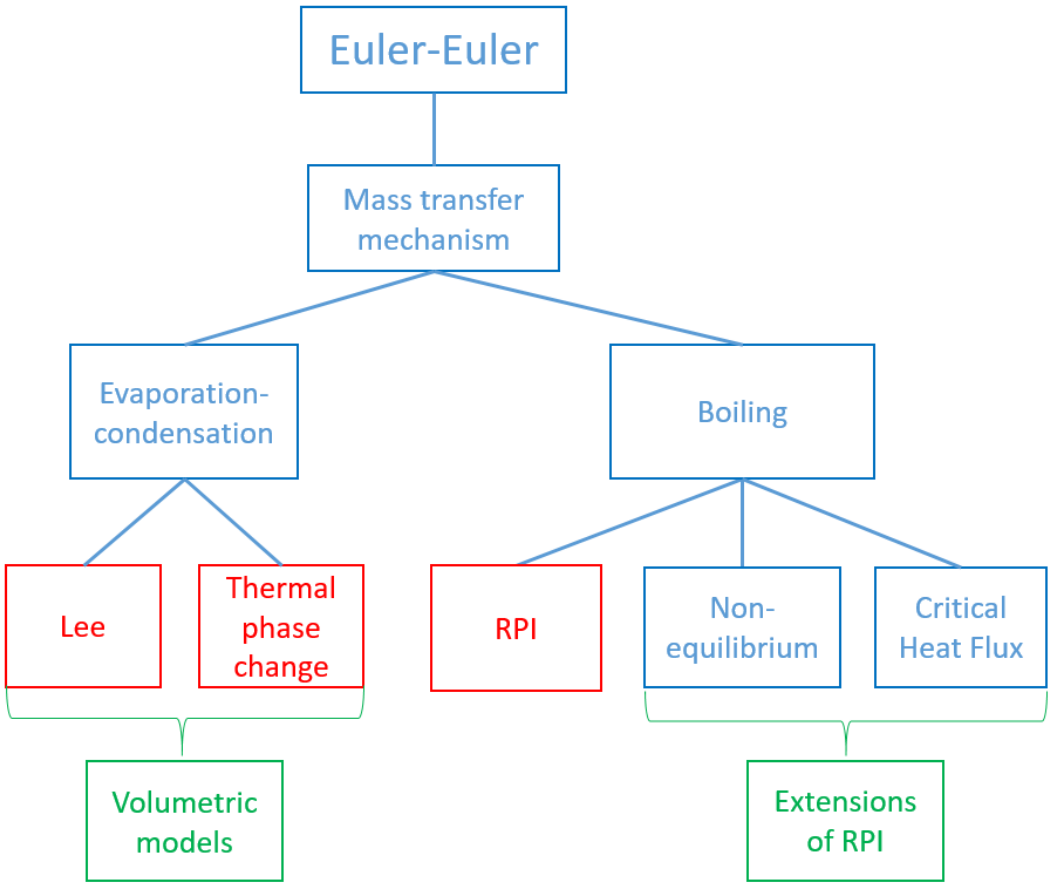

Figure 2.15: Flow chart of the available boiling/ evaporation models compatible with the Eulerian framework in ANSYS Fluent 2023R1 [28].

This leaves the selection of the Lee, the Thermal Phase Change (TPC), and the RPI models (including its extensions for transitional and film boiling, applicable for post-CHF conditions), of which the Lee and TPC models were the eventual focus of this thesis.

2.3.1.1 Lee Model

The Lee model is a simple, physically based mechanistic sub-model which can be applied in the VOF, the mixture, or the Eulerian-Eulerian multiphase frameworks, when Evaporation/condensation is chosen as the interfacial mass transfer mechanism.

The simplicity of the model stems from rough assumptions made about the evaporation processes:

- Assumes the evaporation takes place on a flat interface, in order to derive the model expression from the Hertz Knudsen formula;
- Assumes the bubbles are well dispersed;
- Assumes all the bubbles have the same, constant diameter;
- Disregards any microscopic phenomena associated with boiling.

The liquid-vapour mass transfer is governed by the vapour transport equation, and vice versa by the liquid transport equation (continuity eqs. for each phase).

Only the vapour transport equation is presented for brevity:

$$\frac{\partial \alpha_v \rho_v}{\partial t} + \nabla(\alpha_v \rho_v \vec{u}_v) = \dot{m}_{lv} - \dot{m}_{vl} \tag{2.60}$$

where:

- Index v denotes the vapour phase; and
- $\dot{m}_{lv}$, $\dot{m}_{vl}$ represent the rates of mass transfer due to Evaporation and condensation, respectively [kg/s/m^3].

As the walls heat up liquid in the near-wall region in a single-phase CFD setup, that liquid will eventually get superheated ($T_l > T_{\text{sat}}$). Instead, this model converts all of the superheated liquid into vapour, governed by the following equation:

$$\dot{m}_{lv} = C_{lv} \alpha_l \rho_l \left(\frac{T_l - T_{\text{sat}}}{T_{\text{sat}}} \right) \tag{2.61}$$

In some regions of the domain, vapour bubbles will transfer heat to the surrounding liquid and become subcooled ($T_v < T_{\text{sat}}$), eventually condensing back to liquid:

$$\dot{m}_{vl} = C_{vl} \alpha_v \rho_v \left(\frac{T_{\text{sat}} - T_v}{T_{\text{sat}}} \right) \tag{2.62}$$

The coefficient can be interpreted as the relaxation time for a liquid-fluid system to reach equilibrium in terms of mass transfer, and must be fine-tuned for each specific problem description. The source term for the energy equation is obtained by multiplying the latent heat with the rate of mass transfer.

The Hertz-Knudsen formula provides the interfacial mass flux from evaporation-condensation, based on the kinetic theory for a flat interface:

$$F = \beta \sqrt{\frac{M}{2\pi R T_{\text{sat}}}} (p^* - p_{\text{sat}}) \tag{2.63}$$

where:

- F is the interfacial mass flux [kg/s/m^2];
- M is the molar mass [kg/mol];
- R is the universal gas constant [J/(mol*K)];
- p^* is the vapour partial pressure at the interface in the vapour region; and
- T_{sat} and p_{sat} are the saturation temperature and pressure.

β is the accommodation coefficient that accounts for the portion of vapour molecules absorbed by liquid interface, and equals 1 at equilibrium conditions.
Derived from the equations for liquid and vapour chemical potential, the Clapeyron-Clausius equation associates the saturation pressure and temperature:

$$\frac{dp}{dT} = \frac{h_{\text{lat}}}{T(v_v - v_l)} \tag{2.64}$$

where:

- h_{lat} is the latent heat; and
- v_v, v_l are the specific volumes for the vapour and liquid phase.

Assuming that the pressure and temperature are approximately at saturation conditions, the Clapeyron-Clausius equation can be written as:

$$(p^* - p_{\text{sat}}) = -\frac{h_{\text{lat}}}{T(v_v - v_l)}(T^* - T_{\text{sat}}) \tag{2.65}$$

Combining this expression with the Hertz Knudsen equation gives:

$$F = \beta\sqrt{\frac{M}{2\pi R T_{\text{sat}}}}h_{\text{lat}}\left(\frac{\rho_v\rho_l}{\rho_l - \rho_v}\right)\left(\frac{T^* - T_{\text{sat}}}{T_{\text{sat}}}\right) \tag{2.66}$$

In the Eulerian framework, the secondary phase (in this case the vapour phase) is assumed to be dispersed in the primary phase. Using the Particle Model (discussed in Section 2.2.7.2), assuming all vapour bubbles have the same diameter, the interfacial area density is then given as:

$$A_i = \frac{6\alpha_v\alpha_l}{d_b} \tag{2.67}$$

where d_b is the bubble diameter [m]. The phase source term, $\dot{m}_{lv}$ [kg/(m^3 s)] can then be expressed as:

$$FA_i = \frac{6}{d_b}\beta\sqrt{\frac{M}{2\pi R T_{\text{sat}}}}h_{\text{lat}}\left(\frac{\alpha_v\rho_l}{\rho_l - \rho_v}\right)\left[\alpha_l\rho_l\left(\frac{T^* - T_{\text{sat}}}{T_{\text{sat}}}\right)\right] \tag{2.68}$$

Using Eq. 2.61, C_{vl} can then be expressed as:

$$C_{lv} = \frac{6}{d_b}\beta\sqrt{\frac{M}{2\pi R T_{\text{sat}}}}L\left(\frac{\alpha_v\rho_l}{\rho_l - \rho_v}\right) \tag{2.69}$$

which finally gives the full expression describing the evaporation process, C_{vl} being the inverse of relaxation time [s^{-1}].

The necessity for fine-tuning the coefficient to match experimental data arises from the fact that both the bubble diameter and and the accommodation coefficient are rarely accurately known. As default, the coefficients for evaporation and condensation are set to 0.1.

2.3.1.2 Thermal Phase Change Model

Similar to the Lee model, the Thermal Phase Change (TPC) model is a sub-model for mass transfer available when evaporation/condensation is the chosen mass transfer mechanism, and can only be applied within the Eulerian-Eulerian framework. Both the Lee and TPC models are referred to as volumetric models because they convert any volume of liquid to vapour when the temperature exceeds the fluid's saturation temperature, and vice versa. Unlike the RPI model, the volumetric models do not include any sub-grid modeling [28], [35].

The heat transfer equation from the liquid side of the interface is expressed as

$$Q_l = C_l h_l A_i (T_s - T_l) - \dot{m}_{lv} H_{ls} \tag{2.70}$$

While it is expressed from the vapour side as

$$Q_v = C_v h_v A_i (T_s - T_v) + \dot{m}_{lv} H_{vs} \tag{2.71}$$

where:

- $Q_{l,v}$ are the thermal energies entering the liquid or vapour phase [W];
- $C_{l,v}$ are the scaling factors;
- A_i is the area of the interface $[m^2]$;
- $h_{l,v}$ are the phase HTCs $[\frac{W}{m^2 K}]$;
- $T_{l,v}$ are the phase bulk temperatures $[K]$; and
- $H_{ls,vs}$ are the phase static enthalpies $[\frac{J}{kg}]$.

$C_{(l,v)}$ are by default set to 1.0. Assuming that surface tension has no effect on pressure, the interfacial temperature is set as the saturation temperature, $T_s = T_{\text{sat}}$.

The overall heat balance must be satisfied as neither the mass nor heat can be stored in the phase interface.

$$Q_l + Q_v = 0 \tag{2.72}$$

By inserting Eqs. 2.70 and 2.71 into Eq. 2.72, the mass transfer from the liquid to the vapour phase due to evaporation can be expressed as

$$\dot{m}_{lv} = -\frac{C_l h_l A_i (T_{\text{sat}} - T_l) + C_v h_v A_i (T_{\text{sat}} - T_v)}{H_{vs} - H_{ls}} \tag{2.73}$$

Careful calculation of the phase enthalpies is required, given the discontinuity in static enthalpy at the interface due to the latent heat between the two phases, along with the heat transfer for either phase to the interface. The Prakash formulation can be used to express the liquid and vapour static enthalpies in the case of evaporation. The liquid phase enthalpy will be the bulk enthalpy since it is the outgoing phase,

$$H_{ls} = H_l(T_l) \tag{2.74}$$

And the vapour phase enthalpy will be the saturation enthalpy since it is the incoming phase

$$H_{vs} = H_v(T_{\text{sat}}) \tag{2.75}$$

This ensures that the formulation of Eq. 2.73 is both physical and numerically stable, since the denominator will be non-zero (greater or equal to the latent heat).

Further, since the mass transfer process in the TPC model is completely governed by the interphase heat transfer and overall heat balance, there should be no need to fine-tune the mass transfer coefficients as in the Lee model [28].

The resulting source terms for the governing equations for the two models can be seen in Table 2.2.

Table 2.2: Comparison of the source terms for the Lee and Thermal Phase Change models.

	Lee model	**TPC model**
Continuity	$\mathbf{S_l} = \dot{m}_{vl} - \dot{m}_{lv}$ $\dot{m}_{lv} = C_l v \alpha_l \rho_l \frac{(T_l - T_{\text{sat}})}{T_{\text{sat}}}$	$\mathbf{S_l} = \dot{m}_{vl} - \dot{m}_{lv}$ $\dot{m}_{lv} = -\frac{(C_l h_l A_i (T_{\text{sat}} - T_l) + C_v h_v A_i (T_{\text{sat}} - T_v))}{(H_{vs} - H_{ls})}$
Momentum	$\mathbf{M_l} = \vec{R}_{vl} + \dot{m}_{vl}\vec{u}_{vl} - \dot{m}_{lv}\vec{u}_{lv}$	$\mathbf{M_l} = \vec{R}_{vl} + \dot{m}_{vl}\vec{u}_{vl} - \dot{m}_{lv}\vec{u}_{lv}$
Energy	$\mathbf{E_l} = Q_{vl} + \dot{m}_{vl} h_{v,sat} - \dot{m}_{lv} h_{l,sat}$	$\mathbf{E_l} = Q_{vl} + \dot{m}_{vl} h_{v,sat} - \dot{m}_{lv} h_{l,sat}$

2.3.2 Interfacial heat transfer modelling

The interfacial energy transfer rate is generally assumed to be dependent on the temperature difference and the interfacial area, expressed as:

$$Q_{lv} = h_{lv} A_i (T_s - T_v) + \dot{m}_{lv} H_{vs} \tag{2.76}$$

$$Q_{vl} = h_{vl} A_i (T_s - T_l) - \dot{m}_{lv} H_{ls} \tag{2.77}$$

where:

- Q_{lv}, Q_{vl} are the heat transfer rates from the liquid to the vapour phase and vice versa;
- h_{lv}, h_{vl} are the phase specific heat transfer coefficients;
- T_s is the temperature at the interface (saturation temperature);
- T_l, T_v are the bulk temperatures of the phases;
- $\dot{m}_{lv}$ is the mass transfer rate from the liquid to the vapour phase; and
- H_{ls}, H_{vs} are the phase enthalpies at the interface.

The heat transfer coefficients can be set to constant values, or modelled in with different approaches depending on the chosen boiling model.

In order to achieve a comprehensive representation of flow boiling, it is crucial to utilize a heat transfer model that is capable of accurately modelling the interfacial heat transfer occurring between the phases. Due to the formulation of the boiling models, different heat transfer models are compatible with them. The available models are presented below (see Fig. 2.16).

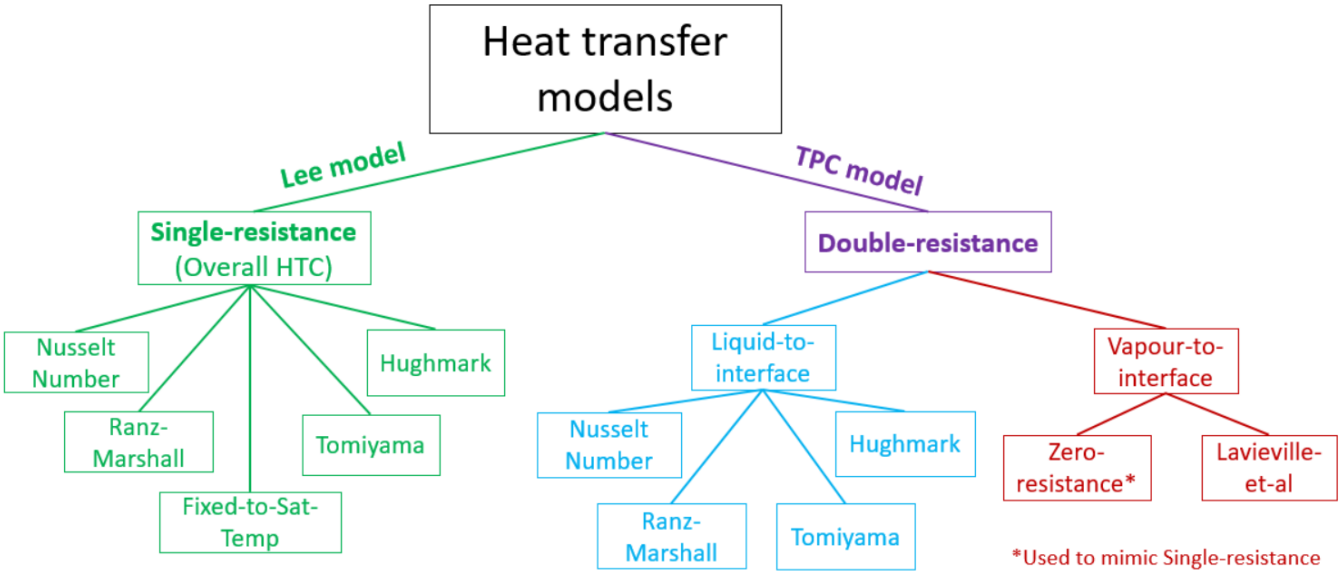

Figure 2.16: Heat transfer sub-models available for the Lee and TPC boiling models.

2.3.2.1 Single-resistance approach

The single-resistance approach assumes that the interfacial heat transfer is governed by an overall heat transfer resistance for the whole process, and an overall heat transfer coefficient ($h_{lv} = h_{vl}$) is calculated. Below, different ways of calculating the overall HTC are presented, compatible with the Lee and RPI boiling models.

$$Q_l = -Q_v = h_{lv} A_i (T_v - T_l) \tag{2.78}$$

2.3.2.1.1 Nusselt number

By specifying the Nusselt number for the liquid phase, the HTC can be calculated as follows:

$$h_{lv} = \frac{k_v Nu_l}{d_b} \tag{2.79}$$

where k_v is the thermal conductivity of the vapour, and d_b is the bubble diameter.

2.3.2.1.2 Ranz-Marshall model

Using the correlation proposed by Ranz and Marshall [36], [37], the Nusselt number is calculated in the following way:

$$Nu_l = 2 + 0.6 Re_l^{1/2} Pr^{1/3} \tag{2.80}$$

where the Reynolds number, $Re_l = \frac{\rho_l |u_l - u_v| d_b}{\mu_l}$, is expressed the bubble diameter and the relative velocity between the phases, and the Prandtl number, $Pr = \frac{c_{p,v} \mu_v}{\mu_v}$, is based on the vapour phase.

2.3.2.1.3 Hughmark model

The Hughmark model is an extension of the Ranz-Marshall Model for a greater range of Re, valid for $0 \leq Pr \leq 250$.

$$Nu_l = \begin{cases} 2 + 0.6Re_l^{1/2}Pr^{1/3}, & 0 \leq Re_l < 776.06 \\ 2 + 0.27Re_l^{0.62}Pr^{1/3}, & 776.06 \leq Re_l \end{cases} \tag{2.81}$$

2.3.2.1.4 Tomiyama model

The Tomiyama model employs a slightly different correlation and is viable for turbulent bubbly flows with relatively low Re.

$$Nu_l = 2.0 + 0.15Re_l^{4/5}Pr^{1/2} \tag{2.82}$$

2.3.2.1.5 Fixed to Saturation Temperature

The Fixed to Saturation Temperature approach is based on two assumptions:

- All of the interfacial heat transfer goes into mass transfer; and
- The vapour is fixed to the saturation temperature for the given pressure.

These assumptions are then applied to Eqs. 2.76 and 2.77, resulting in the following conditions for evaporation:

$$\dot{m}_{lv} \geq 0: \quad T_v = T_s, \quad H_{vs} = H_{ls} = H_v(T_s) \tag{2.83}$$

2.3.2.2 Double-resistance approach

The Lee model relies on a single-resistance approach, where an overall interfacial HTC accounts for the process of transferring heat from the liquid to the vapour.

In contrast, the TPC Model uses a double-resistance approach where a separate HTC is calculated for each side of the interface. In multiphase flows, the liquid and vapour phases have very different properties and the interface is a discontinuity. They will therefore exhibit different amounts of resistance to incoming heat, and can be more accurately modelled if the heat transfer process on each side of the interface are modelled in different ways (see Fig. 2.17). The overall HTC for the double-resistance approach is defined as:

$$Q_{lv} = -Q_{vl} = h_{lv}A_i(T_s - T_v), \quad \frac{1}{h_{lv}} = \frac{1}{h_l} + \frac{1}{h_v} \tag{2.84}$$

where:

- h_l is the HTC for the liquid-to-interface heat transfer,
- h_v is the HTC for the interface-to-vapour heat transfer, and
- T_s is the interface temperature, assumed to be equal to the saturation temperature of the fluid, and set as the same for the liquid and vapour side.

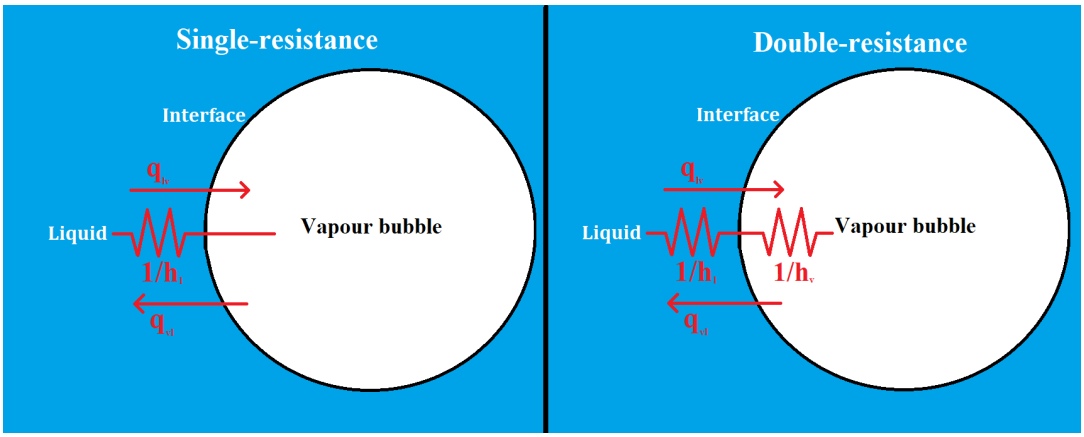

Figure 2.17: Schematic comparing single-resistance heat transfer (left) and double-resistance heat transfer (right).

Here, the previously discussed models can be applied to both phases, except for the Fixed to Saturation Temperature approach. Instead, one can employ the Constant Time Scale Method for the vapour side, a model formulated by Lavieville et al. [38].

2.3.2.2.1 Lavieville (Constant Time Scale) Method

Similar to the Fixed to Saturation Temperature approach, the vapour is assumed to maintain the saturation temperature for the given pressure:

$$Q_{lv} = \frac{(\alpha_v \rho_v c_{p,v})}{\delta t}(T_s - T_v) \tag{2.85}$$

where:

- α_v is the vapour volume fraction; and
- δt is the time scale, usually set to 0.05.

2.3.2.2.2 Zero-resistance criteria

Applying a zero-resistance criteria to the vapour side will force the vapour to have the same temperature as the interface (saturation temperature). This implies that the heat transfer coefficient will tend to infinity on this side of the interface.

2.3.3 Interfacial momentum transfer modelling

In a boiling flow with phase inversion, the vapour phase will begin as small bubbles nucleating at the walls, accumulating at the top of the tube. Eventually, as the vapour fraction increases, they will start coalescing, forming larger bubbles. At the end of the tube, the vapour phase start to occupy the majority of the domain, making it the primary phase.

At each stage of the vaporization, the phases will exchange momentum depending on the size and shape of the interfaces. This exchange is governed by interfacial forces, of which the most significant ones are listed below [39]:

- Drag force;
- Lift force;
- Wall lubrication force;
- Virtual mass force; and
- Turbulent dispersion force.

Fig. 2.18 shows a summary of the aforementioned forces.

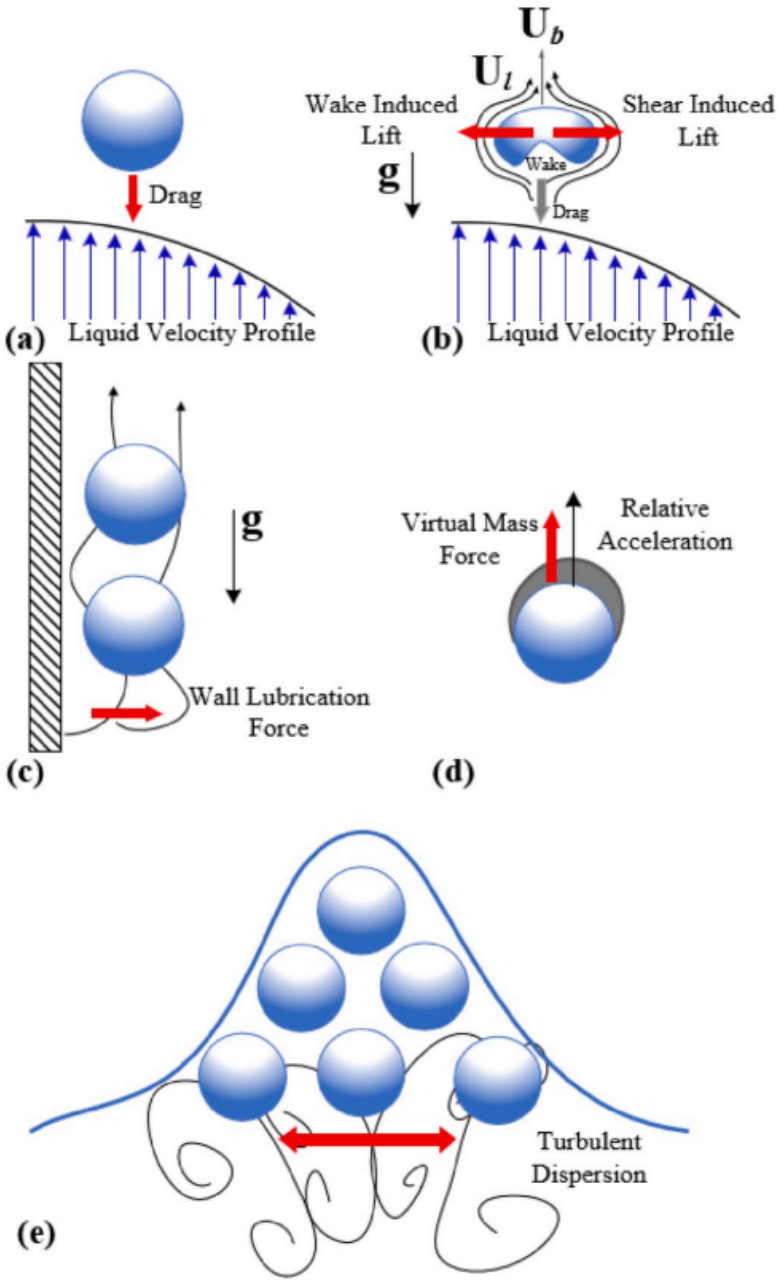

Figure 2.18: Schematic of the interfacial forces acting on bubbles. (a) drag force, (b) lift force, (c) wall lubrication force, (d) virtual mass force, and (e) turbulent dispersion force [40].

2.3.3.1 Drag force

The drag force acting on dispersed particles occurs because of the relative velocity differences between the dispersed and primary phase, in this case vapour bubbles and liquid. It can be likened to a frictional force acting in the opposite direction of the axial flow. For a spherical bubble, the drag force is expressed as:

$$\vec{F}_D = \frac{1}{8} C_D \rho_l A_i |\vec{u}_v - \vec{u}_l| (\vec{u}_v - \vec{u}_l) \tag{2.86}$$

where:

- C_D is the drag coefficient;
- A_i is the interfacial area; and
- $|\vec{u}_v - \vec{u}_l|$ is the relative velocity between the vapour bubble and the liquid.

In the momentum equation, the exchange coefficient, K_{vl}, (see Eq. 2.39) takes the drag force into account with the drag function, f:

$$K_{vl} = \frac{\rho_v f}{6\tau_v} d_v A_i \tag{2.87}$$

where τ_v is the response time, or "particulate relaxation time", of the vapour bubbles:

$$\tau_v = \frac{\rho_v d_v^2}{18\mu_l} \tag{2.88}$$

The drag function, f, generally includes C_D, which can be calculated using different models. Nearly all of them are based on the relative Reynolds number:

$$Re_{vl} = \frac{\rho_l |\vec{u}_v - \vec{u}_l| d_v}{\mu_l} \tag{2.89}$$

where d_v is the vapour bubble diameter.

2.3.3.1.1 Schiller and Naumann model

Schiller and Naumann proposed a drag coefficient correlation for general use in fluid-fluid flows [41]:

$$C_D = \begin{cases} \frac{24(1+0.15 Re_{vl}^{0.687})}{Re_{vl}}, & Re \leq 1000 \\ 0.44, & Re > 1000 \end{cases} \tag{2.90}$$

2.3.3.1.2 Symmetric model

The symmetric model is a modification of the Schiller and Naumann model. The coefficient is defined in the same way (see Eq. 2.90), but the viscosity and density are calculated from volume-averaged properties:

$$\mu_{vl} = \alpha_v \mu_v + \alpha_l \mu_l \tag{2.91}$$

$$\rho_{vl} = \alpha_v \rho_v + \alpha_l \rho_l \tag{2.92}$$

The diameter is determined as follows, allowing both phases to be dispersed:

$$d_{vl} = \frac{1}{2}(d_v + d_l) \tag{2.93}$$

If there is only one dispersed phase, then $d_l = d_v$. Eqs. 2.91, 2.92, and 2.93 are then used to calculate the relative Reynolds number:

$$Re_{vl} = \frac{\rho_{vl}|\vec{u}_v - \vec{u}_l|d_{vl}}{\mu_{vl}} \tag{2.94}$$

which is subsequently used to calculate the drag coefficient:

$$C_D = \begin{cases} \frac{24(1+0.15Re_{vl}^{0.687})}{Re_{vl}}, & Re \leq 1000 \\ 0.44, & Re > 1000 \end{cases} \tag{2.95}$$

This model is suitable for cases where the secondary phase is expected to be dispersed in one region of the domain and the continuous phase in another, such as in boiling flows with phase inversion. This is why this sub-model was used in this thesis.

2.3.3.2 Lift force

The lift force is a force that can greatly affect the radial trajectory of dispersed particles. In boiling flows, this force pushes the bubbles upwards relative to the liquid velocity.

Depending on the bubble size, their trajectory perpendicular to the rotation of the liquid velocity will also be affected by a transverse lift force [42]. Tomiyama et al. found that for single air bubbles in a glycerol-water solution, there was a critical bubble diameter that when exceeded, the bubbles would traverse towards the core of the fluid. For smaller bubbles below this threshold, they would move towards the walls.

A combination of these two lift forces can be expressed as:

$$\vec{F}_L = -C_L \alpha_v \rho_l |\vec{u}_v - \vec{u}_l| \times (\nabla \times \vec{u}_l) \tag{2.96}$$

where:

- C_L is the lift coefficient;
- $|\vec{u}_v - \vec{u}_l|$ is the relative velocity between the phases; and
- $(\nabla \times \vec{u}_l)$ is the rotation of the liquid velocity.

2.3.3.2.1 Tomiyama model

The Tomiyama model is a semi-empirical model that includes both the aforementioned bubble traversing effects, suitable for cases where larger bubbles are expected to be formed, such as boiling flows. Presented below is a slight modification to the original Tomiyama model, proposed by Frank et al. [43]:

$$C_L = \begin{cases} \min[0.288\tanh(0.121Re_v), f(Eo')] & Eo' \leq 4 \\ f(Eo') & 4 < Eo' \leq 10 \\ -0.27 & 10 < Eo' \end{cases} \tag{2.97}$$

where:

$$f(Eo') = 0.00105Eo'^3 - 0.0159Eo'^2 - 0.0204Eo' + 0.474 \tag{2.98}$$

Here, a modification of the standard Eötvös number is used, which instead uses the longest axis of a deformed bubble, d_h:

$$Eo' = \frac{g(\rho_l - \rho_v)d_h^2}{\sigma} \tag{2.99}$$

where:

$$d_h = d_v \left(1 + 0.163Eo^{0.757}\right)^{1/3} \tag{2.100}$$

2.3.3.3 Wall lubrication force

Mentioned in Section 2.3.3.2, small bubbles will traverse towards the walls. However, the surface tension forces will prevent them from making contact with the walls, holding them off at a short distance. This is called the wall lubrication force, and is defined as:

$$\vec{F}_{WL} = C_{WL}\alpha_v\rho_v|(\vec{u}_v - \vec{u}_l)_{\parallel}|^2\vec{n}_W \tag{2.101}$$

where:

- C_{WL} is the wall lubrication coefficient;
- $|(\vec{u}_v - \vec{u}_l)_{\parallel}|$ is the relative velocity component tangential to the wall; and
- $\vec{n}_W$ is the unit normal in the direction away from the wall.

2.3.3.3.1 Antal et al. model

Antal et al. proposed a model to account for the effects of the wall lubrication force [44]:

$$C_{WL} = \max\left(0, \frac{C_{W1}}{d_v} + \frac{C_{W2}}{y_W}\right) \tag{2.102}$$

where:

- $C_{W1} = -0.01$ and $C_{W2} = 0.05$ are empirical constants;
- d_v is the vapour bubble diameter; and
- y_W is the distance to the wall.

It can be seen that C_{WL} takes on a non-zero value when:

$$y_W \leq -\frac{C_{W2}}{C_{W1}}d_v \tag{2.103}$$

or when the distance to the wall is less than five bubble diameters. This means that this model is only compatible with meshes with high refinement in the near-wall region.

2.3.3.4 Virtual mass force

When dispersed particles move through a fluid, they encounter resistance from the surrounding fluid as they push it aside to move forward. This resistance is a result from the inertia of the surrounding fluid, and in effect, adds a "virtual mass" to the dispersed particle. This force is can be expressed as:

$$(\vec{F}_{VM}) = C_{VM}\alpha_v\rho_l\left(\frac{D(\vec{u}_l)}{Dt} - \frac{D(\vec{u}_v)}{Dt}\right) \tag{2.104}$$

where:

- C_{VM} is the virtual mass coefficient for a spherical particle, commonly set to 0.5 [45]; and
- $\frac{D(\vec{u}_l)}{Dt}$, $\frac{D(\vec{u}_v)}{Dt}$ are the material derivative of the velocity vectors of both phases.

2.3.3.5 Turbulent dispersion force

The turbulent dispersion force represents how the spatial distribution of the bubbles is influenced by turbulent eddies in the flow, by altering their trajectory in the radial direction.

In boiling flows, bubbles form on the heated walls and are subsequently driven away from the walls by turbulent eddies. This force emerges from averaging the interfacial drag term:

$$K_{vl}\left(\overline{\vec{u}}_v - \overline{\vec{u}}_l\right) = K_{vl}\left(\vec{u}_v - \vec{u}_l\right) - K_{vl}\vec{u}_{dr} \tag{2.105}$$

where:

- the first term on the left-hand side is the instantaneous drag;
- the first term on the right-hand side is the mean momentum exchange between the phases; and
- the second term is the turbulent dispersion force:

$$\vec{F}_{\mathrm{TD},l} = -\vec{F}_{\mathrm{TD},v} = K_{vl}\vec{u}_{dr} \tag{2.106}$$

Here, $\vec{u}_{dr}$ represents the drift velocity, which accounts for the dispersion of the secondary phase due to turbulent fluid motion in the continuous phase.

2.3.3.5.1 Burns et al. model

Burns et al. derived a model from Favre-averaging the interfacial drag term [46]:

$$\vec{F}_{\mathrm{TD}} = C_{\mathrm{TD}}K_{vl}\frac{D_l}{\sigma_{vl}}\left(\frac{\nabla\alpha_v}{\alpha_v} - \frac{\nabla\alpha_l}{\alpha_l}\right) \tag{2.107}$$

where:

- $C_{\mathrm{TD}} = 1$ is the turbulent dispersion coefficient;
- K_{vl} is the interfacial momentum exchange coefficient (see Eq. 2.43);
- D_l is the dispersion scalar (when using the mixture turbulence model, this is equal to the mixture turbulent kinetic energy, k);
- $\sigma_{vl} = 0.9$ is the dispersion Prandtl number; and
- $\nabla\alpha_v$, $\nabla\alpha_l$ are the gradients of the phase volume fractions.

2.3.4 Interfacial area modelling

The Eulerian-Eulerian framework is not an interface-capturing technique, and therefore modelling of the interfacial area is required.

Choosing an appropriate interfacial area modelling approach is crucial in order to accurately assess phase interactions in a multiphase flow system, primarily because all interfacial transfer processes are directly dependent on the interfacial area concentration, A_i [39], for example:

$$\text{(Interfacial Transfer Process)} \approx A_i \times \text{(Driving Force)} \tag{2.108}$$

From the above, it is therefore clear why accurate modelling of the interfacial area A_i is crucial for the meaningful simulation of multiphase flows.

Population Balance Models (PBM) are the most accurate in modelling the complexity of the relevant phenomena affecting the size and distribution of the bubbles, such as growth, expansion resulting from pressure change, coalescence, breakage, as well as nucleation mechanisms.

However, coupling PBMs with boiling models is computationally cumbersome and expensive since multiple transport equations need to be solved using various specialised methods[5]. In addition, the inclusion of PBMs also require extensive effort in terms of accurate modelling (such as the bubble populations).

In an Eulerian framework, there are two other available approaches for modelling of the interfacial area, either:

- solving a transport equation for the interfacial area concentration, or
- use of an algebraic model.

2.3.4.1 Transport equation based model

The Interfacial Area Concentration (IAC), A_i, is defined as the interfacial surface area per unit mixture volume $[m^{-1}]$. By solving a transport equation for the IAC, these models allow for the inclusion of bubble coalescence and breakage effects, as well as a distribution of bubble diameters. The transport equation for A_i is defined as:

$$\begin{aligned}\frac{\partial \rho_v A_i}{\partial t} + \nabla \cdot (\rho_v \vec{u_v} A_i) = \frac{1}{3}\frac{D\rho_v}{Dt}A_i + \frac{2}{3}\frac{\dot{m}_{lv}}{\alpha_v}A_i \\ + \rho_v(S_{TI} + S_{NU} + S_{RC} + S_{WE})\end{aligned} \tag{2.109}$$

where:

- $\frac{D\rho_v}{Dt}$ is the material derivative of the vapour density, defined as $\frac{D\rho_v}{Dt} = \frac{\partial \rho_v}{\partial t} + \nabla \cdot (\rho_v \vec{u_v})$;
- $\dot{m}_{lv}$ is the mass transfer rate of liquid transitioning to vapour phase;

[5]Such as the Method of Moments (approximating the integrals of population balance equations with a set of simpler PDEs [47])

- S_{TI}, S_{NU} are source terms for breakages due to turbulent eddies, and nucleation of bubbles; and
- S_{RC}, S_{WE} are sink terms for coalescence caused by random collisions which are in turn driven by turbulence and wake entrainment respectively.

The initial two terms on the right-hand side represent vapour bubble expansions due to compressibility and mass transfer, respectively. Ishii et al. [48], [49] made the remark that there are two additional categories of mechanisms:

- Breakage of large bubbles, as a result of flow instability on bubble surfaces; and
- Shearing-off of small bubbles from large cap bubbles.

Neither of these mechanisms are taken into account in the models presented in this thesis. Table 2.3 presents three different closure models that can be used for the transport equation model.

Table 2.3: Overview of three closure models for the transport equation based model.

	Hibiki-Ishii	**Ishii-Kim**	**Yao-Morel**
Applicability	Adiabatic bubbly flows	Adiabatic bubbly flows	Adiabatic and boiling bubbly flows
Random collisions term	Yes	Yes	Yes
Wake entrainment term	No	Yes	Yes
Turbulent interaction term	Yes	Yes	Yes
Nucleation term	No	No	Yes

The key difference between these models is the choice of experimental data used to derive the model formulations. The Yao-Morel model was validated against experiments of boiling bubbly flows, while the Hibiki-Ishii and Ishii-Kim models were not [50]. Since the latter models were validated against adiabatic air-water flows where no nucleation of bubbles occurred, the Yao-Morel model was used in this thesis.

2.3.4.1.1 Yao-Morel Model

The Yao-Morel model is an interfacial area concentration model which provides closure for the source and sink terms in Eq. 2.105. It is an extension of the Hibiki-Ishii and Ishii-Kim models that includes heterogeneous mass transfer effects [28].

The coalescence term is expressed as:

$$\Phi^{CO} = -K_{c1}\left(\frac{\varepsilon^{1/3}\alpha^2}{d_b^{11/3}}\right)\frac{1}{g(\alpha)+K_{c2}\alpha\sqrt{\frac{We}{We_c}}}\exp\left(K_{c3}\sqrt{\frac{We}{We_c r}}\right) \tag{2.110}$$

where:

- $We_{cr} = 1.24$ is the critical Weber number [51],
- ε is the turbulent dissipation rate,

- $g(\alpha)$ is a modification factor,
- $K_{c1} = 2.86$, $K_{c2} = 1.922$, and $K_{c3} = 1.017$ are model coefficients.

The sink terms can then be expressed as:

$$S_{RC} + S_{WE} = \frac{1}{3}\phi \left(\frac{\alpha}{\chi_v}\right)^2 \Phi^{CO} \tag{2.111}$$

The breakage term is defined as:

$$\Phi^{BK} = K_{b1} \left(\frac{\varepsilon^{1/3}\alpha(1-\alpha)}{d_b^{11/3}}\right) \frac{1}{1 + K_{b2}(1-\alpha)\sqrt{\frac{We}{We_c}}} \exp\left(-\frac{We}{We_c r}\right) \tag{2.112}$$

where $K_{b1} = 1.6$ and $K_{b2} = 0.42$ are model constants. The breakage source term can then be written as:

$$S_{TI} = \frac{1}{3}\phi \left(\frac{\alpha}{\chi_v}\right)^2 \Phi^{BK} \tag{2.113}$$

Finally, the nucleation source term is defined as:

$$\Phi^{NUC} = \pi d_b w^2 N_w f \frac{A_{heated}}{V} \tag{2.114}$$

where:

- $d_b w$ is the diameter of the nucleated bubble,
- N_w is the nucleation site density, and
- f is the bubble departure frequency.

2.3.4.2 Algebraic Models

The algebraic models are based on the assumption that the interface is spherical for all dispersed phase regimes. The models are deduced from the surface area to volume ratio, A_p, for a spherical bubble $[m^{-1}]$:

$$A_p = \frac{\pi d_p^2}{\frac{1}{6}\pi d_p^3} = \frac{6}{d_p} \tag{2.115}$$

The types of algebraic models include:

2.3.4.2.1 Particle Model

This model defines the interfacial area density as:

$$A_i = \alpha_p A_p = \frac{6\alpha_p}{d_p} \tag{2.116}$$

where index p denotes the dispersed phase.

2.3.4.2.2 Symmetric Model

This model treats both phases symmetrically, where phases p and q can be continuous or dispersed.

$$A_i = \frac{6\alpha_q\alpha_p}{d_{(p,q)}} \tag{2.117}$$

where $d_{(p,q)}$ is the characteristic length scale, defined as:

$$d_{(p,q)} = \begin{cases} d_p, & \text{if phase } p \text{ is dispersed,} \\ \alpha_q d_p + \alpha_p d_q, & \text{if both phases are dispersed.} \end{cases}$$

This model is suitable for cases where the secondary phase is expected to be dispersed in one region of the domain and the continuous phase in another, which is true for boiling flows with phase inversion. This is why this sub-model was used in this thesis.

2.3.5 Summary of boiling-related models

Two different mass transfer models have been discussed so far, along with various approaches for the interfacial area modelling, heat transfer modelling, and momentum transfer modelling. Note that these models do not differ in many areas. The main differences lie in how the mass transfer rate is calculated: in the Lee model, user-defined mass transfer coefficients govern the rate of vaporization, whereas in the Thermal Phase Change model, the rate is governed directly by the heat transfer coefficients, which can be calculated in different ways.

Regarding heat transfer, the Lee model is only compatible with the single-resistance approach, while the Thermal Phase Change model is paired with the double-resistance approach. However, if a zero-resistance criterion for the interface-to-vapour side is specified, then the two-resistance approach can mimic the single-resistance approach. These methods were investigated further in this thesis.

In terms of interfacial force modelling, after surveying the literature, one sub-model for each interfacial force was selected. The chosen sub-models are presented in Table 5.

For interfacial area modelling, the transport equation model (more specifically the Yao-Morel model) appears to be more physically grounded than the algebraic models. This is because an additional transport equation is solved for the interfacial area concentration, including source and sink terms for bubble dynamics, while the algebraic models calculate the interfacial area concentration based only on the volume fractions and user-defined bubble diameter. Therefore, the effects of these methods, particularly the Yao-Morel and Symmetric algebraic models, will be investigated further.

Table 2.4: Comparison of the Lee and Thermal Phase Change models.

Model properties	Lee model	TPC model
Type of model	Evaporation/ Condensation. Volumetric mass transfer	Evaporation/ Condensation. Volumetric mass transfer.
Assumptions	Flat interface, well-dispersed bubbles, constant bubble diameter	General interface, well-dispersed bubbles, constant bubble diameter
Calculation of mass transfer rate	Governed by mass transfer coefficients	Governed by heat transfer coefficients
Inclusion of microscopic boiling phenomena	Disregards microscopic phenomena	Disregards microscopic phenomena
Calculation of HTC	Single-resistance approach	"Quasi" single-resistance[6] Double-resistance approach
Computational cost	Low	High
Expected outcomes	Prediction of wall temperatures, ONB, dry-out location	Prediction of wall temperatures, ONB, dry-out location

Table 2.5: Interfacial momentum transfer sub-model choices.

Interfacial force	Sub-model choice
Drag force	Symmetric
Lift force	Tomiyama
Wall lubrication force	Antal et al.
Virtual mass force	$C_{VM} = 0.5$
Turbulent dispersion force	Burns et al.

[6]The TPC model can be arranged to mimic the single-resistance configuration of the Lee model by selecting a zero-resistance model for the interface-to-vapour resistance

3
Experimental study

The aim of this thesis was to assess the robustness and overall predictive capability of various boiling models concerning flow boiling patterns and the resulting heat transfer coefficients for tubes oriented horizontally, using water as the working medium. These assessments can then be used to facilitate a more accurate prediction of the heat transfer characteristics of a preliminary heat exchanger design.

Many studies analyzed the heat transfer behavior of horizontally oriented tubes, but few provided sufficiently detailed experimental data for Computational Fluid Dynamics (CFD) validation. Among those that did report the required data, none used water as the working medium; instead, they used various refrigerants, as horizontal heat exchanger tubes are most commonly found in air conditioning units [52]. To draw conclusions about the phase change behavior of water, an experimental study using refrigerants with similar vapor/liquid density would be ideal [1].

Numerous studies have analyzed vertically oriented tubes, providing detailed data suitable for CFD validation [53], [54]. However, vertical orientation results in significantly different flow structures compared to horizontally oriented tubes. This difference is attributed to gravity being parallel to the axial flow in vertical tubes, whereas in horizontally oriented tubes, it acts orthogonally to the axial flow. Consequently, the physics governing the flow structures and interfacial interactions cannot be expected to be similar between the two orientations.

Finally, an experimental study by Jige et al. was deemed to provide sufficiently detailed data for CFD validation [52]. The paper included analysis of heat transfer behavior and pressure drop for horizontal copper tubes with inner diameters of 1.00, 2.16, and 3.48 mm, using R32 as the working medium. This refrigerant has a vapor/liquid density ratio of $\rho_v/\rho_l \approx 0.035$ for the operating pressure used in the study (1.2808 MPa), which is comparable to that of water, $\rho_v/\rho_l \approx 0.00745$, at the same pressure [55].

3.1 Jige et al.

In this section, the experimental study by Jige et al. [52] will be described. They conducted single- and two-phase experiments in a horizontally oriented, circular tube constructed in smooth copper. R32 was used as the working medium, entering the tube inlet at a saturation temperature of 15°C, corresponding to an operating pressure of 1.2808 MPa [55].

3.1.1 Layout and Specifications

3.1.1.1 Test Loop

The refrigerant flow was driven through the test-loop (see Fig 3.1) by a magnetic-drive gear pump (1). First, the mass flow rate was measured using a Coriolis mass flow meter (2), and then regulated by valves situated in the main and bypass loops. Then, the refrigerant was cooled in a water heat exchanger (3), after which it was heated to a saturation temperature of 15°C by an electric pre-heater (4). Thereafter, the fluid entered the test section (5) and then returned to the pump through a condenser (6), liquid receiver (7), and sub-cooler (8). The bulk temperatures were measured with K-type encased thermocouples at the inlet of the electric pre-heater, and at the inlet and outlet of the test section.

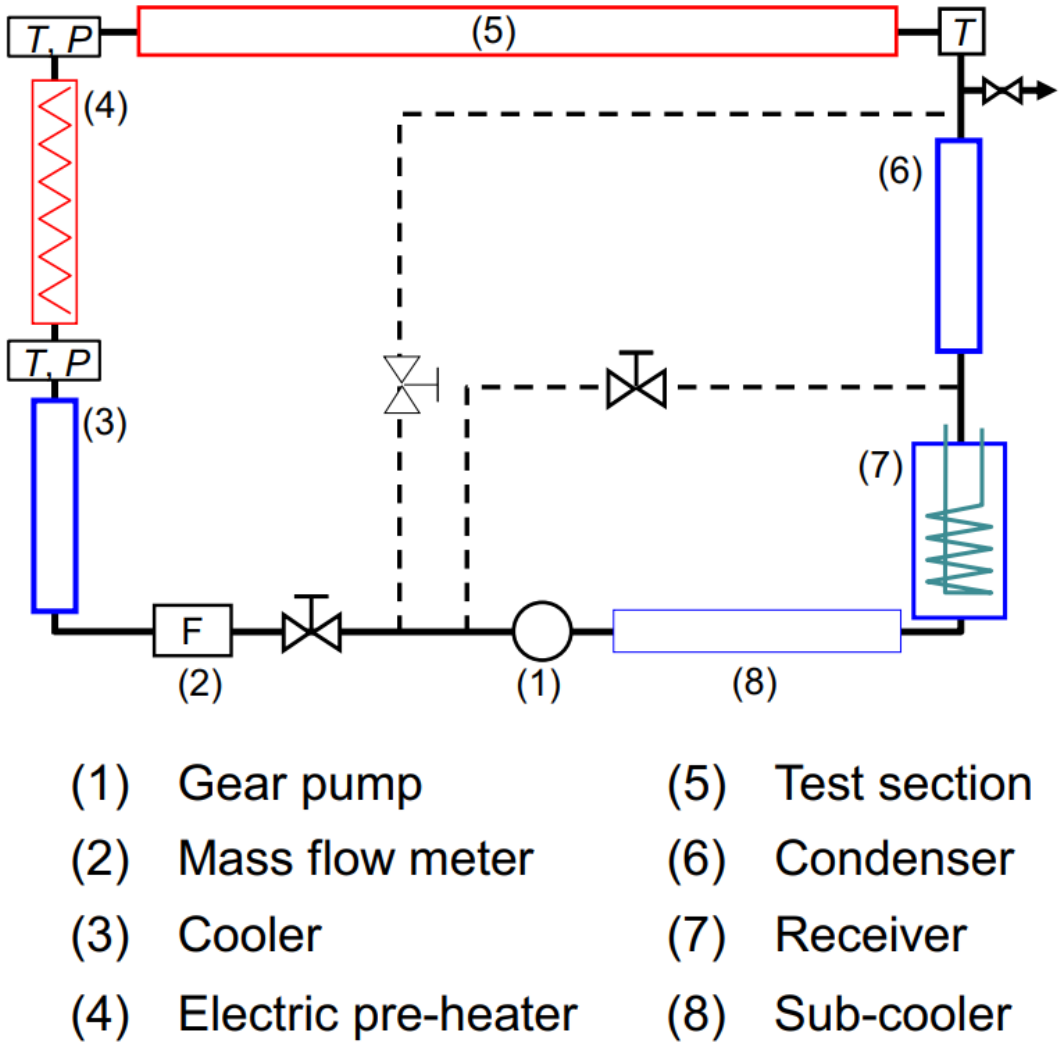

Figure 3.1: Schematic view of the experimental setup [52].

3.1.1.2 Test section

The test section had a total length of 750mm, of which 400 and 550 mm are the measurement lengths for effective heat and pressure drop, respectively (see Figure 19). Jige et al. analysed three different inner tube diameters: 1.0, 2.2, and 3.5mm. The experimental data from the latter size was chosen since it is similar the inner tube diameter expected in aero engine heat exchangers.

T-type thermocouple wires were placed on the top and bottom of the tube at eight locations in order to measure wall temperature throughout the heated section. The inlet pressure was measured using an absolute pressure transducer. The pressure drop between the test section inlet and outlet was measured with a differential pressure transducer. The accuracies of the measurement instrumentation can be seen in Table 6.

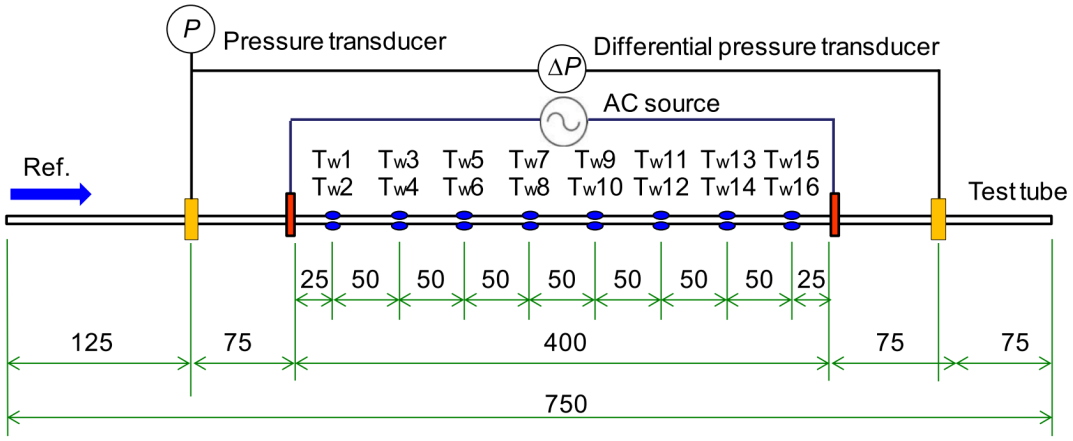

Figure 3.2: Schematic view of the test section and the measurement points [52].

Table 3.1: Accuracy of the measurement instrumentation.

Measurement instrumentation	Accuracy
Coriolis mass flow meter	±0.5%
K-type thermocouples	±0.05K
T-type thermocouples	±0.05K
Absolute pressure transducer	±1.4kPa
Differential pressure transducer	±0.2kPa

The maximum uncertainty of the measured Heat Transfer Coefficient (HTC) was estimated to 25% under the following conditions: a mass flux of $400\frac{\text{kg}}{\text{m}^2\text{s}}$, a heat flux of $5\frac{\text{kW}}{\text{m}^2}$,an outlet vapor quality of 0.9, and a tube diameter of 1.0 mm. These conditions were used for the uncertainty analysis since it was expected to occur at low heat flux, high mass flux, and low vapor quality as that would yield a high HTC and a small temperature difference. The uncertainty regarding measured pressure drop was evaluated to $1\% - 16\%$.

4
Numerical modelling

4.1 Mesh

Low-Re grids have refined near-wall cells which can resolve the thermal and viscous boundary layers with higher accuracy compared to high-Re grids with wall functions. Therefore, a structured low-Re hexa-grid with $y^+ < 1$ was utilized, in combination with the $k - \omega$ SST turbulence model (see Table 4.1 for grid properties). No wall thickness was included in the meshes.

The test tube used by Jige et al. included additional sections up- and downstream of the pressure measurement locations, and these were included in the grids. This is beneficial since the upstream extension would ensure full development of the turbulence flow profile before the pressure measurement location. The length required for full flow development can be calculated using Eq. 4.1, a correlation for turbulent internal flow [56]:

$$L = 4.4Re^{1/6}D \tag{4.1}$$

The extended inlet section was 125mm long, greater than the calculated development length of 76mm, $L/D \approx 22$ (for $Re = 15,500$, the highest of the cases analysed in this thesis).

Regarding the downstream extension, it offset the numerical outlet from the interesting zone of the domain, minimizing the influence of spurious numerical behaviour.

4.1.1 Mesh independence study

The degree to which the computational domain is discretized directly affects the accuracy of the simulation. At some point, this effect will disappear and further refinement will not affect the outcome. Refinement comes with increased computational expense which in turn extends simulation times. Hence, it is excessive to use a mesh with higher refinement than what is necessary to achieve mesh independence.

In this investigation, five different grid sizes were examined, with incremental refinement in the radial and axial directions (see Table 4.1). Cross-sectional views of the grids can be seen in Fig. 4.1, as well as a side-view of the 200k cells grid in Fig. 4.2. Further, the numerical setup used for the independence study can be seen in Table 4.2.

Table 4.1: Properties of the five low-Re grids.

No. of cells	y+	First layer height [mm]	Axial cell length [mm]
25000	∼2[1]	0,016	5
50000	∼1	0,008	4
100000	∼1	0,008	2,5
200000	∼1	0,006	2
500000	∼0.5	0,004	1,33

Table 4.2: Numerical setup for the mesh independence study.

Physical process	Modelling approach
Mass transfer	Lee model (default coefficient)
Momentum transfer	Drag force (symmetric)
Heat transfer	Ranz-Marshall (single-resistance)
Interfacial area	Algebraic (ia-symmetric)
Solution methods	**Scheme**
Pressure-Velocity Coupling	Coupled (solve N-phase volume fraction eqs.)
Gradient	Least Squares Cell Based
Pressure	PRESTO!
Momentum	QUICK
Volume Fraction	Modified HRIC
Turbulent Kinetic Energy	QUICK
Specific Dissipation Rate	QUICK
Energy	QUICK

[1]Although y+ should ideally be less than 1, in this case, a mesh with 25,000 cells and a y+ close to 1 would result in only a few cells between the walls and the centre, leading to an abrupt transition between the cells. To avoid this, the calculated non-dimensional wall distance was kept slightly above 1 to preserve mesh smoothness

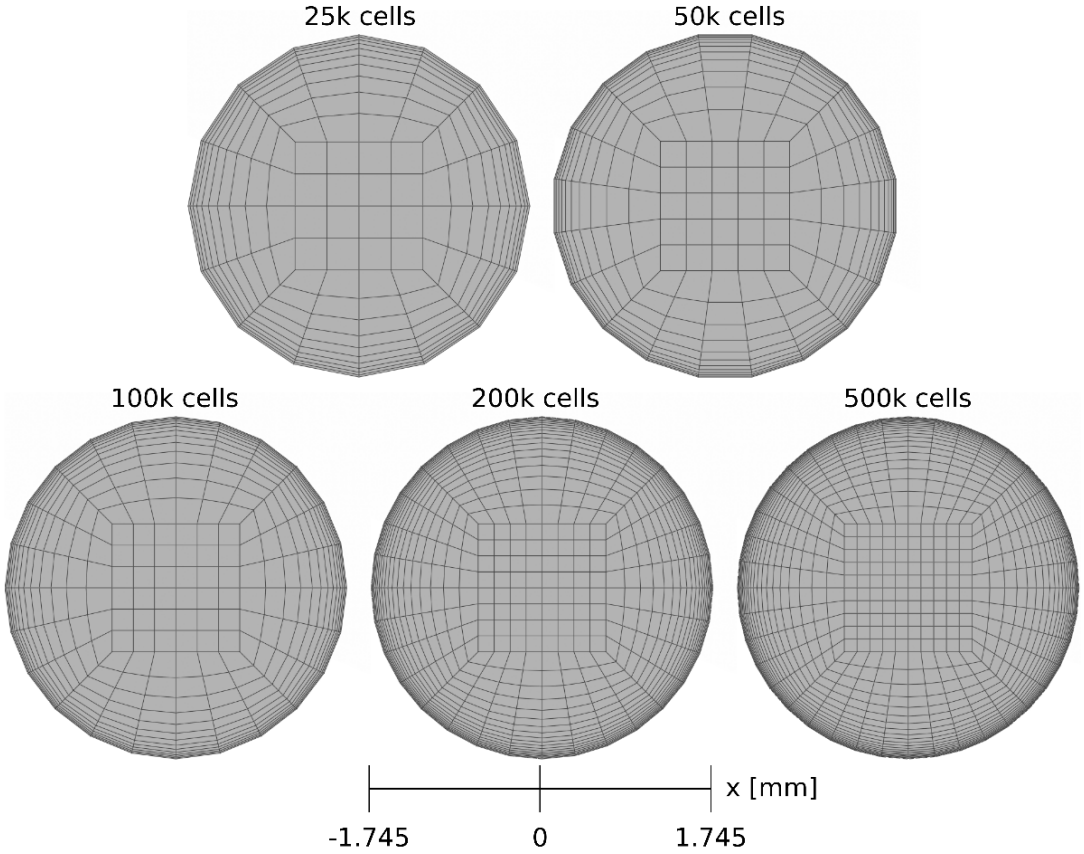

Figure 4.1: Cross-sectional view of the five meshes.

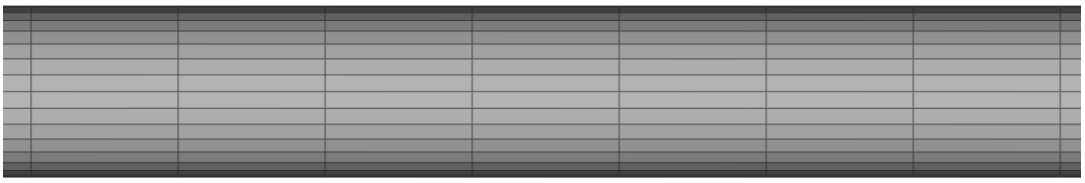

Figure 4.2: Axial view of the 200k cell mesh.

The grid sensitivity analysis was focused on the area-averaged outlet vapour quality and area-averaged wall temperature of the heated test section, since these are the most significant parameters affecting the boiling characteristics of the domain.

In addition, the effect of defining the refrigerant properties using Real Gas Property (RGP) compared to specifying constant properties was also analysed. The difference in vapour quality and wall temperature between these two approaches was negligible (see Fig. 4.2 and 4.3). However, for higher mass transfer coefficients, leading to a larger degree of vaporization of the liquid, the difference might become more significant.

It can be observed that both vapour quality and wall temperature start to even out between 200k and 500k cells, but do not completely converge. The absolute

difference in vapour quality between the meshes were 0.0003, and 0.278K in terms of the wall temperature. However, the relative error in vapour quality between 200k and 500k cells was quite large. Nevertheless, other flow variables (such as vapour volume fraction and mass transfer rate) did not display such a discrepancy, indicating that the solutions might not have converged enough to make a proper judgement of the small values observed of the vapour qualities. With this in mind, the 200k cell mesh was deemed sufficiently fine to be utilized in the later simulations.

There were attempts to generate meshes with even higher refinement, but as the near-wall cells got smaller, numerical instabilities became more prominent. Therefore, it was concluded that the gains in numerical accuracy in relation to the increased computational effort required to run simulations for these even finer grids, were unwarranted.

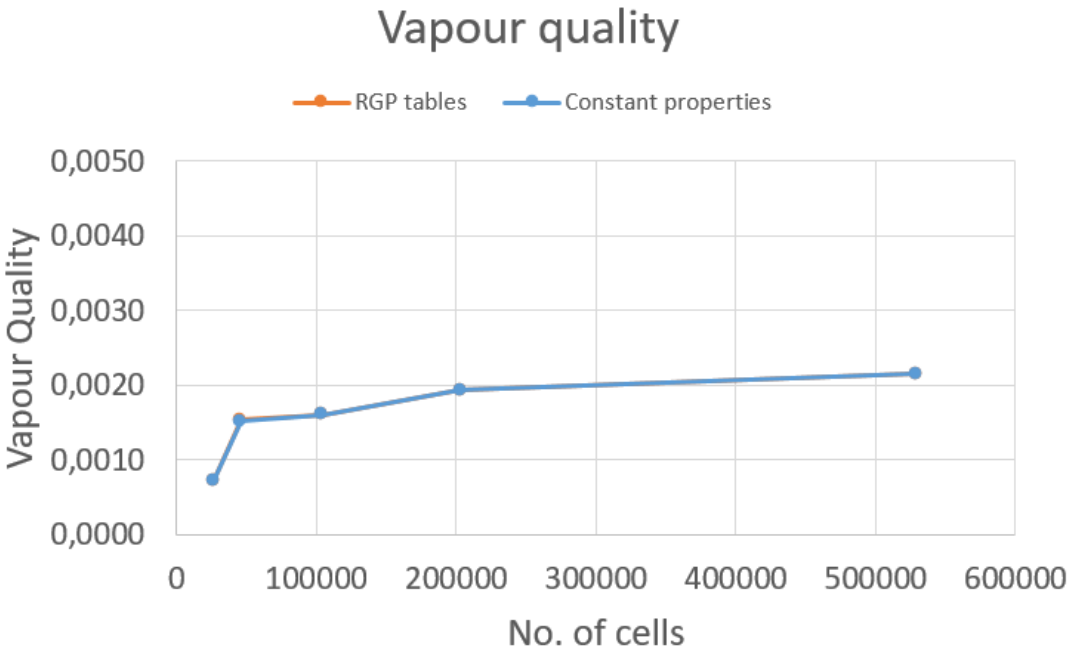

Figure 4.3: Plot of vapour quality against the no. of cells in each mesh.

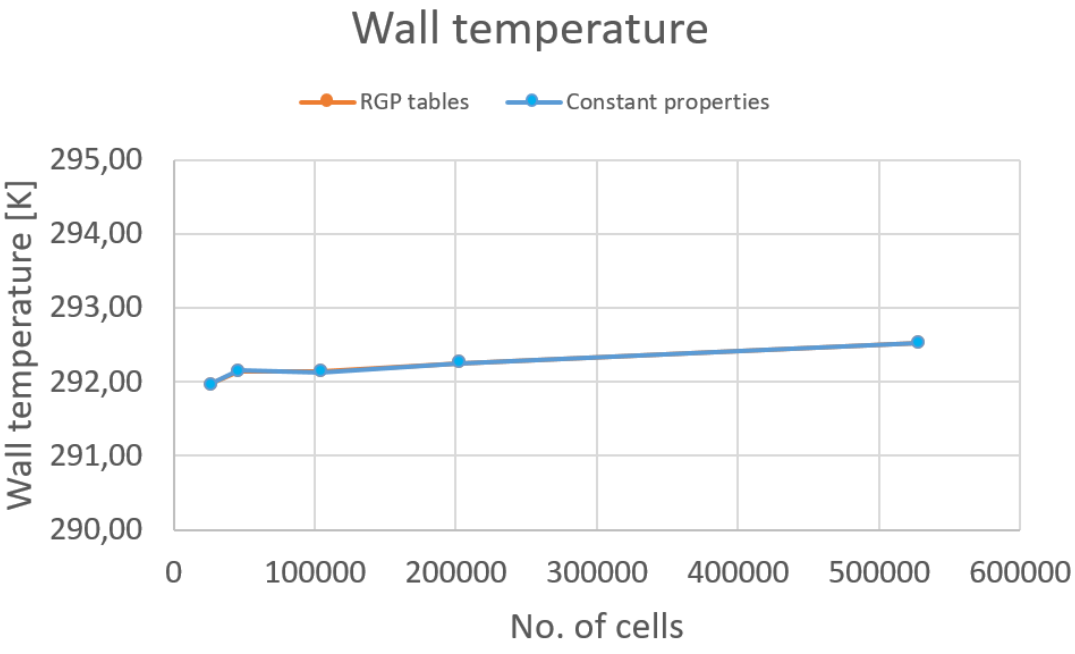

Figure 4.4: Plot of wall temperature against the no. of cells in each mesh.

4.2 Base solver configuration

The computations for this investigation were conducted using steady-state simulations on the 3D geometry presented in Section 4.1. The solver used was ANSYS Fluent[2]with double precision accuracy enabled. Liquid and vapour properties for R32 were obtained from the NIST Standard Reference Database 23, Version 9.5 [55], and a mass-flow inlet boundary condition was applied at the inlet, while a pressure outlet was set at the outlet. Additionally, a constant heat flux was specified at the wall of the heated section.

For Pressure-Velocity coupling, coupled with volume fractions scheme (Solve N-phase vol. frac. eqs.) was selected, which solves phase volume fraction equations for both the primary and secondary phase. With this scheme, the resulting volume fractions are scaled to satisfy that the sum of them equals 1. While this method is more computationally demanding than solving for only one phase, it has shown to improve convergence behaviour.

The spatial discretization schemes used in the numerical simulations are presented in Table 4.3. The Pseudo Time Stepping Method was used to improve convergence behaviour, which uses a pseudo-transient approach to converge to the steady-state solution. The $k-\omega$ SST model was used for turbulence modelling.

Table 4.3: Spatial discretization schemes used for the single- and multiphase simulations.

Spatial Discretization	Scheme
Gradient	Least Squares Cell Based
Pressure	PRESTO!
Momentum	QUICK
Volume Fraction[3]	Modified HRIC
Turbulent Kinetic Energy	QUICK
Specific Dissipation Rate	QUICK
Energy	QUICK

[2]Release 2023r1
[3]Multiphase simulations only

4.3 Solution strategies

Because of the convergence difficulties which have often been reported when solving multiphase fluid simulations, a specific "solution strategy" intended to make achieving a stable and acceptably converged simulation was devised.

For most cases, the following steps were followed:

1. The solution was initialized with 100% liquid at inlet temperature condition with adiabatic walls.
2. Thereafter, a custom-written UDF was used to ramp up the wall heat flux in small steps until the final heat flux was reached (see Appendix A). This strategy considerably improved convergence behaviour compared to cases in which the full heat flux was applied immediately. If the solver still had convergence issues, the heat flux step size was decreased, and the number of iterations per heat flux step were increased. Further, if convergence issues were still experienced, the time scale factor used in the pseudo-transient formulation was also decreased.
3. Initially, first order schemes were used for the momentum, volume fraction, turbulent kinetic energy, specific dissipation rate, and energy equations.
4. Thereafter, after a converged solution had been achieved at the final heat flux, the spatial discretization was then switched to the higher order QUICK[4]scheme (except for volume fraction where the Modified HRIC scheme was used).

4.4 Convergence criteria

The solution was deemed converged once the residuals, as well as the area-averaged volume fraction at the outlet of the heated section as well as the area-averaged wall temperatures reached constant levels.

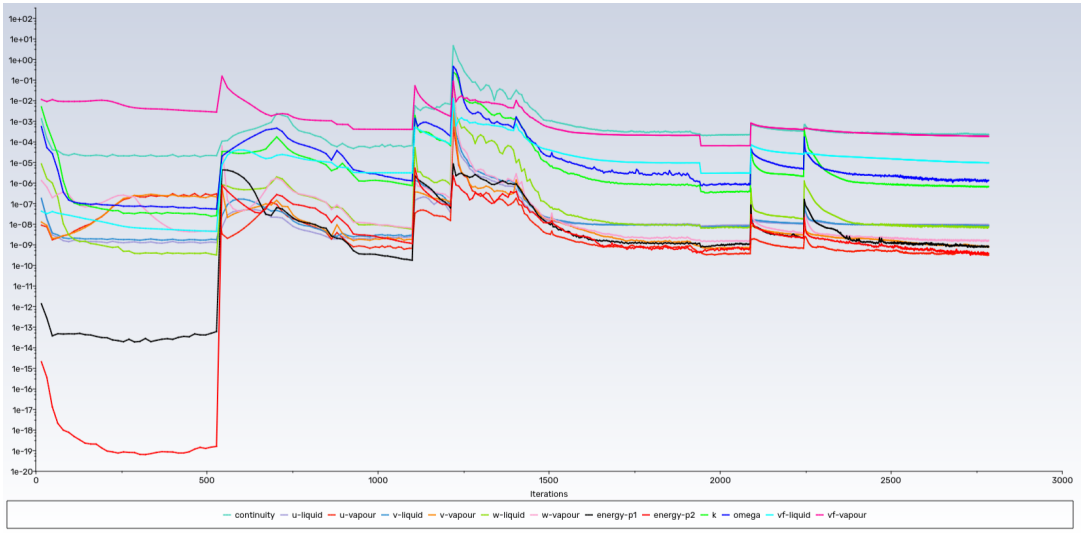

Figure 4.5: Example of the relative residuals of a converged solution.

[4]Quadratic Upwind Interpolation for Convective Kinematics

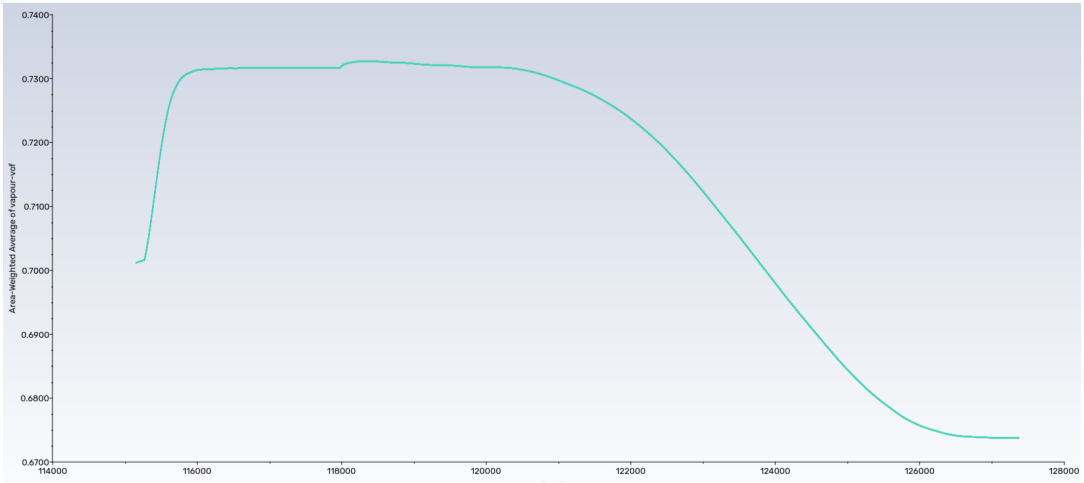

Figure 4.6: Example of an area-averaged outlet volume fraction monitor for final simulation configuration for a multiphase case (that is, with the maximum wall heat flux and final solver configuration (spatial discretization).

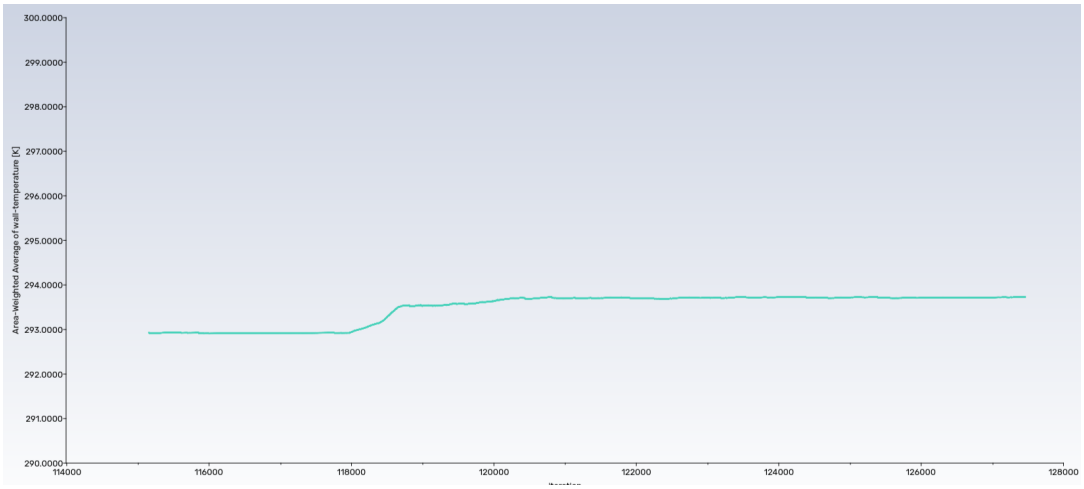

Figure 4.7: Example of an area-averaged wall temperature monitor for final simulation configuration for multiphase case.

5
Results

5.1 Numerical results

In this section, the numerical results from the CFD simulations are presented. Single-phase simulations were conducted to examine the capability of the mesh to predict the pressure drop and heat transfer behaviour observed in the single-phase experimental data. Subsequently, multiphase simulations were carried out and compared against the multiphase experimental data.

5.1.1 Single-phase simulations

Prior to commencing multiphase simulations, single-phase (liquid) simulations were performed with the boundary conditions from the liquid-only experimental runs described in Jige et al (see Table 5.1).

These results were subsequently compared with well-established correlations for single-phase heat transfer and pressure drop. The purpose of this exercise was to acquire a sense of the accuracy of CFD compared to correlations for simpler systems, like single-phase flows.

Table 5.1: Boundary conditions for the single-phase experiments.

Parameter	Value
Inlet temperature [°C]	10
Operating pressure [MPa]	1.2808
Wall heat flux [$\frac{kW}{m^2}$]	2.5-10
Re	4700-23500
Pr	1.76

5.1.1.1 Heat Transfer Coefficients

In Figure 5.1, the predicted HTCs from CFD and three different correlations are compared against the experimental data. It can be seen that all three correlations matched the experimental data with very good accuracy, whereas the CFD slightly overpredicted the HTCs. Further, this effect was more noticeable for lower Re. Nonetheless, the average deviation was 17.7% which was deemed acceptable, since convective heat transfer is known to be a challenging phenomenon to model with CFD [57].

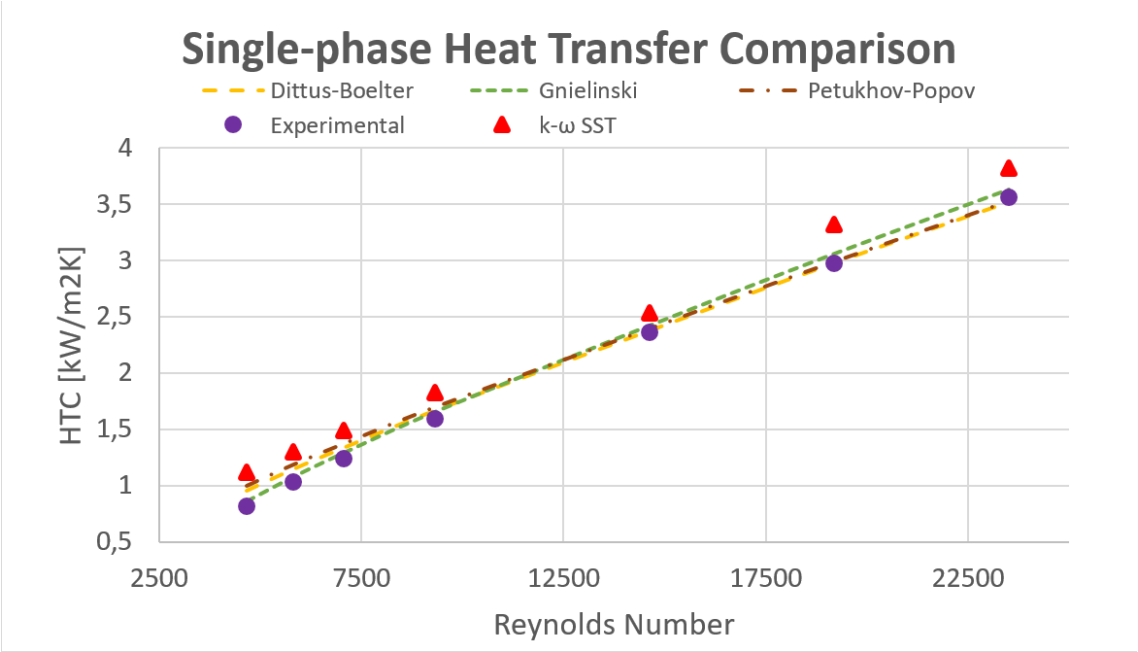

Figure 5.1: Plot of predicted HTC from single-phase heat transfer correlations and CFD against experimental data.

5.1.1.2 Pressure Drop

In regards to pressure drop, the CFD results matched experimental data with an average deviation of 0.85%. The mesh could thereby be considered sufficient for simulating more complex systems, such as multiphase flows.

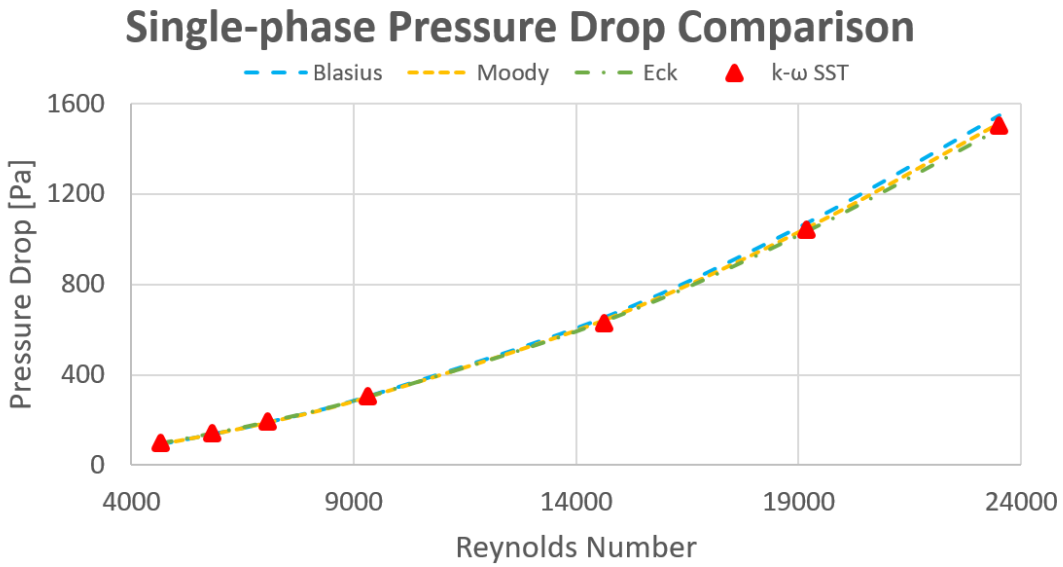

Figure 5.2: Plot of predicted pressure from single-phase correlations against CFD results.

5.1.1.3 Summary

The single-phase CFD simulations showed good agreement with experimental data and correlations for heat transfer and pressure drop. The average deviation of the CFD-predicted pressure drop was 0.85%, whereas it reached 17.7% for Nusselt numbers. Such a discrepancy was expected, as convective heat transfer has been acknowledged by other authors to be challenging to model accurately. Hence, the deviation from experimental data was considered acceptable.

5.1.2 Multiphase Simulations

The results of the multiphase simulations are now presented in this section. This encompasses a sub-model study aimed at assessing and selecting the appropriate sub-models. It also involves comparing the numerical results from the Lee and Thermal Phase Change models with experimental data using default and tuned mass transfer coefficients. Additionally, it includes the outcomes of modeling thermal diffusion in the tube walls by incorporating wall thickness into the mesh.

5.1.2.1 Test Cases

Jige et al. ran a series of experimental runs, varying mass, heat fluxes, and inner tube diameter. Out of those runs, the two cases that were expected to produce the least and the most amount of vapour were chosen for the numerical simulations (see Table 5.2).

In the study, both cases had outlet vapour qualities of ~ 1, but modeling boiling flows with default mass transfer coefficients could result in lower values. Hence, running the boiling models for the two extreme cases would give insight into the degree of tuning required for the numerical simulations.

Table 5.2: Experimental conditions for the 3.5mm diameter tube.

Parameter	Case 1	Case 2
d_i $[mm]$	3.5	3.5
q $[\frac{W}{m^2}]$	5000	20000
G $[\frac{kg}{m^2 s}]$	400	100
T_{in} [°C]	15	15
Operating pressure [MPa]	1.2808	1.2808

The inner diameter was kept at 3.5mm, as this dimension is closer to what might be expected in a commercial aerospace heat exchanger. In the study by Jige et al., the data was reported in vapour quality[1]instead of vapour volume fraction. Volume fraction can easily be converted to vapour quality with the following expression:

$$x = \frac{\alpha_v \rho_v}{\alpha_v \rho_v + \alpha_l \rho_l} \tag{5.1}$$

[1]Equivalent to the vapour mass fraction

5.1.2.2 Survey of available sub models

The goal of the thesis was to assess the accuracy and robustness of different boiling models.

For a given multiphase framework, accuracy relies on the inclusion of relevant sub-models in order to capture important physical phenomena present in the flow, whereas robust models exhibit low numerical instabilities and are easily applicable. Finding a balance between these two factors was therefore crucial. As such, an investigation was conducted to conclude which phenomena required modelling or could be neglected. This included evaluating the relative importance of various different sub-models in terms of their impact on the overall predictive capability of the simulation framework.

The sub-model survey was divided into four parts:

- Impact of interfacial area modelling,
- Impact of heat transfer modelling[2],
- Impact of turbulence modelling, and finally
- Impact of momentum transfer (i.e. force) modelling.

Each of the analyses was conducted starting with a base case known to be robust (see Table 5.3).

5.1.2.2.1 Base configuration

The simulations were conducted using the boundary conditions equivalent to those used in Case 1.

Table 5.3: Sub-models included in the base configuration.

Physical phenomenon	Chosen sub-model
Mass transfer	Lee model, TPC model
Interfacial area	Algebraic (ia-symmetric)
Heat transfer	Ranz-Marshall (Lee), Ranz-Marshall and zero-resistance (TPC)
Momentum transfer	Drag force (symmetric)
Turbulence model	$k-\omega$ SST model

An algebraic interfacial area model was selected for numerical stability, except for in the force analysis in which a transport equation formulation was used. This is because the transport equation-based model calculates the interfacial area concentration while considering bubble-bubble and bubble-turbulence interactions, while the algebraic model does not [48]–[50]. Additionally, the drag force was expected to be very significant in the flow domain, and was included in each of the numerical setups.

[2]I.e. the impact of different thermal resistance (single- or double) models

Regarding the heat transfer modeling, the single- and double-resistance approaches were compared within the Thermal Phase Change model. This is because the Lee model is only compatible with the single-resistance approach, as discussed previously in Section 2.3.2. The sub-models for the liquid-to-interface heat transfer were formulated in similar ways, and no significant differences in results were expected. Therefore, the Ranz-Marshall model was applied for all simulations using the Lee model.

In regards to the Thermal Phase Change model (which relies on the double-resistance approach), a zero-resistance model was specified on the vapour side of the interface. In effect, this made the heat transfer modeling setup equivalent to the single-resistance used with the Lee model.

With the baseline numerical setup defined, this configuration was then used to investigate the effects each of the following sub-models had on the solution.

5.1.2.2.2 Interfacial area modeling

First, the most suitable sub-model for each interfacial area modeling approach was investigated. Among the available algebraic models, the symmetric model was chosen since its formulation allows both phases to be continuous or dispersed in different regions of the tube.

For the transport equation model, the Yao-Morel closure sub-model was selected since it included terms describing nucleation of bubbles and was developed from flow boiling experiments, and this was therefore considered most appropriate for the work in this project [50].

In Table 5.4 and Figs. 5.3 - 5.6, the results from the interfacial area modeling analysis are presented. Using default mass transfer coefficients resulted in significantly different outlet vapour qualities between the two boiling models. For the Lee model, the transport equation formulation yielded a higher outlet vapour volume fraction compared to the algebraic formulation. However, the outlet vapour quality was comparatively lower. This discrepancy arises because vapour quality depends on phase densities. Therefore, the difference is likely due to variations in the predicted densities by the two interfacial area concentration models.
For the Thermal Phase Change model, the vapour quality was significantly lower for the transport equation formulation. It is unclear which specific terms contributed to this.

For the Lee model, the transport equation formulation promoted greater bubble formation early in the tube. This could be attributed to the nucleation term in the Yao-Morel model (Eq. 2.112), a phenomenon not accounted for in the algebraic formulation. However, this was not the case for the TPC model in combination with the Yao-Morel model, where less vapour was produced early in the tube. The reason for this discrepancy was not immediately clear, but it is expected that further analysis will be required to reconcile this difference.

The transport equation approach exhibited worse convergence behavior and produced

marginal difference in results. Therefore, the algebraic formulation was deemed as the appropriate approach for the multiphase simulations.

Table 5.4: Results from the interfacial area modelling analysis. Table shows area-averaged vapour quality at the heated section outlet and area-averaged wall temperature from the heated section wall.

Lee	**Vapour quality**	**Wall temperature [K]**
Algebraic	0.0016	292.21
Transport eq.	0.0007	292.05
TPC	**Vapour quality**	**Wall temperature [K]**
Algebraic	0.1055	289.14
Transport eq.	0.0030	289.31
Experimental	0.9450	288.98

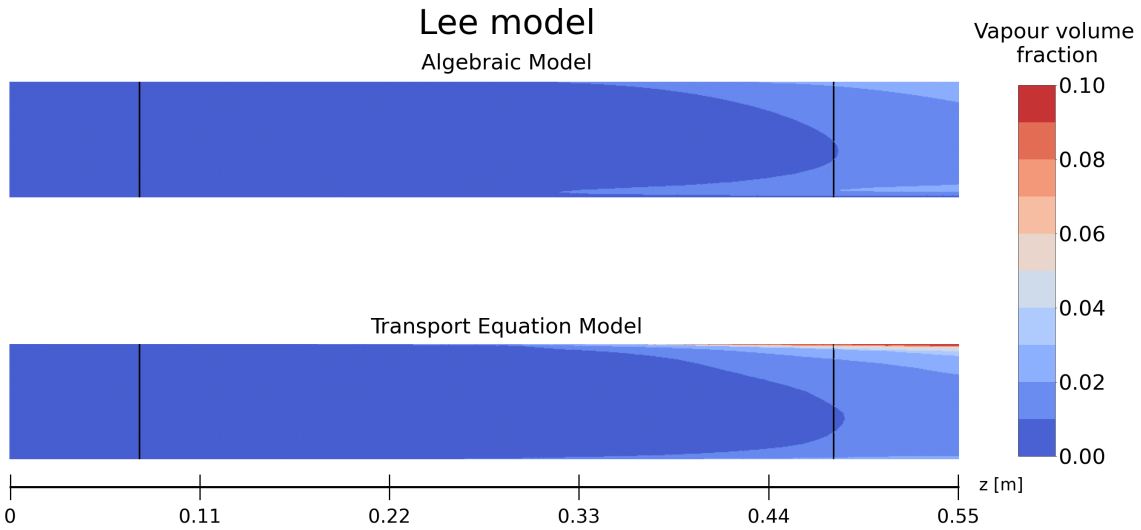

Figure 5.3: Comparison of interfacial area models with the Lee model. Contours showing vapour volume fraction in the axial direction.

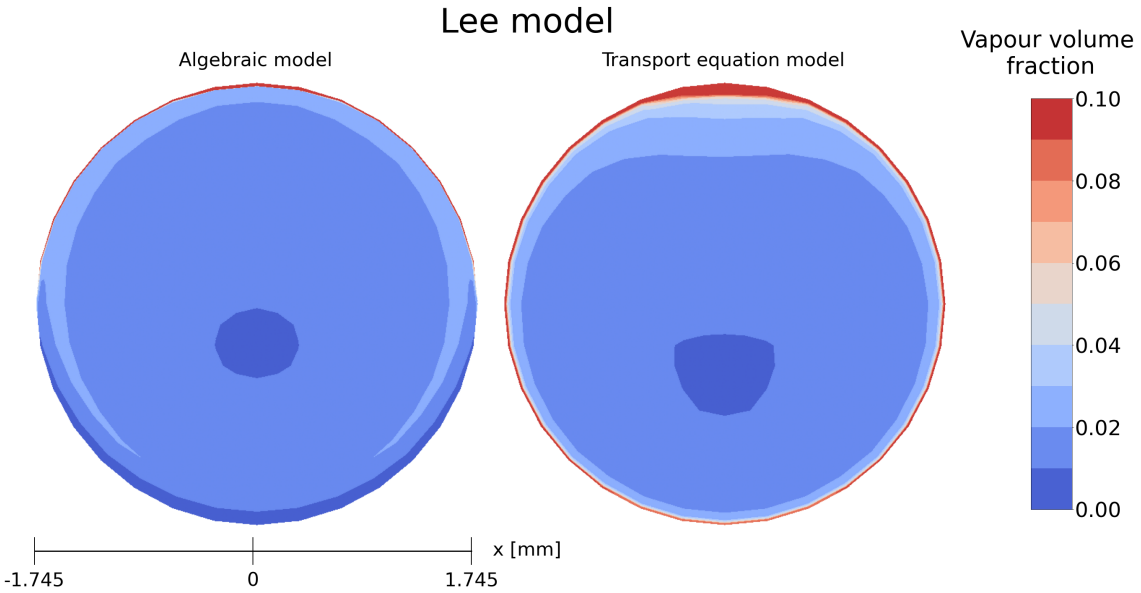

Figure 5.4: Comparison of interfacial area models with the Lee model. Contours showing vapour volume fraction in the radial direction (cross-sectional view of the test section outlet).

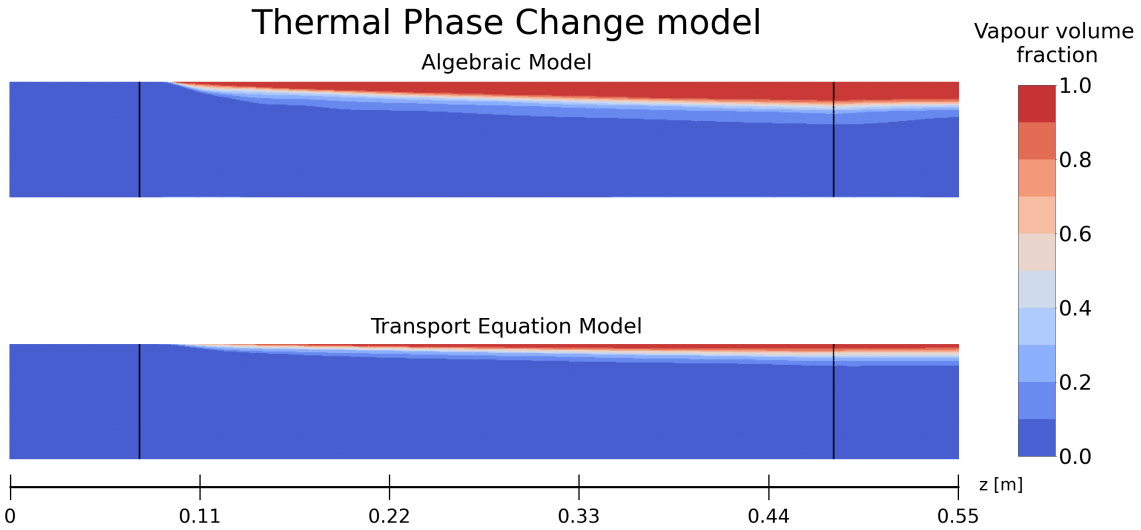

Figure 5.5: Comparison of interfacial area models with the Thermal Phase Change model. Contours showing vapour volume fraction in the axial direction.

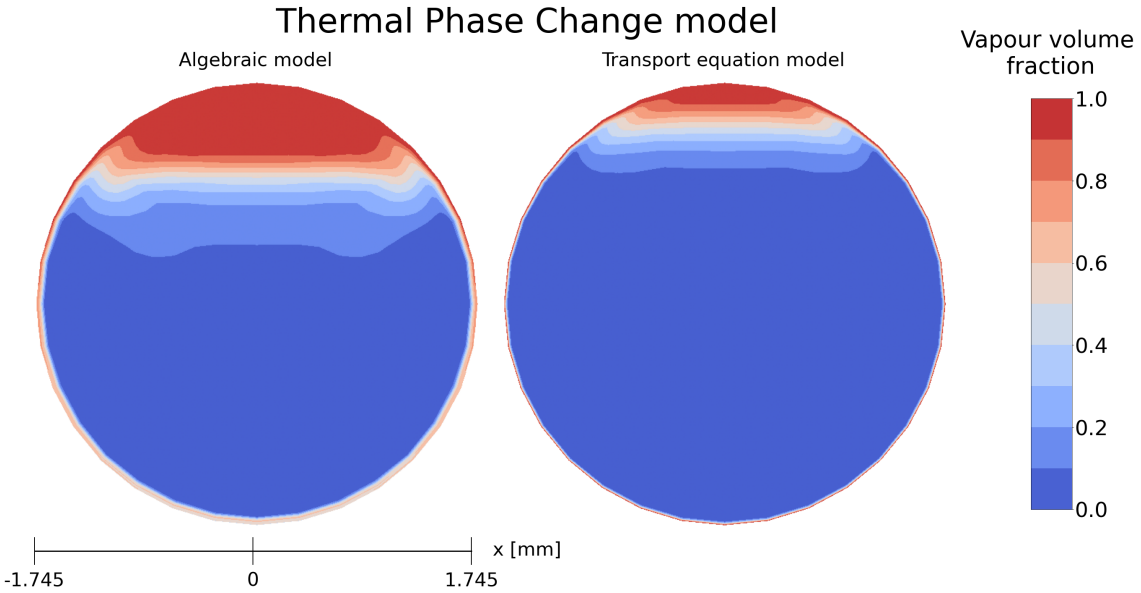

Figure 5.6: Comparison of interfacial area models with the Thermal Phase Change model. Contours showing vapour volume fraction in the radial direction (cross-sectional view of the test section outlet).

5.1.2.2.3 Heat transfer modelling

In this section, the single- and double-resistance approaches are directly compared. As discussed previously (Section 2.3.2.2), the double-resistance approach cannot be coupled with the Lee model. Hence, this investigation was only carried out with the Thermal Phase model.

The results from the single-resistance and double-resistance approaches with the Thermal Phase Change model are shown in Table 5.5 and Figs 5.7 and 5.8, respectively.

The double-resistance approach yielded comparatively higher wall temperatures. This is because the thermal energy exerted by the wall could not be transferred through the vapour phase as readily (as a result of the additional resistance of the double-resistance approach) in comparison to the single-resistance approach.

Further, it was noted that for the final solutions, the overall area-averaged vapour quality was substantially larger for the double-resistance approach when compared to the single-resistance model.

Table 5.5: Results from the heat transfer modelling analysis. Table shows area-averaged vapour quality at the heated section outlet and area-averaged wall temperature from the heated section wall.

TPC model	Vapour quality	Wall temperature [K]
Single-resistance (Ranz-Marshall, Zero resistance)	0.1055	289.14
Double-resistance (Ranz-Marshall, Constant Time Scale)	0.1836	305.63
Experimental	0.9450	288.98

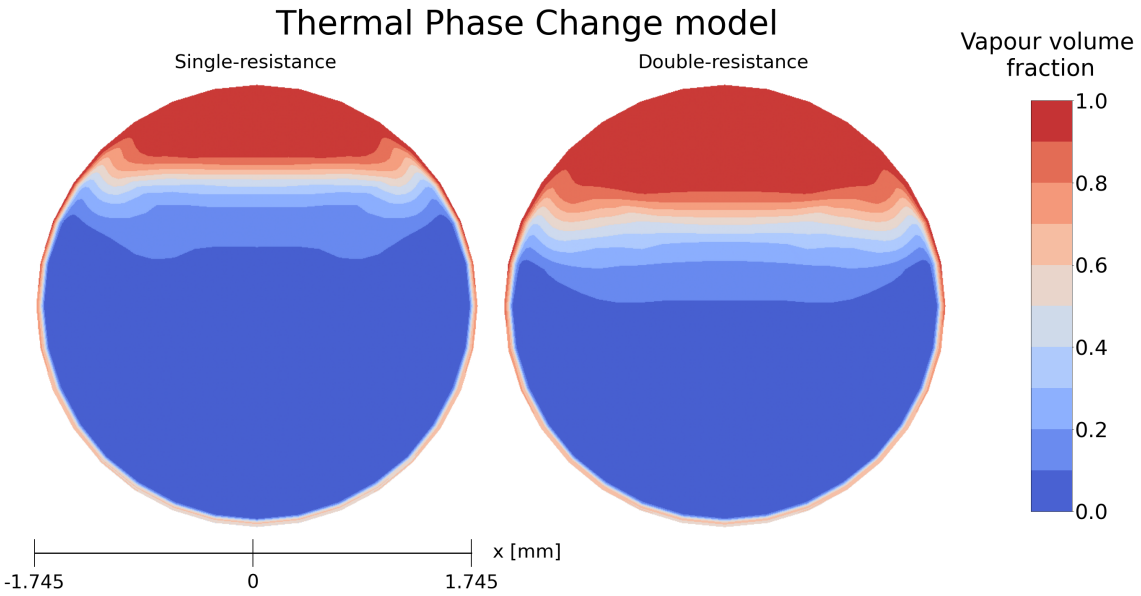

Figure 5.7: Comparison of the single- and double-resistance approaches with the Thermal Phase Change model. Contours showing vapour volume fraction in the radial direction (cross-sectional view of the test section outlet).

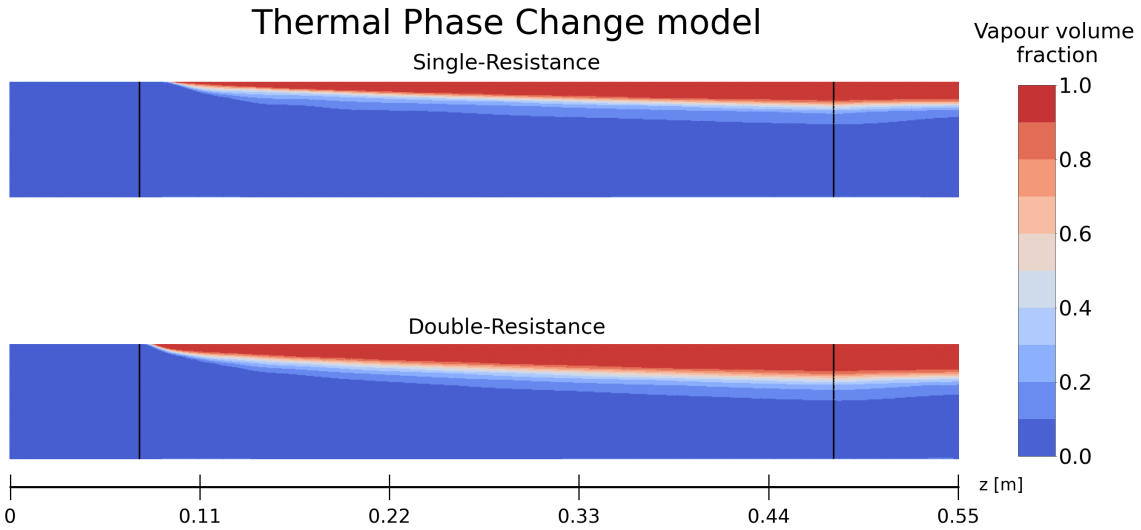

Figure 5.8: Comparison of heat transfer models with the Thermal Phase Change model. Contours showing vapour volume fraction in the axial direction.

5.1.2.2.4 Turbulence modelling

In addition to the above, in this survey, three different turbulence modelling configurations were also investigated for both the Lee and TPC models. These were:

- $k-\omega$ SST (mixture)
- $k-\omega$ SST (per phase)
- $k-\varepsilon$ (per phase with Enhanced Wall Treatment)

The numerical results are presented in Table 5.6 and Figs. 5.9–5.12.

For all three turbulence configurations, no significant differences in vapour quality or wall temperature were observed. The largest discrepancy was observed for the standard $k-\varepsilon$ model with enhanced wall treatment, which yielded higher vapour quality. This discrepancy is believed to stem from inaccurate modelling of turbulent behaviour in the near-wall regions by the wall functions [58]. This leads to an over-prediction of turbulent quantities and, consequently, enhanced heat transfer and vaporization rates due to increased flow mixing.

Further, it was noted that solving the turbulence equations for both phases on a per phase basis often led to numerical difficulties for the solver; therefore, the mixture formulation was used for the remainder of the thesis.

Table 5.6: Results from the turbulence modelling analysis. Table shows area-averaged vapour quality at the heated section outlet and area-averaged wall temperature from the heated section wall.

Lee model	**Vapour quality**	**Wall temperature [K]**
Mixture, $k-\omega$ SST	0.0016	292.21
Per Phase, $k-\omega$ SST	0.0014	292.08
Per Phase, $k-\varepsilon$ (Enhanced Wall Treatment)	0.0013	292.09
TPC model	**Vapour quality**	**Wall temperature [K]**
Mixture, $k-\omega$ SST	0.1055	289.14
Per Phase, $k-\omega$ SST	0.1051	289.25
Per Phase, $k-\varepsilon$ (Enhanced Wall Treatment)	0.1166	289.44
Experimental	0.9450	288.98

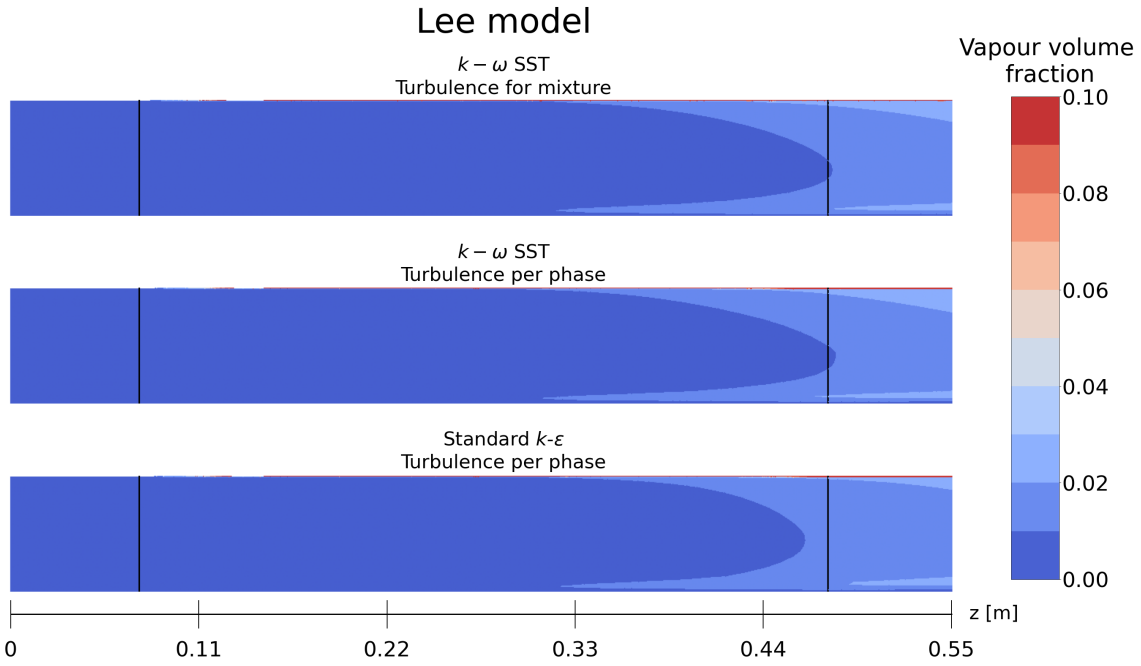

Figure 5.9: Comparison of turbulence models with the Lee model. Contours showing vapour volume fraction in the axial direction.

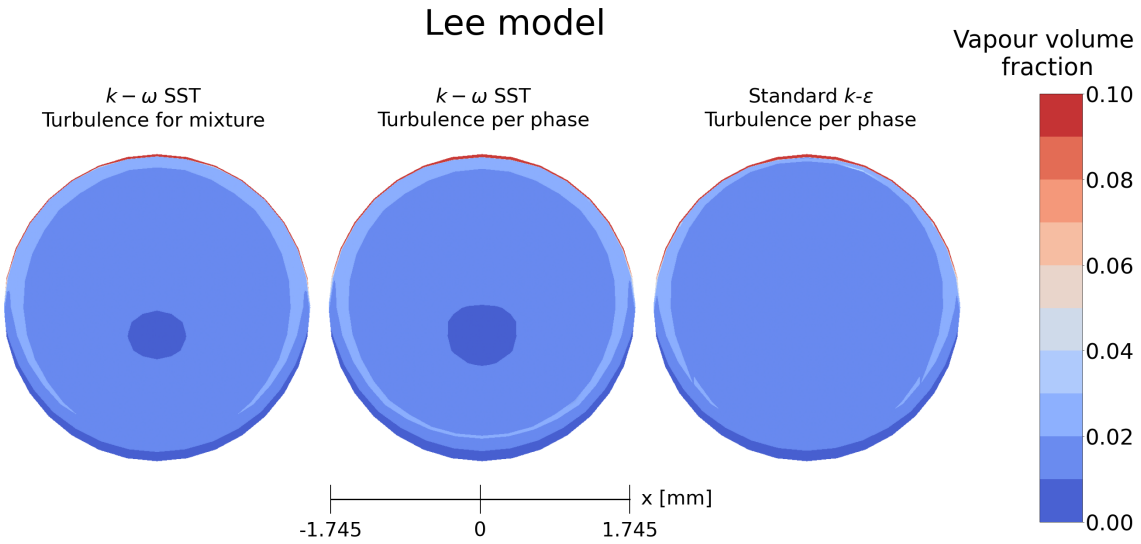

Figure 5.10: Comparison of turbulence models with the Lee model. Contours showing vapour volume fraction in the radial direction (cross-sectional view of the test section outlet).

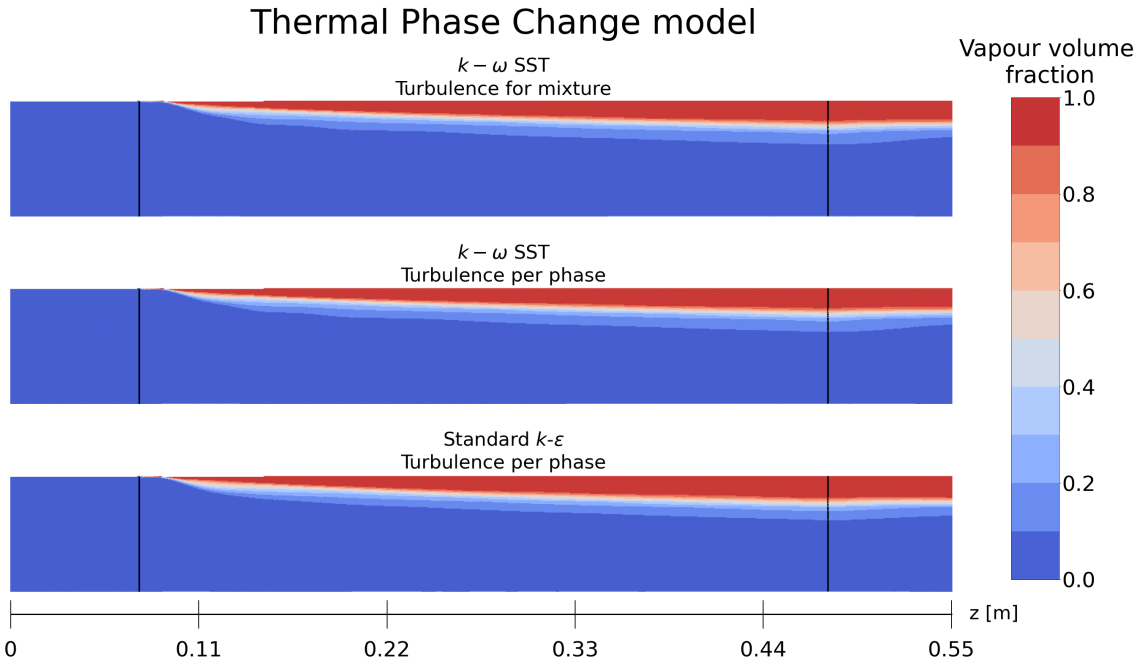

Figure 5.11: Comparison of turbulence models with the Thermal Phase Change model. Contours showing vapour volume fraction in the axial direction.

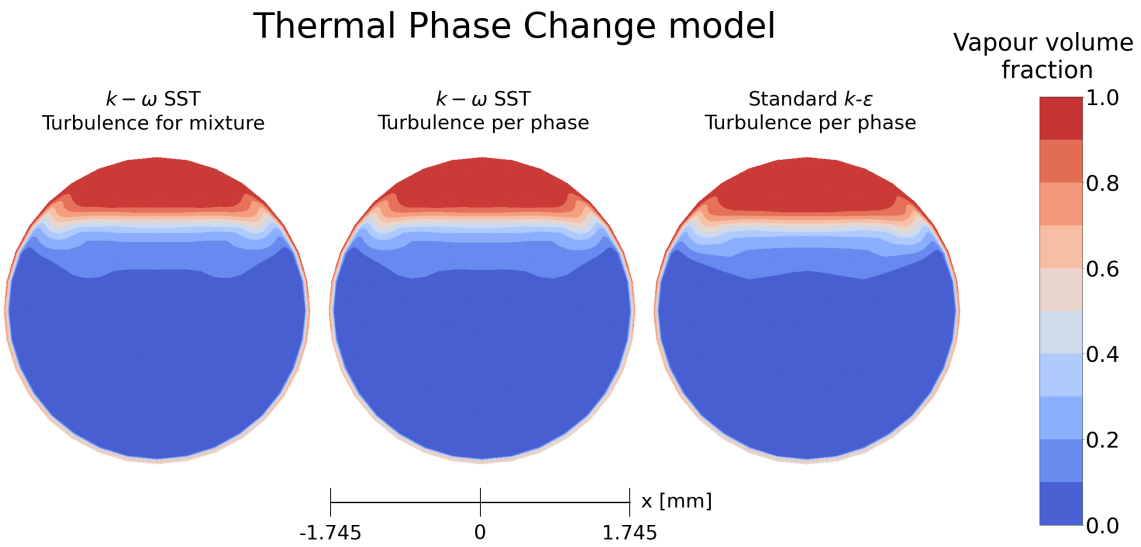

Figure 5.12: Comparison of turbulence models with the Thermal Phase Change model. Contours showing vapour volume fraction in the radial direction (cross-sectional view of the test section outlet).

5.1.2.2.5 Force modelling

The results from the momentum transfer survey can be seen in Table 5.7 and Figs. 5.13, 5.14. For all cases, the inclusion of the forces had little effect on wall temperature; nonetheless, the greatest deviation when comparing the effects of changes to the force modelling was observed when dispersion due to turbulence forces was included in the simulation configuration.

Once again, the vapour quality from all numerical results was significantly lower than the experimental data, and all cases showed consistent vapour qualities apart from when the aforementioned turbulent dispersion was included, which resulted in a large decrease in vapour quality.

The turbulent dispersion force was expected to increase the vaporization rate (rather than decrease it, as was noted from this sub-model investigation), since it was expected that more mixing should result in more effective heat transfer in fluids. However, although this was not the case, the inclusion of this force did (as indicated above) result in significant effects on the overall heat transfer characteristics of the system, and therefore, it is suggested that modelling of the turbulent dispersion force should be included when possible[3].

[3]That is, when inclusion of these forces does not result in convergence difficulties

Table 5.7: Results from the force modelling survey. Table shows area-averaged vapour quality at the heated section outlet and area-averaged wall temperature from the heated section wall.

Lee model	Vapour quality	Wall temperature [K]
Drag only	0.00073	292.05
Drag + Lift	0.00076	292.06
Drag + Turbulent Dispersion	0.00004	291.96
Drag + Added mass	0.00076	292.06
Drag + Wall lubrication	0.00076	292.06
Experimental	0.94500	288.98

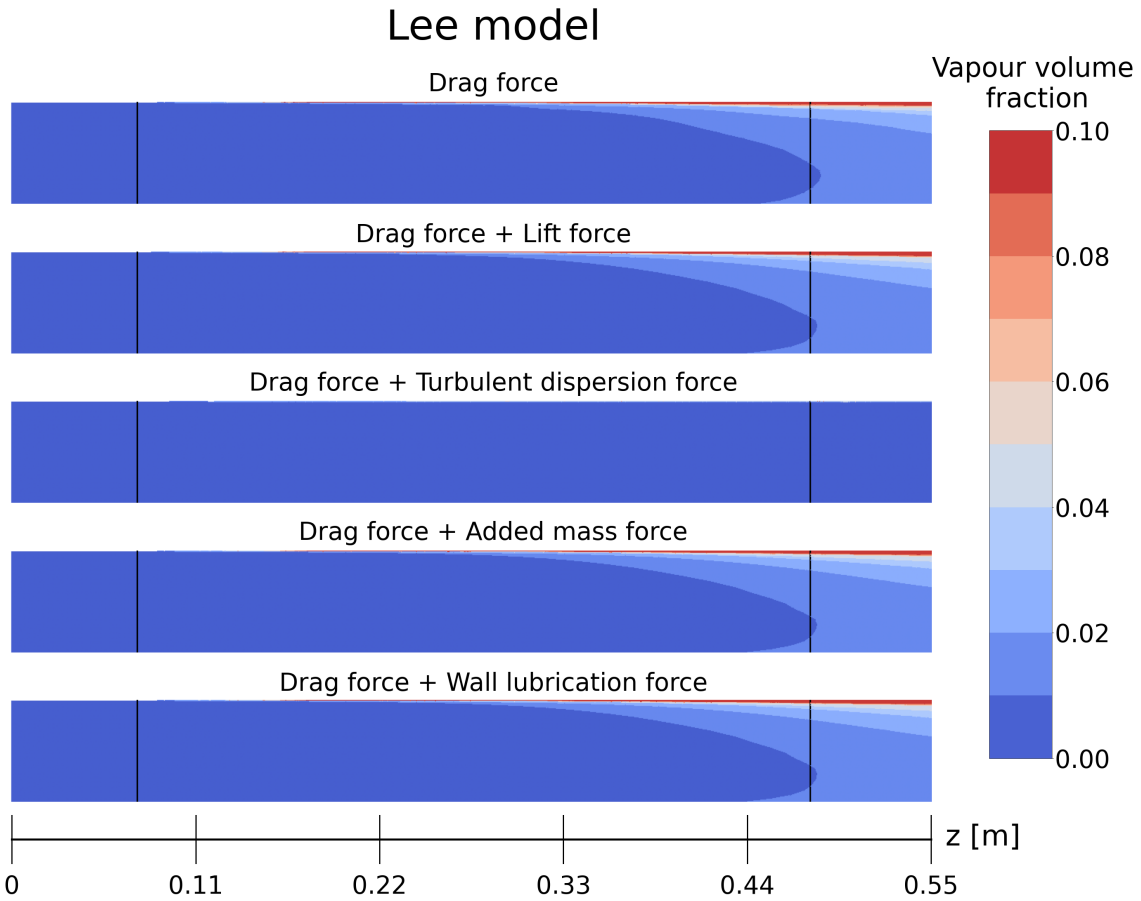

Figure 5.13: Comparison of different force configurations with the Lee model. Contours showing vapour volume fraction in the axial direction.

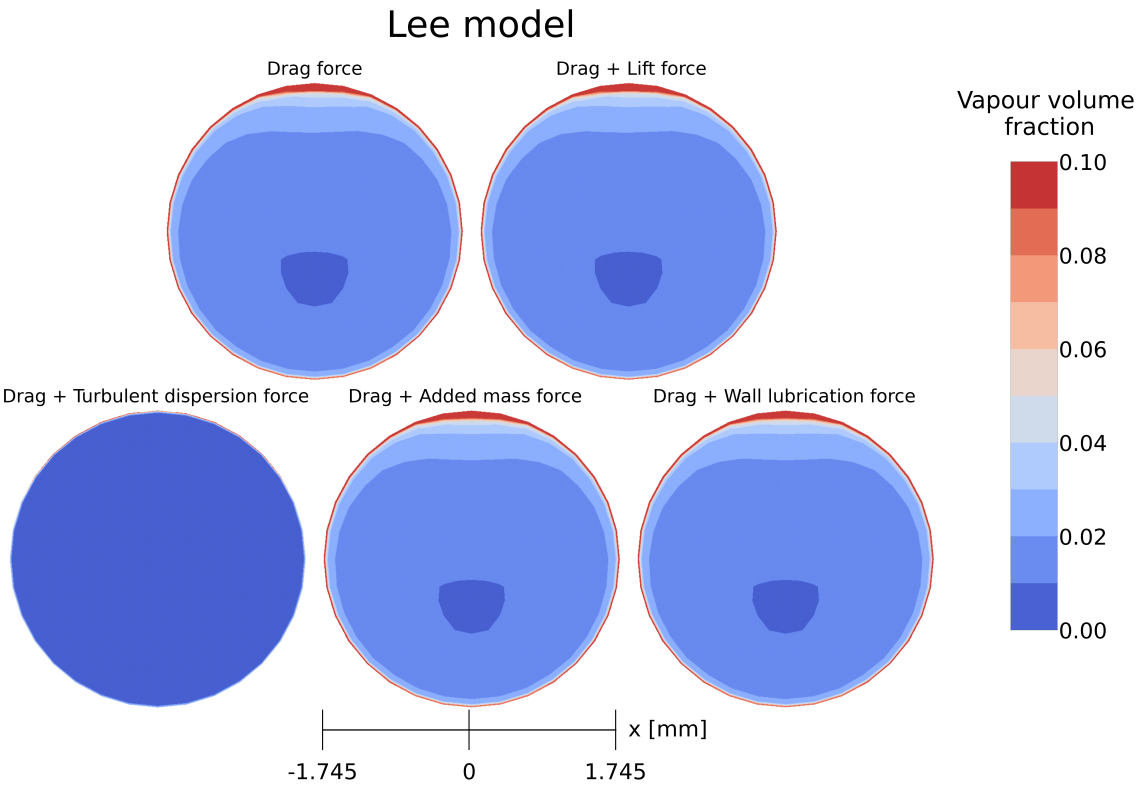

Figure 5.14: Comparison of different force configurations with the Lee model. Contours showing vapour volume fraction in the radial direction (cross-sectional view of the test section outlet).

5.1.2.2.6 Summary

The vapour quality from all numerical results were significantly lower than the experimental data, which were $x \approx 0.95$ for all but one experimental run. This suggested that tuning of the mass transfer coefficients was required for both the Lee and TPC models, in order to more accurately represent the experimental data.

Further, the transport equation formulation promoted greater bubble formation early on in the tube for the Lee model and this was considered consistent with the understanding that this model (the transport equation model for IAC modelling) should promote greater vapour mass fractions as a result of the term considering the nucleation of bubbles. However, despite this being the case for the Lee model, this was not the case for the TPC model, for which the transport equation formulation for the IAC resulted in a lower amount of vapour being produced, leaving some uncertainty about the effects of the transport equation approach in comparison to the algebraic formulation. In addition, it was found that the transport equation model tended to show increased convergence difficulties in comparison to the algebraic formulation, for the same problem configurations, and so overall the algebraic formulation was considered the best approach to use in general multiphase simulations.

In terms of the heat transfer modelling, the double-resistance approach produced

substantially higher wall temperatures and vapour qualities, indicating that explicit modelling of the interface-to-vapour thermal resistance (in addition to the liquid-to-interface thermal resistance) is important when undertaking multiphase simulations. However, as was the case with the transport equation modelling of the IAC, use of the double resistance heat transfer model also resulted in increased difficulties in the convergence behaviour of the simulations at hand, and so, for general purpose computations, the single-resistance approach was recommended.

In terms of the turbulence modelling for the multiphase simulations, no significant differences in vapour quality or wall temperature were observed when using the different turbulent model setups. However, amongst the configurations which were tested, the largest discrepancy was observed for the standard k-ε model with enhanced wall treatment, which yielded higher vapour quality in comparison to the remaining configurations. Further, solving the two transport equations for both phases often led to numerical difficulties for the solver; therefore, once again, the most suitable approach for use for the remainder of the thesis was considered the mixture formulation.

Finally, regarding the interfacial momentum transfer modelling (i.e. force modelling), all cases showed consistent results in wall temperature and vapour quality except for when the turbulent dispersion forces were modelled. Most notably, this case produced a large decrease in vapour quality when compared to the other cases.
In Table 5.8, the sub-model configuration for the multiphase simulations is summarized.

Table 5.8: Multiphase model configuration.

Modelled phenomena	Model choice
Interfacial area concentration	Algebraic (Symmetric)
Heat transfer	Single-resistance (Lee and TPC)
Turbulence	Mixture, $k-\omega$ SST
Momentum transfer	Drag (Symmetric)

5.1.2.3 Comparison with experiments and correlations

In this section, numerical results obtained from the multiphase simulations are compared against experimental data and established correlations. This analysis was essential for assessing the accuracy of the different modeling approaches surveyed in the previous section. The section is divided into three parts:

- Results using default coefficients;
- Results using tuned coefficients; and
- Results with conjugate heat transfer[4].

[4]The heat transfer between solid bodies and fluids. In this thesis, this corresponds to inclusion of the tube walls in the mesh.

5.1.2.3.1 Default coefficients

In the first part, the performance of the numerical setups are evaluated against experimental data and two-phase heat transfer correlations. This baseline assessment provides an understanding of the inaccuracies and limitations of the unmodified models.

Numerical simulations were run with boundary conditions equivalent to two experimental runs, Case 1 and 2 (see Section 5.1.2.1). The results are presented in Figs 5.15 and 5.16 together with the experimental data and correlations.

Unlike the single-phase simulations, the multiphase simulations matched the experimental data with much less accuracy. Further, as discussed previously (Section 5.1.2.2.1), the mass transfer models heavily under-predicted the vapour quality for both cases. However, for Case 2, the vapour quality was higher. This outcome was anticipated due to the lower mass flux and higher heat flux, which allows the liquid phase to absorb more energy and vaporize over a longer period.

In terms of heat transfer coefficients, the Lee model yielded lower values compared to those observed in the experiments for both cases. One possible explanation for this discrepancy is that the model inherits the tendency to over-predict wall temperatures.

The TPC model out-performed the Lee model in both aspects, as the predicted vapour quality and heat transfer coefficients were somewhat closer to the experimental results. However, the predicted values still deviated significantly from the experimental data.

In regards to the correlations, Kandlikar's correlation over-predicted the heat transfer coefficients for both cases, whereas the Chen and Liu-Winterton correlations under-predicted them. However, the latter two exhibited close agreement for Case 1.

The primary conclusion drawn from this analysis is that the mass transfer models lack the ability to predict heat transfer behavior of horizontal boiling flows without tuned coefficients.

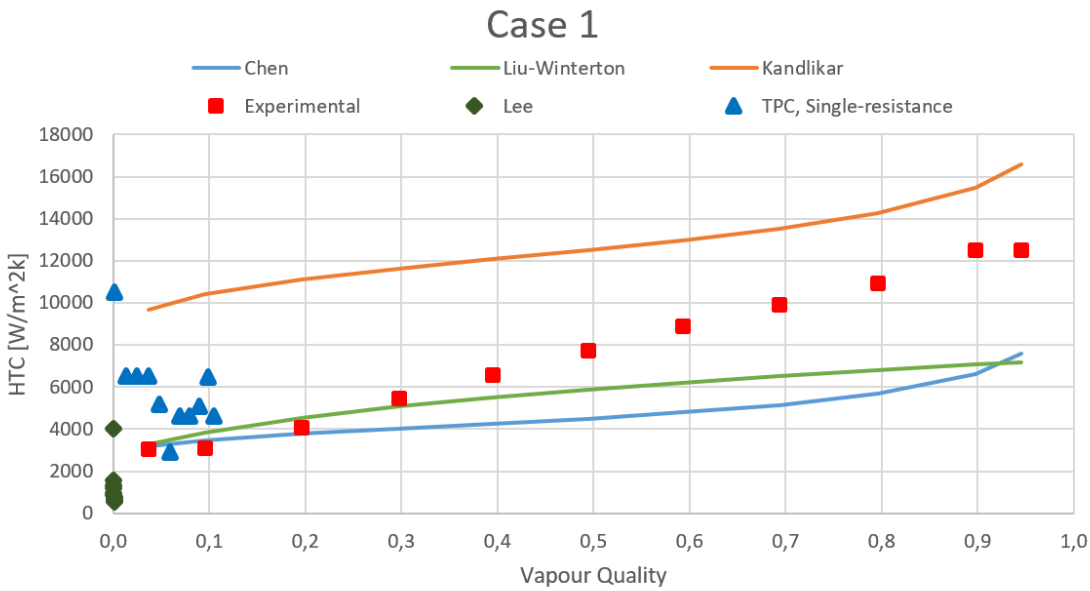

Figure 5.15: Predicted HTCs of the Lee and Thermal Phase Change models with default coefficients for Case 1, compared against experimental data and correlations.

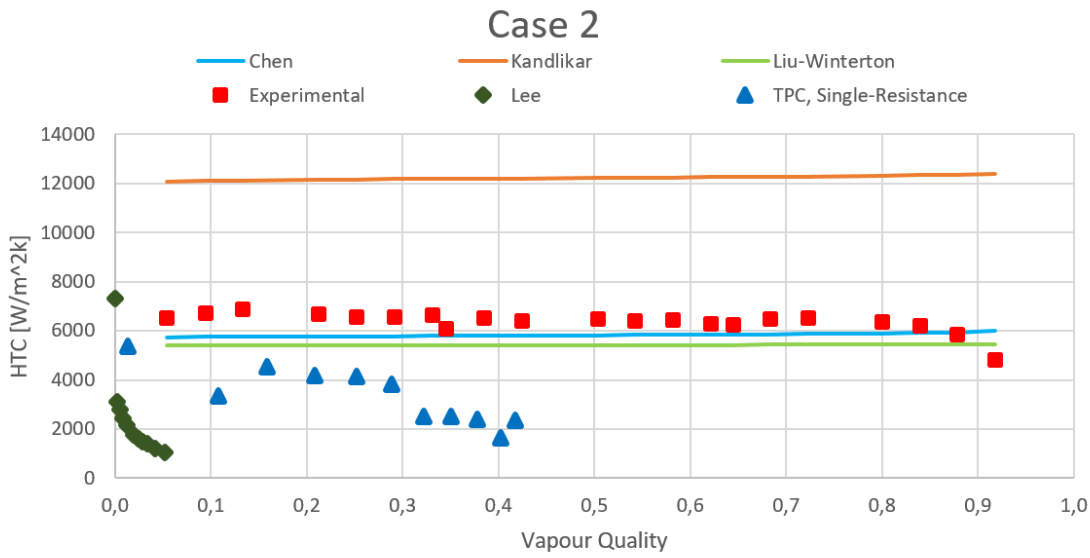

Figure 5.16: Predicted HTCs of the Lee and Thermal Phase Change models with default coefficients for Case 2, compared against experimental data and correlations.

5.1.2.3.2 Tuned coefficients

The second part focuses on tuning the mass transfer coefficients of the Lee and TPC models in order to improve their accuracy towards the experimental data.

5.1.2.3.2.1 Lee model

Starting with the Lee model, the coefficient was varied between 0.1 (default) - 2500. The results are presented in Fig. 5.17. It was observed that increasing the coefficient provided some improvement. However, the outlet vapour quality eventually reached a maximum, and further increment did not result in higher values (see Fig. 5.18). Further, even for the maximum coefficient setting, the resulting outlet vapour quality mass fractions were substantially below those noted for the experiments.

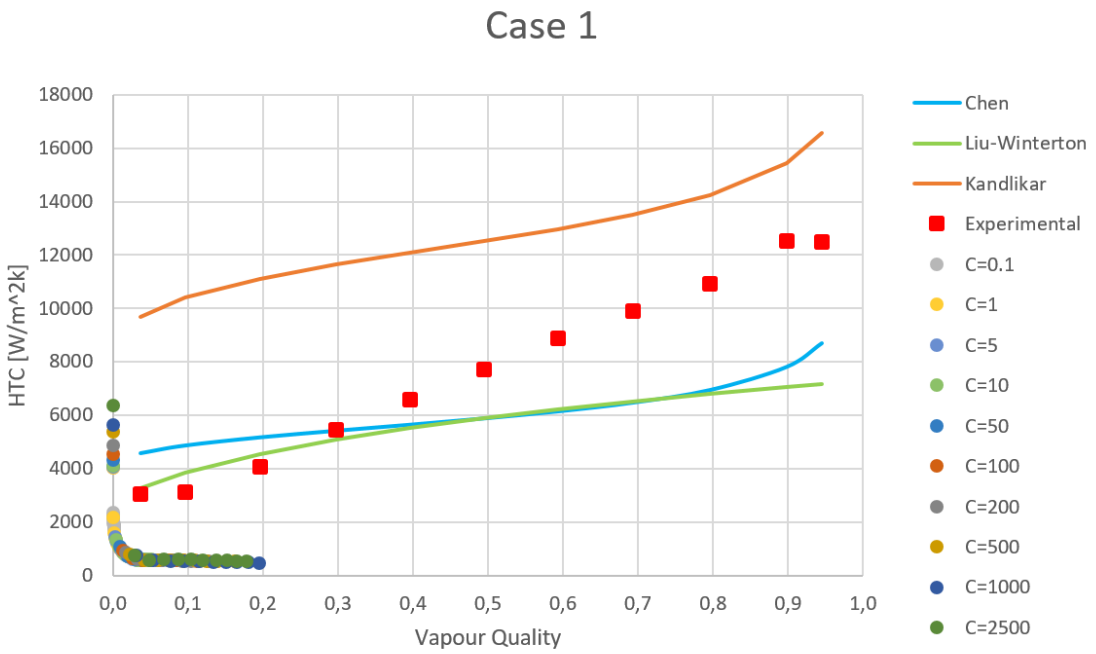

Figure 5.17: Predicted HTCs of the Lee model with tuned coefficients for Case 1, compared against experimental data and correlations.

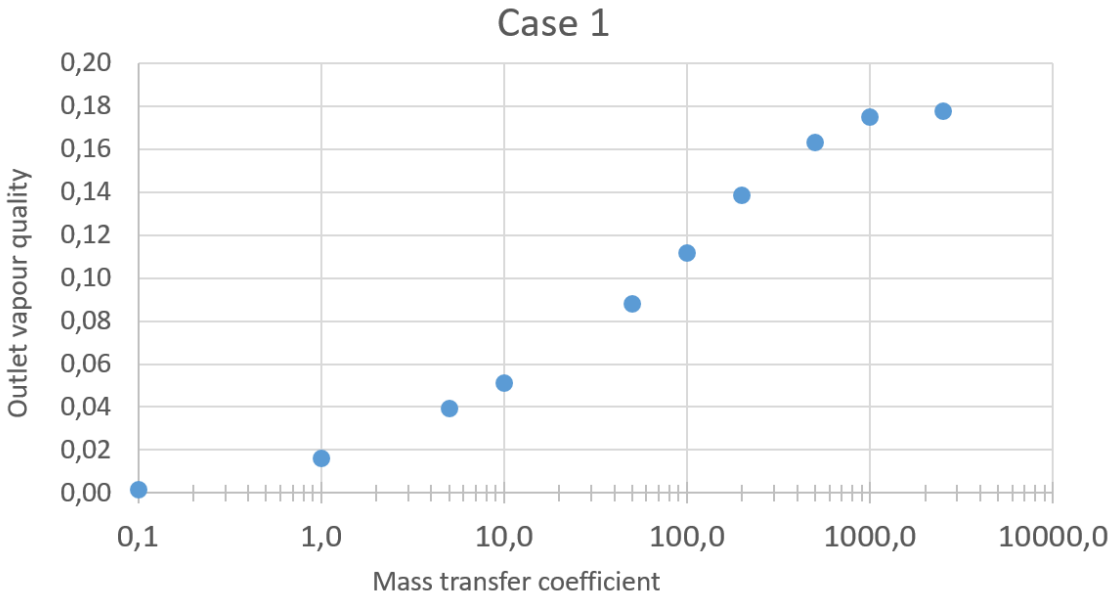

Figure 5.18: Predicted outlet volume fractions with increments of mass transfer coefficients in the Lee model.

5.1.2.3.2.2 Thermal Phase Change model

For the TPC model, the coefficient was set to 1 (default), 5, and 10. The resulting heat transfer coefficients and vapour qualities are presented in Fig. 5.19. It can be observed that all coefficients yielded roughly the same outlet vapour quality, while the heat transfer coefficients varied with no apparent pattern.

It has been stated that the model does not require tuning since the mass transfer rate is directly dependent on the heat transfer coefficients [28], and the results from this analysis did appear to validate these comments.

A possible explanation for the inaccuracies of the volumetric mass transfer models could be that they do not account for the nucleation of bubbles, which is arguably the most important phenomenon to consider when modeling boiling flows [5], [35].

Another important characteristic of boiling flows, which was not modeled in the numerical simulations, was the polydispersity of the vapour bubbles. The transport equation formulation of the interfacial area concentration was used in the sub-model survey, but it did not seem to yield significantly different results compared to the algebraic model.

In literature, population balance models coupled with the RPI wall boiling model have been successfully implemented to account for these phenomena [59]. It seems as though the complexities of flow boiling cannot be modeled accurately unless these sub-continua phenomena are carefully modeled.

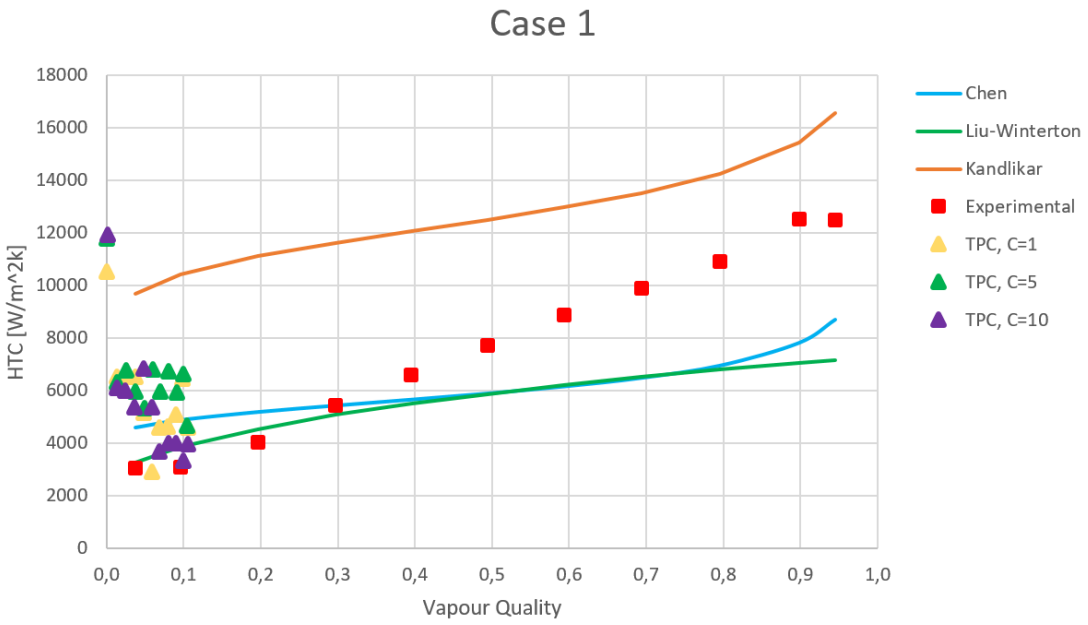

Figure 5.19: Predicted HTCs of the TPC model with tuned coefficients for Case 1, compared against experimental data and correlations.

5.1.2.3.3 Summary

The multiphase simulations were less accurate than single-phase simulations in matching experimental data, with mass transfer models under-predicting vapour quality, particularly for Case 1. Case 2 showed higher vapour quality due to lower mass flux and higher heat flux.

In general, the TPC model performed better than the Lee model but still showed significant deviations from experimental results. Increasing the coefficient improved the predictions slightly for the Lee model, but further increases did not enhance the vapour quality beyond a certain point, indicating that the model could not be effectively tuned sufficiently to replicate the experimental results. It should be noted that these findings echoed those of Peyvandi, who reached the same conclusion in his master thesis where the Lee model was used to model condensation in heat exchanger tubes [60].

Despite tuning of the mass transfer coefficient, the TPC model generally yielded the same vapour qualities for all the coefficient settings, indicating that the model could not be tuned to match the experimental results simply by increasing the coefficients.

Volumetric mass transfer models do not account for bubble nucleation, unlike the RPI wall boiling model, which has been successfully coupled with population balance models and has shown to accurately model the complexities of flow boiling, and this was considered one of the major reasons for the underperformance of the Lee and TPC models in this investigation.

5.1.2.4 Conjugate heat transfer

A review of relevant literature indicated that explicit modeling of the tube walls, also known as conjugate heat transfer (CHT) modeling, could impact the overall performance of the simulations [61], [62]. This approach involves calculating the heat diffusion through the tube walls, specifically calculating the wall temperature while accounting for thermal conductivity of the copper walls. Eq. 2.2 can be rewritten to represent the radial direction as:

$$\frac{q_{cond}}{A} = k(T_{\text{outer wall}} - T_{\text{inner wall}}) \tag{5.2}$$

where $T_{\text{inner wall}}$ is then used in the convective heat transfer eq. (see Eq. 2.3) as:

$$\frac{q_{\text{conv}}}{A} = h(T_{\text{inner wall}} - T_{\text{wall adjacent fluid}}) \tag{5.3}$$

Consequently, a brief investigation was conducted to determine whether including the tube walls would affect the predicted results. The mass transfer models were used with default coefficients, together with the boundary conditions equivalent to Case 1.

5.1.2.4.1 Mesh

In Figs. 5.20 and 5.21, the mesh including the tube walls is presented. 50,000 cells representing the tube walls were added to the 200k cell mesh, amounting to a total of 250k cells. The tube walls were divided into five layers to ensure high enough resolution for the temperature distribution.

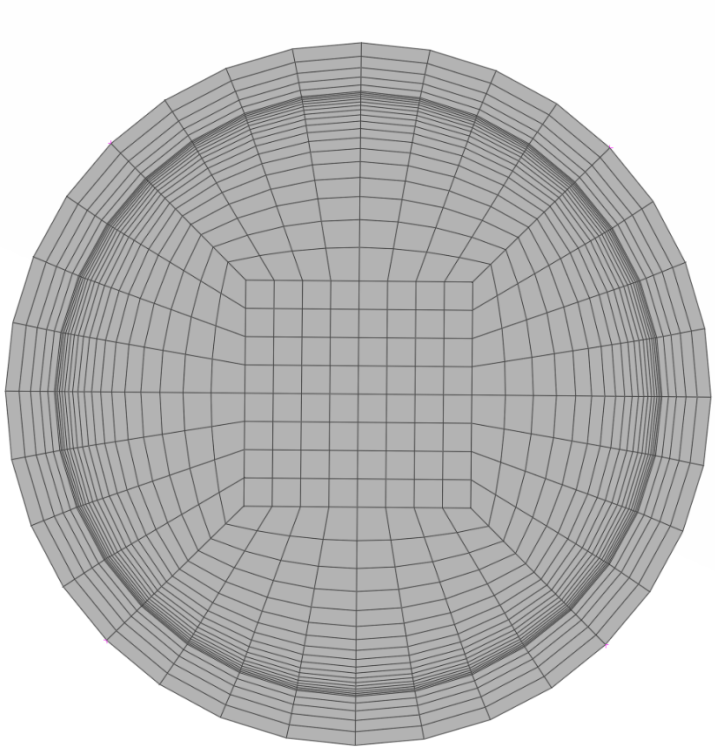

Figure 5.20: Cross-sectional view of the mesh including the tube wall thickness.

Figure 5.21: Axial view of the mesh including the tube wall thickness.

5.1.2.4.2 Thin walls vs Thick walls

In this section, the numerical results from the CHT investigation are presented. Figs. 5.22 - 5.23 compare the vapour volume fractions produced by the mass transfer models with and without CHT. Modeling with CHT consistently yielded higher vapour volume fractions across all configurations.

The HTCs for the four different configurations are presented in Fig. 5.24, and they support this conclusion. However, as was the case for all of the results to date, the results which included modeling of the wall thickness still deviated significantly from the experimental data.

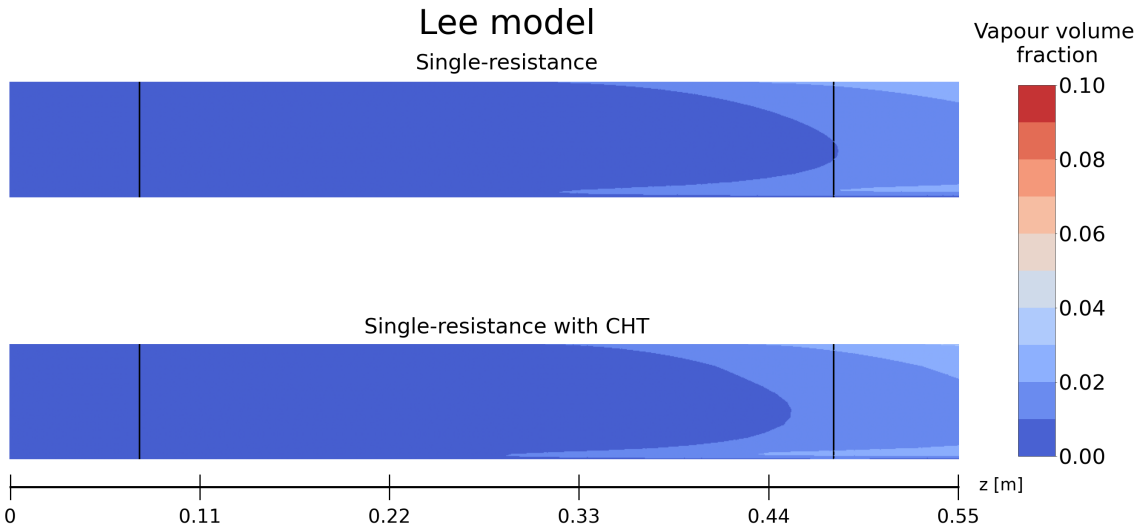

Figure 5.22: Comparison of modelling with and without CHT with the Lee model. Contours showing vapour volume fraction in the axial direction.

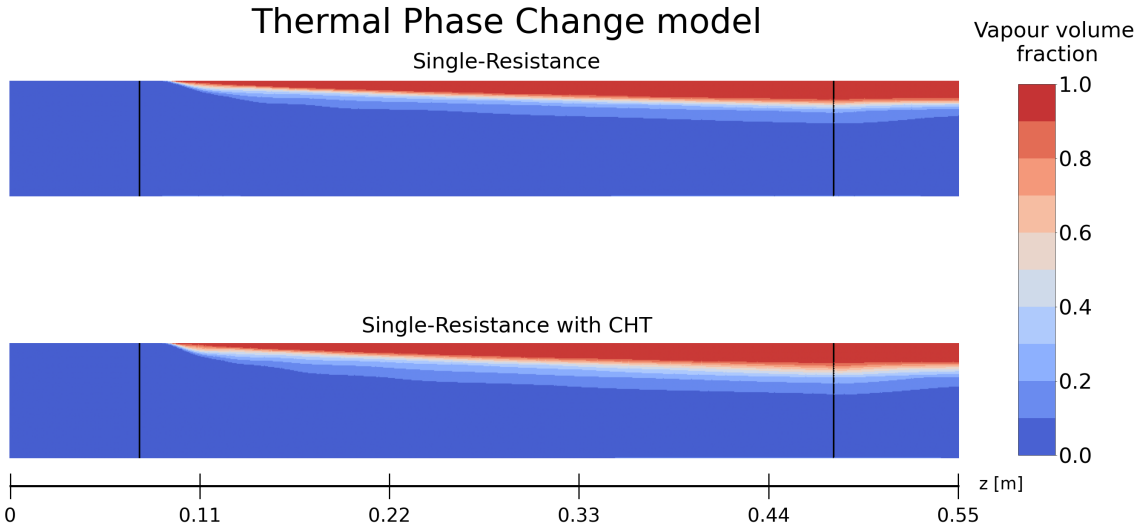

Figure 5.23: Comparison of modelling with and without CHT with the Thermal Phase Change model (single-resistance). Contours showing vapour volume fraction in the axial direction.

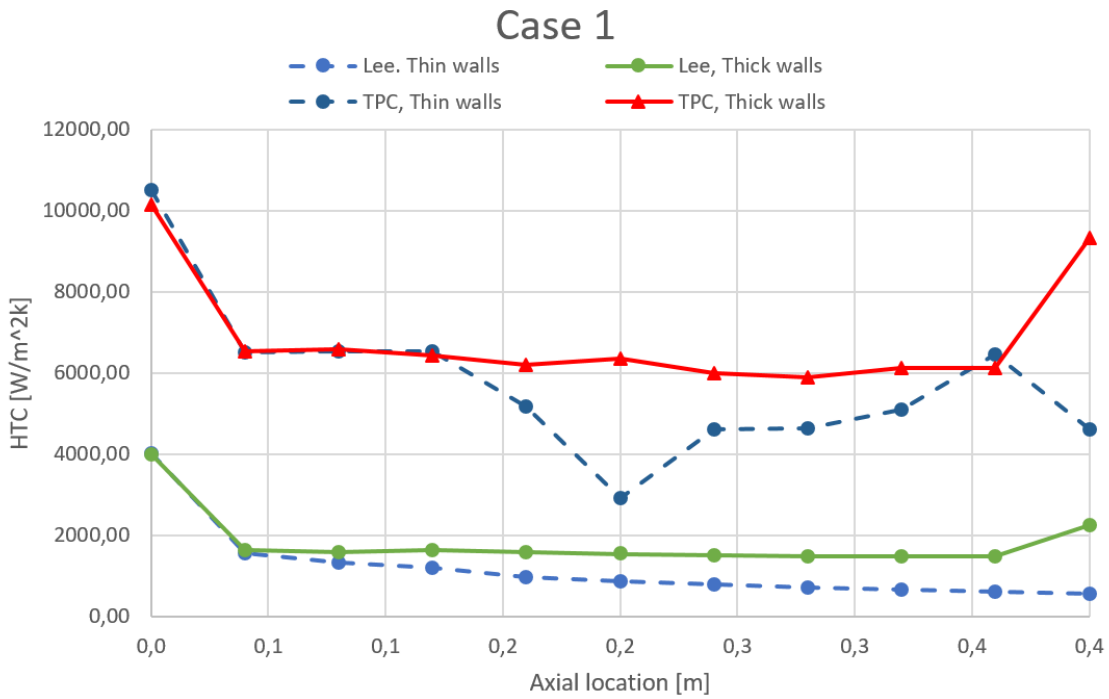

Figure 5.24: Predicted HTCs of the mass transfer models with and without CHT for Case 1, compared against experimental data and correlations.

5.1.2.4.3 Single vs Double resistance models (thick walls)

Finally, in this section, CHT modelling using both single- and double-resistance approaches are compared. The aim of this investigation is to determine whether the double-resistance approach models the wall temperatures more accurately than the single-resistance approach when the tube walls were modelled explicitly.

In Figs. 5.25 and 5.26, the resulting vapour volume fractions and temperature profiles from the simulations using the single- and double thermal resistance sub-models, in conjunction with explicit modelling of the tube walls, are compared. It can be seen that the double-resistance approach yielded a higher volume fraction and higher temperatures in the walls and the fluid domain. This indicates that the added thermal resistance of the vapour phase will increase its temperature, as well as the adjacent walls and liquid phase. As a result, the enhanced thermal conditions facilitate the evaporation of the liquid, thereby increasing the vapour fraction.

Further, the resulting HTCs and vapour qualities are compared against experimental data and correlations in Fig. 5.27. Once again, the double-resistance approach performed better than the single-resistance approach, yielding higher vapour quality and a closer match to the experimental HTCs.

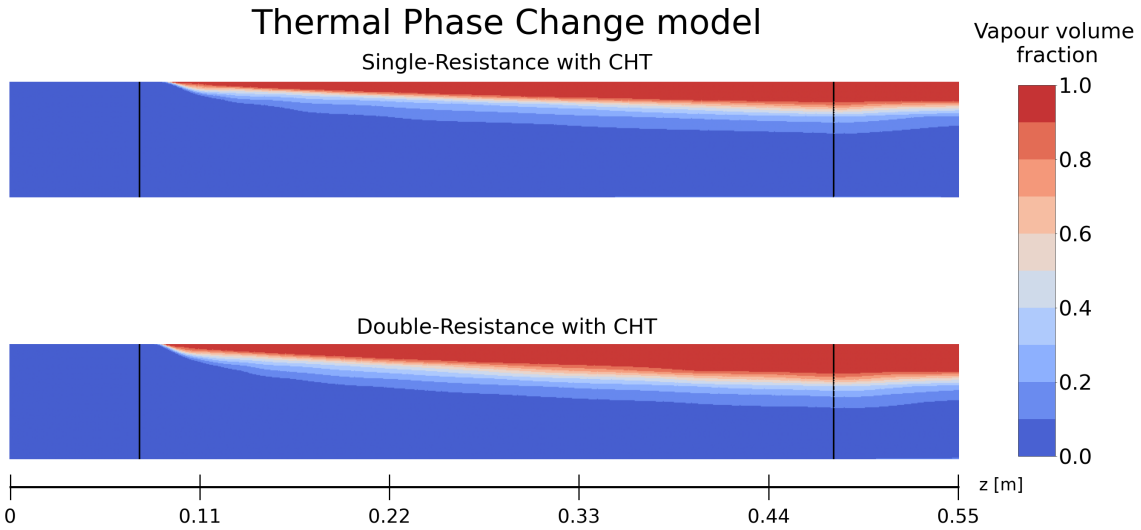

Figure 5.25: Comparison of the single- and double-resistance approaches with the Thermal Phase Change model and CHT. Contours showing vapour volume fraction in the axial direction.

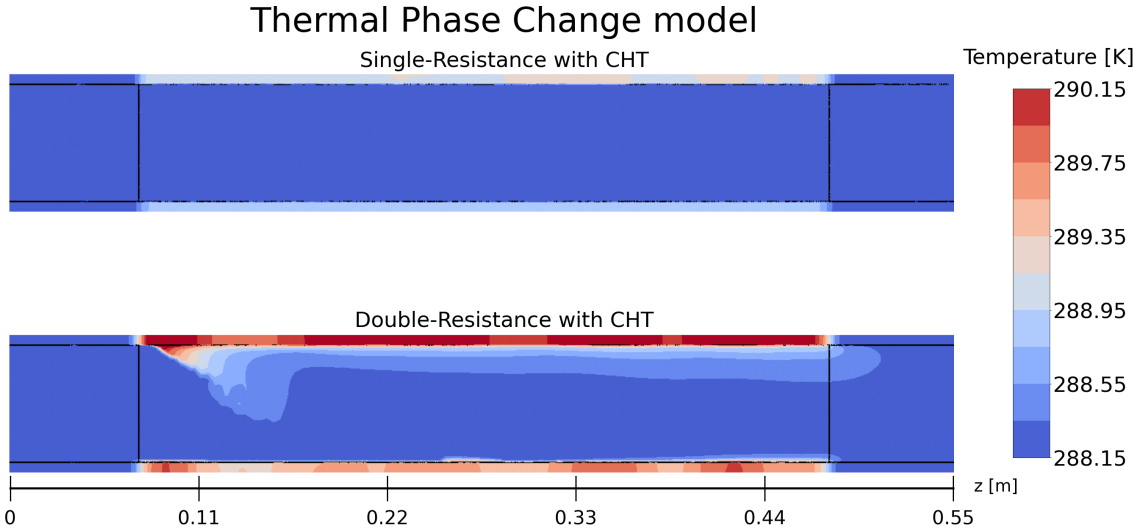

Figure 5.26: Comparison of the single- and double-resistance approaches with the Thermal Phase Change model and CHT. Contours showing the temperature distribution in the axial direction (vapour temperature in the fluid domain and wall temperature in the solid domain).

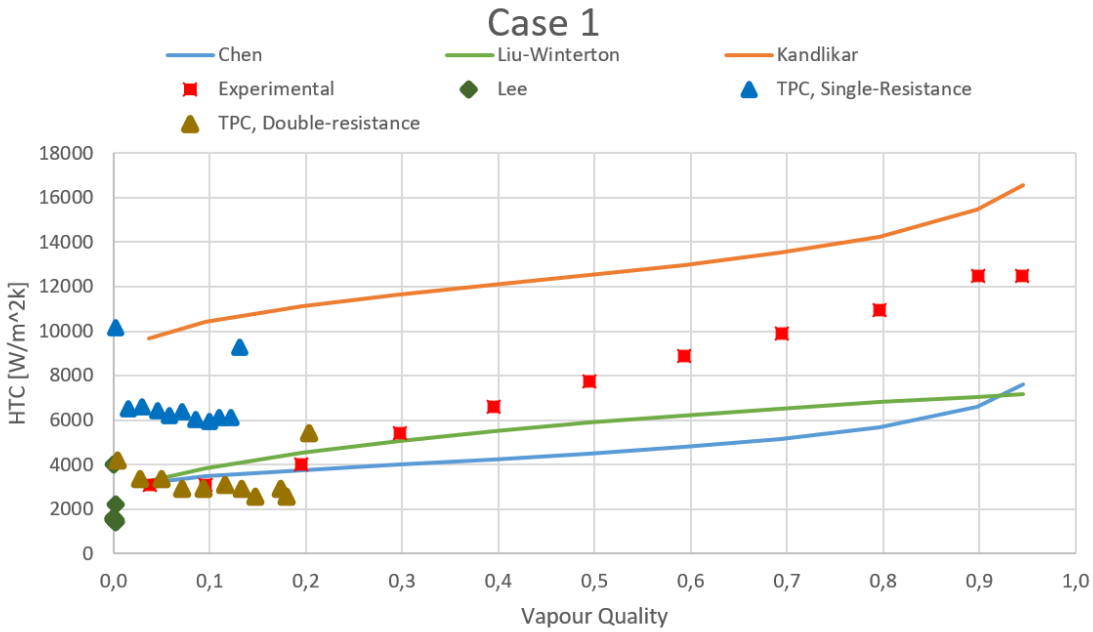

Figure 5.27: Predicted HTCs of the single- and double-resistance approaches with the Thermal Phase Change model and CHT, compared against experimental data and correlations.

5.1.2.4.4 Summary

In conclusion, the results of this investigation suggest that explicit modelling of the tube walls is necessary to match experimental data, and more specifically, resulted in wall temperatures that more closely matched the results of the Jige et al experimental data. Further, the double-resistance approach appeared to be the most appropriate to model the interfacial heat transfer when compared to the single-resistance approach, as its predicted HTCs and vapour quality were a significantly better match to the experimental data.

Despite these findings, the vapour qualities observed in the experiments could not be replicated with the Lee or Thermal Phase Change model, even with the inclusion of conjugate heat transfer. This suggests that more advanced boiling models that explicitly model specific boiling mechanisms, such as the nucleation of bubbles, are more appropriate (e.g. the RPI model) [1].

6
Summary and Conclusions

As other authors have pointed out, multiphase flow continues to be a challenging field. Even for simple cases, off-the-shelf mass transfer models lack the capabilities to produce realistic representations of boiling flows. As would be expected for single-phase heat transfer, the CFD simulations were very accurate.

For all cases, the numerical results showed lower vapour quality compared to experimental data, which consistently indicated $x \approx 0.95$. Increasing the mass transfer coefficient improved the Lee model's predictions only up to a point. The Thermal Phase Change model outperformed the Lee model but still deviated significantly from experimental results, proving to be insensitive to coefficient tuning.

The inclusion of turbulent dispersion influenced results, but could not be included due to numerical difficulties. Neither lift force, added mass force, nor wall lubrication force affected the results. Other authors have indicated the importance of including the lift force in the numerical setup to account for bubble motion perpendicular to the flow velocity, primarily for vertical channels [1], [13], [39], [59]. However, the results from this thesis suggest that this effect is negligible in horizontal tubes.

Explicit modelling of the tube walls appears necessary to match experimental data, specifically to accurately model the wall temperatures. The double-resistance approach proved to be the appropriate heat transfer model choice compared to the single-resistance approach, as it predicted HTCs and vapour quality more accurately in line with the experimental data.

Nevertheless, the vapour qualities observed in the experiments could not be replicated with the Lee or Thermal Phase Change model, even with the inclusion of conjugate heat transfer. A possible explanation for the inaccuracies of the volumetric mass transfer models could be that they do not account for microscopic phenomena, such as the nucleation of bubbles, which is arguably the most important phenomenon to consider when modelling boiling flows [5], [35].

Another important characteristic of boiling flows, which was not modelling in the numerical simulations was the polydispersity of the vapour bubbles. The transport eq. formulation of the interfacial area concentration was used in the sub-model survey, but it did not seem to yield significantly different results compared to the algebraic model.

This suggests that more advanced boiling models that explicitly model specific boiling mechanisms, such as bubble nucleation, are more appropriate (e.g. the RPI model) [1]. In literature, population balance models coupled with the RPI wall boiling model

have been successfully implemented to account for these phenomena [59]. It seems as though the complexities of flow boiling cannot be modelled accurately unless these sub-continua phenomena are carefully modelled. Inevitably, numerical modelling of additional phenomena is computationally demanding and can introduce further numerical instability.

6.1 Recommendations for Future Work

The current evaporation/condensation models do not account for microscopic phenomena crucial to the heat transfer behaviour of boiling flows, highlighting a clear opportunity for advancements. Future research should focus on integrating these models with sub-models that account for bubble nucleation and bubble dynamics. Additionally, applying the Lee and TPC models to replicate more experimental cases

would be helpful to evaluate their robustness under varying conditions. Experimental studies analysing horizontal tubes with water could be particularly interesting due to their relevance to aero engine applications. Such studies would produce essential data for validating CFD simulations, thereby improving the predictive accuracy of these simulations.

Future research should also prioritize the ongoing development of the RPI model and its associated sub-models. As it is the most promising boiling model currently available, enhancing its numerical stability could significantly streamline its application, thereby facilitating its use in diverse scientific and engineering contexts.

Bibliography

[1] E. Krepper and R. Rzehak, "Cfd for subcooled flow boiling: Simulation of debora experiments," *Nuclear Engineering and Design*, vol. 241, no. 9, pp. 3851–3866, 2011.

[2] J. Welty, G. L. Rorrer, and D. G. Foster, "Chapter 14 – fundamentals of heat transfer," in *Fundamentals of Momentum, Heat and Mass Transfer*, 6th, John Wiley & Sons, 2014.

[3] D. Domairry Ganji, Y. Sabzehmeidani, and A. Sedighiamiri, "Chapter 3 - radiation heat transfer," in *Nonlinear Systems in Heat Transfer*, 1st, Elsevier, 2018.

[4] "9.3.2: Boiling, evaporation and condensation," *Chemistry LibreTexts*, 2022. [Online]. Available: `https://chem.libretexts.org/Courses/Madera_Community_College/MacArthur_Chemistry_3A_v_1.2/09%3A_Attractive_Forces/9.03%3A_Phase_Transitions/9.3.02%3A_Boiling_Evaporation_and_Condensation`.

[5] M. Ilic, M. Petrovic, and V. Stevanovic, "Boiling heat transfer modelling: A review and future prospectus," *Thermal Science*, vol. 22, pp. 249–249, 2018.

[6] S. Nukiyama, "The maximum and minimum values of the heat q transmitted from metal to boiling water under atmospheric pressure," *International Journal of Heat and Mass Transfer*, vol. 9, no. 12, pp. 1419–1433, 1966.

[7] "Boiling heat transfer." (2024), [Online]. Available: `https://www.nuclear-power.com/nuclear-engineering/heat-transfer/boiling-and-condensation/boiling-heat-transfer/`.

[8] L. Cheng, G. Ribatski, and J. Thome, "Two-phase flow patterns and flow-pattern maps: Fundamentals and applications," *Applied Mechanics Reviews*, vol. 61, 2008.

[9] M. M. Shah, "Chart correlation for saturated boiling heat transfer: Equations and further study," *ASHRAE Trans.*, 1982.

[10] R. W. Lockhart and R. C. Martinelli, "Proposed correlation of data for isothermal two-phase, two-component flow in pipes," *Chemical Engineering Progress*, vol. 45, pp. 38–48, 1949.

[11] Q. Lu, D. Chen, C. Li, and X. He, "Experimental investigation on flow boiling heat transfer in conventional and mini vertical channels," *International Journal of Heat and Mass Transfer*, vol. 107, 2017.

[12] R. Clift, J. R. Grace, and M. E. Weber, *Bubbles, Drops, and Particles*. New York: Academic Press, 1978, p. 26.

[13] A. Tomiyama, "Struggle with computational bubble dynamics," *Multiphase Science and Technology*, vol. 10, pp. 369–405, 1998.

[14] S. Khandekar, A. K. Jaiswal, and G. Sahu, "Chapter four - spray cooling: From droplet dynamics to system level perspectives," in *Advances in Heat Transfer*, 2022.
[15] A. Kumar and B. K. Hardik, "Heat transfer distribution and pressure fluctuations during flow boiling in a pipe with different orientations," *Applied Thermal Engineering*, vol. 201, 2022.
[16] F. W. Dittus and L. M. K. Boelter, "Heat transfer in automobile radiators of the tubular type," 1930.
[17] R. H. S. Winterton, "Where did the dittus and boelter equation come from?" *International Journal of Heat and Mass Transfer*, vol. 41, pp. 809–810, 1998.
[18] V. Gnielinski, "New equations for heat and mass transfer in turbulent pipe and channel flow," *International Chemical Engineering*, vol. 16, no. 2, pp. 359–367, 1976.
[19] B. S. Petukhov and V. N. Popov, "Theoretical calculation of heat exchange and frictional resistance in turbulent flow in tubes of an incompressible fluid with thermophysical properties," *TVT*, vol. 1, no. 1, pp. 85–101, 1963.
[20] H. Darcy, *Recherches expérimentales relatives au mouvement de l'eau dans*. Paris: Mallet-Bachelier, 1857.
[21] H. Blasius, *Das aehnlichkeitsgesetz bei reibungsvorgängen in flüssigkeiten*. Springer Berlin Heidelberg, 1913, pp. 1–41.
[22] L. F. Moody, "An approximate formula for pipe friction factors," *Transactions of ASME*, vol. 69, no. 12, pp. 1005–1011, 1947.
[23] B. Eck, *Technische Strömungslehre*. Springer-Verlag, 2013.
[24] Z. Liu and R. H. S. Winterton, "A general correlation for saturated and subcooled flow boiling in tubes and annuli, based on a nucleate pool boiling equation," *International Journal of Heat and Mass Transfer*, vol. 34, no. 11, pp. 2759–2766, 1991.
[25] S. G. Kandlikar, "A general correlation for saturated two-phase flow boiling heat transfer inside horizontal and vertical tubes," *ASME Journal of Heat Transfer*, vol. 112, pp. 219–228, 1990.
[26] S. G. Kandlikar and P. Balasubramanian, "An extension of the flow boiling correlation to transition, laminar, and deep laminar flows in minichannels and microchannels," *Heat Transfer Engineering*, vol. 25, no. 3, pp. 86–93, 2004.
[27] B. Andersson, R. Andersson, L. Håkansson, M. Mortensen, R. Sudiyo, and B. Van Wachem, *Computational Fluid Dynamics for Engineers*. Cambridge University Press, 2011.
[28] ANSYS, *Ansys fluent 2023 r1 theory guide*, 2023.
[29] J. Blazek, *Computational Fluid Dynamics: Principles and Applications (Second Edition)*. Elsevier, 2005.
[30] L. Davidson, *An Introduction to Turbulence Models*. 2013.
[31] D. C. Wilcox, "Re-assessment of the scale-determining equation for advanced turbulence models," *AIAA Journal*, vol. 26, no. 11, pp. 1299–1310, 1988.
[32] F. R. Menter, "Review of the sst turbulence model experience from an industrial perspective," *International Journal of Computational Fluid Dynamics*, vol. 23, no. 4, 2009.

[33] A. A. Aliabadi, "Free shear flows," in *Turbulence: A Fundamental Approach for Scientists and Engineers*, Springer International Publishing, 2022, pp. 55–63.

[34] A. Wimhurst, *[cfd] what are wall functions and how do they work? - fluid mechanics 101*, Last Accessed: 2024-06-07, 2018. [Online]. Available: `https://www.youtube.com/watch?v=fJDYtEGMgzs`.

[35] N. Kurul and M. Podowski, "On the modeling of multidimensional effects in boiling channels," in *ANS Proc. National Heat Transfer Conference*, Minneapolis, Minnesota, USA, 1991.

[36] W. E. Ranz and J. Marshall, "Evaporation from drops, part i," *Chem. Eng. Prog.*, vol. 48, pp. 141–146, Mar. 1952.

[37] W. E. Ranz and J. Marshall, "Evaporation from drops, part i and part ii," *Chem. Eng. Prog.*, vol. 48, pp. 173–180, Apr. 1952.

[38] J. Lavieville, E. Quemerais, S. Mimouni, M. Boucker, and N. Mechitoua, *Neptune cfd v1.0 theory manual*, 2005.

[39] M. Ishii, *Thermo-fluid dynamic theory of two-phase flow* (NASA Sti/recon Technical Report A). 1975, vol. 75.

[40] I. Khan and M. Wang, "Two-phase bubbly flow simulation using cfd method: A review of models," *Progress in Nuclear Energy*, vol. 125, no. 103360, p. 3, 2020.

[41] L. Schiller and Z. Naumann, "A drag coefficient correlation," *VDI Zeitung*, vol. 77, pp. 318–320, 1935.

[42] A. Tomiyama, H. Tamai, I. Zun, and S. Hosokawa, "Transverse migration of single bubbles in simple shear flows," *Chemical Engineering Science*, vol. 57, pp. 1849–1858, 2002.

[43] T. Frank, J. Shi, and A. D. Burns, "Validation of eulerian multiphase flow models for nuclear," in *3rd International Symposium on Two-Phase Flow Modelling and Experimentation*, 2004, pp. 22–24.

[44] S. P. Antal, R. T. Lahey Jr, and J. E. Flaherty, "Analysis of phase distribution in fully developed laminar bubbly two-phase flow," *International Journal of Multiphase Flow*, vol. 17, no. 5, pp. 635–652, 1991.

[45] M. R. Maxey and J. J. Riley, "Equation of motion for a small rigid sphere in a nonuniform flow," *Physics of Fluids*, vol. 26, no. 4, pp. 883–889, 1983.

[46] A. D. Burns, T. Frank, I. Hamill, and J.-M. Shi, "The favre averaged drag model for turbulent dispersion in eulerian multi-phase flows," in *5th International Conference on Multiphase Flow*, 2004.

[47] M. Pigou, J. Morchain, P. Fede, M.-I. Penet, and G. Laronze, "An assessment of methods of moments for the simulation of population dynamics in large-scale bioreactors," *Chemical Engineering Science*, vol. 171, pp. 218–232, 2017.

[48] T. Hibiki and M. Ishii, "One-group interfacial area transport of bubbly flows in vertical round tubes," *International Journal of Heat and Mass Transfer*, vol. 43, pp. 2711–2726, 2000.

[49] S. Kim, Q. Wu, and M. Ishii, "One-group interfacial area transport in vertical bubbly flow," *International Journal of Heat and Mass Transfer*, vol. 41, pp. 1103–1112, 1997.

[50] W. Yao and C. Morel, "Volumetric interfacial area prediction in upward bubbly two-phase flow," *International Journal of Heat and Mass Transfer*, vol. 47, pp. 307–328, 2004.

[51] Q. Wu, S. Kim, and M. Ishii, "One-group interfacial area transport in vertical bubbly flow," *International Journal of Heat and Mass Transfer*, vol. 41, no. 8, pp. 1103–1112, 1998.

[52] D. Jige, K. Sagawa, and N. Inoue, "Effect of tube diameter on boiling heat transfer and flow characteristic of refrigerant r32 in horizontal small-diameter tubes," *International Journal of Refrigeration*, vol. 76, pp. 206–218, 2017.

[53] K. Becker, C. Ling, S. Hedberg, and G. Strand, "An experimental investigation of post dryout heat transfer," Royal Inst. of Tech., Dept. of Reactor Technology, Stockholm, Sweden, Tech. Rep., 1983.

[54] J. Garnier, E. Manon, and G. Cubizolles, "Local measurements on flow boiling of refrigerant 12 in a vertical tube," *Multiphase Science and Technology*, vol. 13, 2001.

[55] E. W. Lemmon, M. L. Huber, and M. O. McLinden, *Nist standard reference database 23. reference fluid thermodynamic and transport properties (refprop), version 9*, 2010.

[56] Y. A. Cengel and C. J. M., *Fluid mechanics–fundamentals and applications*. 2006.

[57] M. Kadivar, D. Tormey, and G. McGranaghan, "A comparison of rans models used for cfd prediction of turbulent flow and heat transfer in rough and smooth channels," *International Journal of Thermofluids*, vol. 20, 2023.

[58] J. Bredberg, S.-H. Peng, and L. Davidson, "An improved k-omega turbulence model applied to recirculating flows," *International Journal of Heat and Fluid Flow*, vol. 23, pp. 731–743, 2002.

[59] E. Krepper, R. Rzehak, C. Lifante, and T. Frank, "Cfd for subcooled flow boiling: Coupling wall boiling and population balance models," *Nuclear Engineering and Design*, vol. 255, pp. 330–346, 2013.

[60] E. Peyvandi, "Numerical study of condensation and conjugated heat transfer from flow in a heat exchanger," Ph.D. dissertation, Chalmers University of Technology, Gothenburg, 2024.

[61] E. Bilgen, "Conjugate heat transfer by conduction and natural convection on a heated vertical wall," *Applied Thermal Engineering*, vol. 29, no. 2, pp. 334–339, 2009.

[62] L. I. Martinez, "Investigation of cfd conjugate heat transfer simulation methods for engine components at scania cv ab," M.S. thesis, Linköping University, Linköping, 2017.

A

Appendix A - Incremental Wall Flux UDF

```
    #include "udf.h"

DEFINE_PROFILE(wallheatflux, thread, i)
{
    real source = 100.0;
    face_t f;

    int iter = (nres == 0) ? 0 : (int)count2[nres - 1];
    int step = 1000;
    int max_iter = 50000;

    if (iter <= max_iter)
    {
        int step_number = iter / step;
        source = 100.0 + step_number * 100;
        source = (source > 5000.0) ? 5000.0 : source;
    }
    else
    {
        source = 5000.0;
    }

    begin_f_loop(f, thread)
    {
        F_PROFILE(f, thread, i) = source;
    }
    end_f_loop(f, thread)
}
```

DEPARTMENT OF SOME SUBJECT OR TECHNOLOGY
CHALMERS UNIVERSITY OF TECHNOLOGY
Gothenburg, Sweden
www.chalmers.se

CHALMERS
UNIVERSITY OF TECHNOLOGY